UNIVERSITÀ DEGLI STUDI DI TRIESTE

Sede Amministrativa del Dottorato di Ricerca

XXVI CICLO DEL DOTTORATO DI RICERCA IN
INGEGNERIA DELL'INFORMAZIONE

SUPERHYDROPHOBIC BIOMEMS SENSOR ARRAYS: DEVELOPMENT OF ACTUATION AND READOUT ELECTRONIC STRATEGIES

(Settore scientifico-disciplinare: ING-INF/01)

DOTTORANDA
Valeria Toffoli
Università degli Studi di Trieste

COORDINATORE
Chiar.mo Prof. **Walter Ukovich**
Università degli Studi di Trieste

Firma: ....

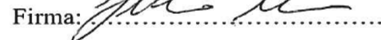

SUPERVISORE DI TESI
Chiar.mo Prof. **Sergio Carrato**
Università degli Studi di Trieste

Firma: ....

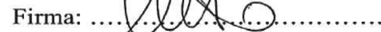

CO-SUPERVISORE DI TESI
Chiar.mo Ricercatore **Marco Lazzarino**
Istituto Officina dei Materiali – Area Science Park

Firma: ....

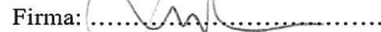

ANNO ACCADEMICO 2012 / 2013

UNIVERSITÀ DEGLI STUDI DI TRIESTE

Sede Amministrativa del Dottorato di Ricerca

XXVI CICLO DEL DOTTORATO DI RICERCA IN
INGEGNERIA DELL'INFORMAZIONE

SUPERHYDROPHOBIC BIOMEMS SENSOR ARRAYS: DEVELOPMENT OF ACTUATION AND READOUT ELECTRONIC STRATEGIES

(Settore scientifico-disciplinare: ING-INF/01)

DOTTORANDA
Valeria Toffoli
Università degli Studi di Trieste

COORDINATORE
Chiar.mo Prof. Roberto Vescovo
Università degli Studi di Trieste

SUPERVISORE DI TESI
Chiar.mo Prof. Sergio Carrato
Università degli Studi di Trieste

CO-SUPERVISORE DI TESI
Dott. Marco Lazzarino
Istituto Officina dei Materiali – Area Science Park

ANNO ACCADEMICO 2012 / 2013

SOMMARIO

La tecnologia dei sistemi micro-elettro-meccanici (MEMS) ha dimostrato d'avere grandi potenzialità in molti campi, in particolare nei sistemi bio-medicali. Essa si basa infatti su processi di fabbricazione ad altro volume produttivo, permettendo una considerevole riduzione dei costi per dispositivo. Un ulteriore beneficio di questa tecnologia risiede nella possibilità di dimensionare i dispositivi fino a raggiungere l'ordine del submicron, così da consentire l'integrazione e il monitoraggio in tempo reale di sistemi sensibili a biomarker di tipo medicale e biologici.

Tra gli obiettivi futuri dei MEMS biomedicali (BioMEMS) vi è la realizzazione di dispositivi in grado di interfacciarsi direttamente con il paziente e definirne lo stato di salute grazie alla rilevazione del livello di centinaia di diversi biomarker (siano essi chimici o fisici). La medicina assumerebbe in questa visione una configurazione ad personam nella quale al paziente verrebbe prontamente somministrato un quantitativo di medicinale adatto alle risposte del suo organismo. A tale scopo i dispositivi MEMS devono essere in grado di effettuare analisi multiple operando in un ambiente liquido. Tuttavia è proprio l'ambiente liquido a comportare la riduzione di sensibilità e, quindi, di performance dei sensori MEMS.

La presente ricerca si pone lo scopo di sviluppare nuovi sistemi elettronici di misurazione e attuazione di due distinte tipologie di BioMEMS risonanti operanti in liquido, i cantilever e i pillar. In particolare verrano trattati tre argomenti: la realizzazione di setup ottici per applicazione dei MEMS in liquido ed in aria, la progettazione di sistemi elettronici di attuazione e lettura di singoli pillar nel loro comportamento in frequenza e lo sviluppo di un software LabVIEW in grado di programmare un FPGA ed ottenere un PLL digitale da impiegarsi nell'analisi in tempo reale del comportamento in frequenza di RF-MEMS.

Il primo progetto è stato sviluppato in collaborazione l'Università di Kaiserslautern (Germania) e prevedeva la realizzazione di sistemi microfluidici e setups ottici, interfacciati in modo tale da permettere la rilevazione della risposta in frequenza di molteplici MEMS operanti in parallelo. Nel secondo progetto l'obiettivo era la realizzazione di un sistema elettronico in grado di integrare in un unico dispositivo i sistemi di attuazione e lettura dei pillar. In particolare siamo stati in grado di modulare l'ampiezza di risonanza dei nostri dispositivi risonanti mediante l'applicazione della forza di polarizzazione Kelvin mentre lo sviluppo del sistema di lettura richiede ulteriore lavoro di indagine. Infine, nell'ultimo progetto è stato realizzato un sistema PLL digitale con 10 MHz di banda passante utilizzando la tecnologia della National Instruments (FlexRIO NI5781R). Mediante questo PLL si è potuto identificare la frequenza di risonanza di diverse tipologie di MEMS e se ne è seguite le variazioni in tempo reale .

Le attività di ricerca sperimentale sono state eseguite presso il laboratorio CNR- IOM a Trieste.

ABSTRACT

Micro-electro-mechanical system (MEMS) technology has shown its high potentiality in many different fields, in particular in biomedical systems. One of the advantages of MEMS is that its technology is based on a very high throughput of the parallel fabrication process, which allows a huge reduction of the cost per device. A second remarkable advantage stems from the possibility to design small devices in the submicron range, thus enabling both implantable systems and real-time monitoring of medical and biological markers. One of the future goals of biomedical technology is indeed the realization of implantable devices able to "read" the status of the patient, based on the level of hundreds of different chemical and physical biomarkers, and to act on the patient healt by releasing a proper amount of drugs in real-time. The first step toward this ambitious results is the design of a device able to perform multiple analysis in a liquid environment. However, it is exactly the biological environment that raises the major issues for MEMS applications since the liquid environemnt and the viscous damping greatly affect the performance of MEMS sensors.

Our research was aimed at the development of new electronic measurement system for the actuation and the readout of BioMEMS resonators (mainly cantilevers and pillars) operating in liquid. In particular, this thesis covers three main subjects: the implementation of optical setups to perform air and liquid measurements, the design of electrical actuation and readout systems to study single pillar frequency behaviour and the development of a LabVIEW routine to control FlexRIO NI5781R (FPGA) to create a digital PLL with 10 MHz bandwidth for real-time RF-MEMS analysis.

The first project was partially developed in collaboration the University of Kaiserslautern (Germany) and involved the fabrication of microfluidic and optical experimental setups for the detection of the frequency response of multiple MEMS resonator operating in parallel. In the second project we focused our attention on the full integration of pillars with the on-chip electronic actuation and detection system. We demonstrated the ability to actuate target pillars by Kelvin polarization force while further work has to be done on the readout system. Finally, in the last project we realized a phase-locked look system using National Instruments technology to identify and follow MEMS resonance frequency changes.

All the experimental activities were carried out at the CNR-IOM laboratory in Trieste.

TABLE OF CONTENTS

Overview of the thesis **7**
Structure of the thesis 8
1. MEMS and BioMEMS **11**
1.1. MEMS 11
1.2. BioMEMS 12
1.2.1. Micro-mechanical resonators 14
1.2.2. Static and dynamic mode 16
1.2.3. Detection techniques 20
1.2.4. Actuation techniques 22
1.3. Pillar approach 23
2. Microfabrication and Microelectronics **31**
2.1. Microfabrication 31
2.1.1. Lithography and lift-off 32
2.1.2. Film deposition 35
2.1.3. Etching 36
2.1.4. Supercritical drying 37
2.1.5. SEM and FIB 37
2.2. Microelectronics 38
2.2.1. Integration strategies 38
3. Parallel optical readout **41**
3.1. Differential contrast measurements 41
3.1.1. HDIC microscope and experimental setup 41
3.1.2. Cantilever in air 47
3.1.3. Cantilever in liquid 50
3.2. Light-intensity measurements 52
3.2.1. Acquisition system 53
3.2.2. Data acquisition and elaboration 55
3.2.3. Results and comparison with optical lever technique 58
3.3. Summary and discussions 60
4. Electrical actuation and readout on pillar **63**
4.1. Electrical actuation 64
4.1.1. Dielectric material and polarization force 64
4.1.2. Analytical model and simulation results 66

4.1.4. Fabrication 69
4.1.5. Experimental setup 70
4.1.6. Experimental results 72
4.2. Electrical readout 75
4.2.1. Mechanical considerations 76
4.2.2. Fabrication 77
4.2.3. Implemented measurement techniques 82
4.2.4. Initial characterization 83
4.2.4.1. Impact oscillator 86
4.2.5. Preliminar results 87
4.3. Summary and discussions 88
5. Real-time measurement by DPLL 91
5.1. PLL theory and architecture 91
5.1.1. Phase detector 93
5.1.2. DDS theory 93
5.2. Implementation and analysis 95
5.2.1. NI 5781R 96
5.2.1.1. Programming strategies 98
5.2.2. Other hardware 101
5.3. Experimental results 101
5.3.1. Characterization 102
5.3.2. MEMS experiments 103
5.4. Summary and discussions 105
Conclusions 109
Acknowledgments 113

OVERVIEW OF THE THESIS

It is well established that different cell types present unique protein profile. As biomedical research continues to find new proteins or chemical markers associated with a diseases or conditions, in medical diagnostic applications there is a growing interest in detecting these markers to cure in a more efficient way or to prevent the onset of other conditions. Ideally, one person could be tested for these markers periodically, giving insight into the onset of disease, and addressing a large number of markers in parallel would give a more accurate overview of physical conditions. Moreover, developing techniques that could detect sufficiently low quantities of biomarkers would lead to the ultimate in early detection of disease with less invasive analysis. To reach this goal, biomedical research is focused on maximizing sensitivity, reducing false positives or negatives, and creating highly multiplexed systems for parallel detection of any number of biomolecules of interest.

Because of their high sensitivity as mass sensors, microelectromechanical resonators are promising candidates for the detection of biomarkers in biological fluid. Devices on the microscale are, in general, more efficient than corresponding bench-top instruments. Moreover, thanks to the ability to control physical characteristics up to the nanometer scale, the application of MEMS technology in novel areas such as in vivo imaging, single-cell detection for disease diagnostics and tissue engineering may lead to an increased understanding of the human body and to an improvement of human health and life. MEMS devices are fabricated using techniques similar to those used to create integrated circuits and are compatible with CMOS technology, which makes them promising for chip-integration and global distribution at low price. In particular, resonators sensors have been demonstrated as sensitive tools for chemical and biological detection on chip [1–5]. Their major advantages are label-free detection of the analyte and potential for array operation.

Nevertheless, research and development are needed to find robust manufacturing processes that will lead to large-scale fabrication and low-cost devices. Most of the techniques implemented and the scientific results, albeit outstanding, are not fully compatible with liquid environment and do not performed real-time measurements. The most common readout method for resonating MEMS is the optical one [6–10], which is very sensitive but requires elaborate free-space optics with precise alignment of the laser beam to the device under test; this alignment can not be easily reproduced. Parallel measurement leads to a greatly increased instrumentation complexity [11,12] (e.g. it is not reasonable to increase the number of laser much further, while the number of sensors on a chip can be in the thousands). Another common method for measuring MEMS response involves the integration of on-chip displacement sensors [13–18], with an increase in fabrication complexity and cost of

the device. Moreover, their resolution is typically low due to electrical noise and the output signal requires calibration, which may change from device to device so that comparison of the results obtain from different MEMS may be problematic.

The aim of the work presented in this thesis is the design, development and optimization of different strategies for parallel readout and single actuation of MEMS sensors. The goal is the fabrication of a fully integrated device in MEMS technology for inspection of nano-masses outside of vacuum, where they become susceptible to viscous damping. Biological sensors would greatly benefit from such improvements, allowing operation in more biologically appropriate environments and real-time observation of resonant frequency shifts. We considered two different type of vibrating structures (pillars and cantilevers). Pillars are suitable for dense array fabrication but their characteristic vertical geometry and fabrication strategy hinders a direct integration within integrated circuits. The secondary goal of the research presented in this thesis is the demonstration of a method for electrically actuate and read a single pillar. Finally we focus on real-time detection of the resonance frequency of different vibrating MEMS and detect its shift when a change in the surrounded environment is introduced.

1.1. Structure of the thesis

This thesis is structured in 5 chapters. The first chapter describes the motivation behind this doctoral thesis research. It also introduces the aims and the scope of this works and reviews the state of the art of MEMS in biomedical applications, providing an insight into the different methodologies currently used for detection of resonance devices. The techniques used in micro-fabrication are presented in chapter 2. In chapter 3 the issue of parallel detection for biological applications is addressed. A new optical configuration involving a CCD camera is studied and applied to different sensors and environments. Optimization and performance in terms of mass sensitivity are investigated, using a metal deposition as reference mass.

Pillars and their integration with IC are examined in chapter 4, both from the actuation and the readout point of views. First a theoretical study, supported by simulations, is carried out to determine the electric field dependence of the resonance frequency of pillar in a non-uniform electric field. As confirmation of the theoretical results, measurements of the frequency response of a silicon cantilever are shown. Then, a new design for an electrical reading of pillar by hard-contact technique is illustrated. The operating concept is presented, which involved the measure of the direct current from an intermittent contact once every vibration cycle between the conducting pillar and a counter electrode at a low bias voltage with respect to the pillar, while

the excitation frequency and amplitude are varied. The chapter ends with the fabrication results of the contact-pillar and the first results obtain on readout field. From this study it can be concluded that the pillar device requires a base less than 200 nm thin to operate at low frequency and enable and almost "digital" detection of its resonance behaviour.

In chapter 5 a PLL based on National Instrument Flex-RIO technology is designed and realized in its main blocks and the final configuration is illustrated. Tests on several resonant structures, like AFM tips, cantilevers and pillars, have been performed in vacuum environment and the results are presented.

REFERENCES

[1] P.S. Waggoner, and H.G. Craighead, "Micro- and nanomechanical sensors for environmental, chemical, and biological detection", Lab Chip, vol. 7, no. 10, pp. 1238–55,Oct. 2007.

[2] X. Li, H. Yu, X. Gan, X. Xia, P. Xu, J. Li, M. Liu, and Y. Li, "Integrated MEMS/NEMS Resonant Cantilevers for Ultrasensitive Biological Detection", J. Sensors, vol. 2009, pp. 1–10, 2009.

[3] N.V. Lavrik, M.J. Sepaniak, and P.G. Datskos, "Cantilever transducers as a platform for chemical and biological sensors", Rev. Sci. Instrum., vol. 75, no. 7, p. 2229, 2004.

[4] R. Bashir, "BioMEMS: state-of-the-art in detection, opportunities and prospects", Adv. Drug Deliv. Rev., vol. 56, no. 11, pp. 1565–86, Sep. 2004.

[5] B. Bhushan, "Nanotribology and nanomechanics of MEMS/NEMS and BioMEMS/BioNEMS materials and devices", Microelectron. Eng., vol. 84, no. 3, pp. 387–412, Mar. 2007.

[6] R. McKendry, J. Zhang, Y. Arntz, T. Strunz, M. Hegner, H.P. Lang, M. K. Baller, U. Certa, E. Meyer, H.-J. Güntherodt, and C. Gerber, "Multiple label-free biodetection and quantitative DNA-binding assays on a nanomechanical cantilever array", Proc. Natl. Acad. Sci. U. S. A., vol. 99, no. 15, pp. 9783–8, Jul. 2002.

[7] X.R. Zhang, and X. Xu, "Development of a biosensor based on laser-fabricated polymer microcantilevers", Appl. Phys. Lett., vol. 85, no.12, pp. 2423, 2004.

[8] N. Scuor, P. Gallina, O. Sbaizero, H.V. Panchawagh, and R.L. Mahajan, "Dynamic characterization of MEMS cantilevers in liquid environment using a low-cost optical system", Meas. Sci. Technol., vol.17, no. 1, pp. 173–80, Jan. 2006.

[9] S. Kelling, F. Paoloni, J. Huang, V.P. Ostanin, and S.R. Elliott, “Simultaneous readout of multiple microcantilever arrays with phase-shifting interferometric microscopy”, Rev. Sci. Instrum., vol. 80, no. 9, p. 093101, Sep. 2009.

[10] M. F. Khan, S. Schmid, P.E. Larsen, Z. J. Davis, W. Yan, E. H. Stenby, and A. Boisen, “Online measurement of mass density and viscosity of pL fluid samples with suspended microchannel resonator”, Sensors Actuators B Chem., vol. 185, pp. 456–461, Aug. 2013.

[11] H.P. Lang, R. Berger, F. Battiston, E. Meyer, C. Andreoli, J. Brugger, P. Vettiger, M. Despont, T. Mezzacasa, L. Scandella, and J. K. Gimzewski, “A chemical sensor based on a micromechanical cantilever array for the identification of gases and vapors”, Appl. Phys. A, vol. 64, pp. 861–864, 1998.

[12] F. Battiston, J.-P. Ramseyer, H. . Lang, M. . Baller, C. Gerber, J. . Gimzewski, E. Meyer, and H.-J. Güntherodt, “A chemical sensor based on a microfabricated cantilever array with simultaneous resonance-frequency and bending readout”, Sensors Actuators B Chem., vol. 77, no. 1–2, pp. 122–131, Jun. 2001.

[13] G. Langfelder, T. Frizzi, A. Longoni, A. Tocchio, D. Manelli, and E. Lasalandra, “Readout of MEMS capacitive sensors beyond the condition of pull-in instability”, Sensors Actuators A Phys., vol. 167, no. 2, pp. 374–384, Jun. 2011.

[14] J. Pettine, M. Patrascu, D.M. Karabacak, M. Vandecasteele, V. Petrescu, S. H. Brongersma, M. Crego-Calama, and C. Van Hoof, “Volatile detection system using piezoelectric micromechanical resonators interfaced by an oscillator readout”, Sensors Actuators A Phys., vol. 189, pp. 496–503, Jan. 2013.

[15] A. Depari, A. Flammini, D. Marioli, E. Sisinni, E. Comini, and A. Ponzoni, “A 10ms-readout interface for the characterization of high-value wide-range experimental resistive sensors”, Sensors Actuators B Chem., vol. 146, no. 2, pp. 495–501, Apr. 2010.

[16] C. Riesch, F. Keplinger, E.K. Reichel, and B. Jakoby, “Frequency response of a micromachined doubly-clamped vibrating beam for the measurement of liquid properties”, 2008 IEEE Ultrason. Symp. IEEE, pp. 1022–1025, Nov. 2008.

[17] P.A. Rasmussen, J. Thaysen, O. Hansen, S.C. Eriksen, and A. Boisen, “Optimised cantilever biosensor with piezoresistive read-out”, Ultramicroscopy, vol. 97, no. 1–4, pp. 371–6, 2003.

[18] G. Shekhawat, S.-H. Tark, and V.P. Dravid, “MOSFET-Embedded microcantilevers for measuring deflection in biomolecular sensors”, Science, vol. 17, no.311, issue 5767, pp. 1592–1595, Mar. 2006.

1. MEMS AND BIOMEMS

In the following chapter a brief introduction on MEMS and basic circuit modelling for generic MEMS resonators, as a background for pillar and cantilever resonator design, will be presented. Moreover, we will introduce the conventional actuation and readout systems used to interface MEMS with electronic intrumentations, in order to define their limits and improvements we worked on.

1.1. MEMS

MEMS, acronym of "Micro Electro Mechanical Systems", are micro systems consisting of micro mechanical sensors, actuators and microelectronic circuits. The type of MEMS device can vary from relatively simple structures to extremely complex system. The main criterion of identification is that they incorporate some elements having some sort of mechanical functionality that interact with the surrounded environments [1-1]. Generally, the scope of MEMS is very broad. Since these devices are the offspring of microelectronics and micromechanical technologies, the most important applications of MEMS technologies are transducers (sensors and actuators using piezoresistive, electrostatic, capacitive and vibration sensing schemes).

The evolution of MEMS has a long history, almost as long as that of the integrated circuits (IC). It started in the research field, where silicon microstructures were used as sensors for measuring strain and pressure back in the 1950s and 1960s, and it spread around into velocity, acceleration, electromagnetic field, etc.. Since 1990s the number of MEMS applications has blossomed and MEMS have been successfully commercialized, thanks to their fabrication techniques that are similar to those used for ICs. In fact, as sensors became less expensive, smarter and use less power, new applications became possible. Let's take as an example the history of the accelerometers: initially, when accelerometers became inexpensive enough to be used in automotive applications, they were coupled with air bags and later, as the cost dropped further, accelerometers were introduced into applications such as smart phones and video game controllers [1-2].

The ability to miniaturize their elements and to integrate electronic and transducers makes MEMS attractive not only for commercial applications but also for fundamental research. In fact, as we shrink MEMS towards the domain of NEMS (Nano Electro Mechanical Systems), the device physic becomes increasingly dominated by the surfaces and the understanding and controlling of mesoscopic mechanisms is still at the very early stages [1-

3]. This thesis mainly concerns MEM mass sensor and, in this field, one recent outstanding result is the fabrication and characterization of devices with mass sensitivity of zeptograms in ultra-high vacuum [1-4]. In figure 1-1 some of the most important MEMS sensors, developed in the last decade, are shown [1-5 – 1-10].

Another relevant MEMS research field involves nanotechnology [1-11], which is the ability to manipulate matter at the atomic or molecular level to make something useful at the nanodimensional scale and can allow us to:

- Put every atom or molecule in the desired place and position.
- Make almost any structure or material consistent with the laws of physics that can be specified at the atomic or molecular level.
- Have manufacturing costs not greatly exceeding the cost of the required raw materials and energy used in fabrication.

Although MEMS and nanotechnology are sometimes cited as separate and distinct technologies, in reality the distinction between the two of them is not so sharp. Examples of the mutual dependencies between these two technologies are the scanning tunnelling-tip microscope (STM) and atomic force microscope (AFM). In fact, a variety of MEMS technologies are required in order to interface with the nanoscale domain. Likewise, many MEMS technologies are becoming dependent on nanotechnologies for successful new products. For example, a nanotechnology called self-assembled monolayers (SAM) coating is now routinely used to treat the surfaces of the moving MEMS elements so as to prevent stiction effects from occurring over the product life.

1.2. BIOMEMS

Combined with microfluidics, bioMEMS devices provide a necessary platform for high-throughput analysis of complex biological systems [1-12]. BioMEMS technologies devices allow for lower healthcare costs and provide faster analysis of clinical samples. These goals are partially achieved by the realization of disposable and miniature clinical diagnostic systems, which can be used to detect biomarkers of specific diseases. Other important design qualities that make MEMS suitable for bio-applications are high sensitivity, multiple task integration, reliability and real-time measurements.

DNA and proteins are present in low quantities in biological samples. Standard techniques, like PCR (polymerase chain reaction), need 100 ng of genomic DNA and the lower is the amount of sample to analyze the higher is the probability of error propagation. In addition, to have a complete overview of patient condition, several so-called biomarkers have to be measured by techniques that offer low probability of artefacts and errors

in short time.

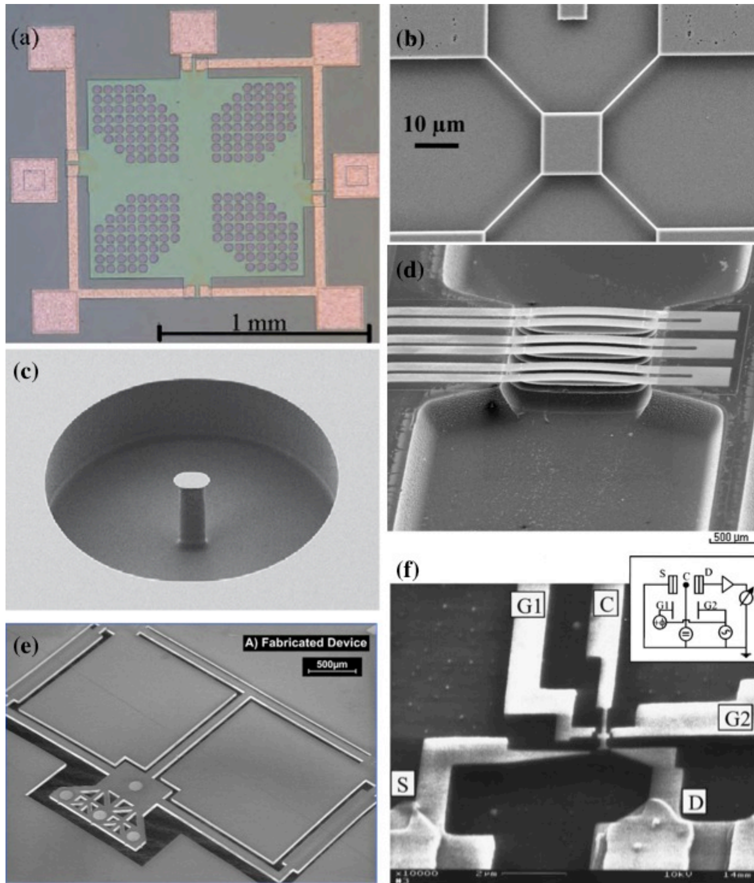

Fig. 1-1. Examples of MEMS and NEMS devices. (a) DIC image of a diaphragm piezoresistive pressure sensor arrays that couple the pressure sensing diaphragm with a perforated semi-permeable membrane [1-5]. **(b)** A quad beam oscillator for distributed mass sensing with capacitive detection [1-6]. **(c)** Columnar shaped microresonators in a trench for mass detection [1-7]. **(d)** Thermoanemometers used to measure flow velocity [1-8]. **(e)** Piezoresistive 6 degrees of freedom (DOF) force and torque sensor [1-9]. **(f)** Nanomachined electromechanical resonator applied as a mechanically flexible tunneling contact [1-10].

BioMEMS are designed to detect either a single or class of bio-chemicals, as much as system level, thanks to their analytical capabilities for a broad range of chemical species. Indeed they have the advantage of incorporating sample handling, separation, detection and data analysis into one platform and provide results in, ideally, real-time thanks to the integration of electronic and sensing devices. For this reason they are known as micro total analysis system (µTas). The most common applications of silicon-based bioMEMS devices are deoxyribonucleic acid (DNA) sequencing chips [1-13], DNA synthesis chips [1-14, 1-15], polymerase chain reaction (PCR) chips [1-16], protein separation and analysis tools [1-17], microassay applications [1-18, 1-19] and electrochemical biosensors [1-20]. Moreover, recent interest has been developed in in-vivo MEMS-based medical devices and implantable sensors [1-21] and in devices for cell manipulation [1-22], differentiation [1-23] and active culture [1-24]. Examples of µTas and Bio-MEMS are shown in figure 1-2 [1-14 – 1-18].

The ability to detect small amounts of materials, including biological entities such as pathogenic bacteria, is

important for medical diagnostics, detection of infectious agents, mass based flow cytometry, and sizing of colloidal particles. Mass sensing techniques, including quartz crystal microbalance and microcantilevers, have been used to distinguish between different biological samples as multifunctional, highly sensitive, immunospecific biological detectors. Burg et al. demonstrate a cantilever device with microfluidic channels that can resolve mass differences with a precision of 300 ag [1-25]. In this thesis, from now on, we will focus on MEMS where chemical interactions are detected by changes of the mechanical properties they cause.

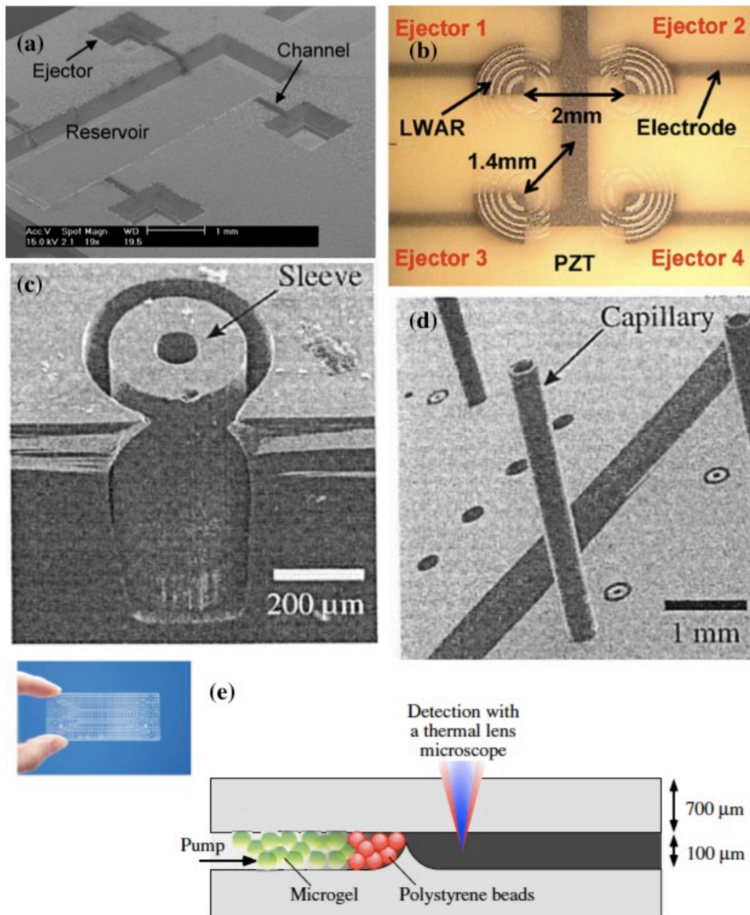

Fig. 1-12 Examples of BIOMEMS. **(a)** SEM image of a self-focusing acoustic transducer (SFAT) to synthesize deoxyribonucleic acid (DNA) sequences [1-14]. **(b)** Ejector array of an ltrasonic transducer having lens with air-reflectors (LWARs) and no nozzle to synthesize with DNA sequence [1-15]. **(c)** SEM photograph of a fluidic coupler with a 110-µm thick sleeve around the bore to prevent blocking of capillaries with adhesive [1-17]. **(d)** SEM photograph of capillaries inserted into the sleeve couplers [1-18]. **(e)** A microchip for immunoassay and its cross section with polystyrene beads and microgel [1-19].

1.3.1. Micro-mechanical resonators

A MEMS resonator consists of a resonant mechanical structure that converts energy between electrical and mechanical domains. Regardless of their shape (beams, disks, rings, plates, etc.), all resonant structures can be modelled as a spring-mass-damper system. Another model that can by applied to first order micromechanical resonator, regardless of the geometry, mode shape, and transduction methods is the RLC series circuit. The

values of inductance, capacitance and resistance correspond to values of equivalent mass, reciprocal of stiffness and damping factor. Parameters commonly used to evaluate resonators performance are resonance frequency and *Q-factor* of spectrum response, which are connected to the effective mass, thickness, density and vibration mode shape of the structure. The quality factor Q can be express as [1-26]:

$$Q = 2\pi \frac{E_M}{E_C} = \frac{f_0}{\Delta f} \tag{1-1}$$

where E_M is the mechanical energy accumulated in the resonator, E_C is the mechanical energy dissipated per vibration cycle and f_o is the resonance frequency. Δf is the difference between f_1 and f_2, where oscillation amplitude is 3 dB less than its maximum value. High *Q-factor* occurs for well-isolated system and implies high amplitude and small width of the resonance peak, as shown in figure 1-3.

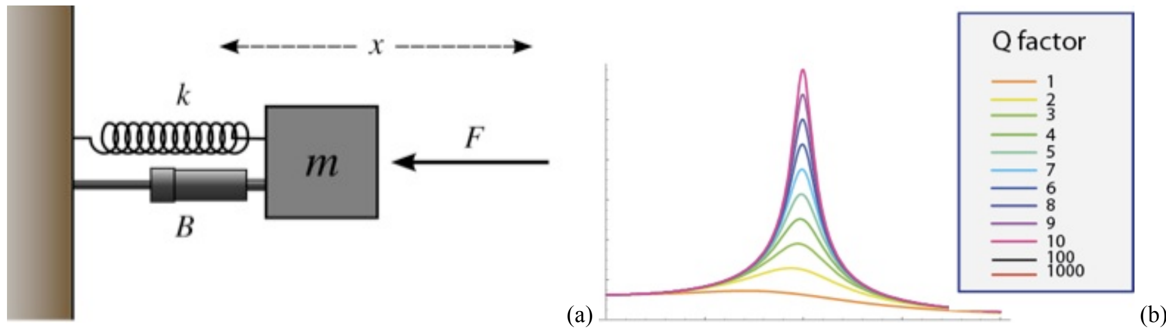

Fig. 1-3. Micromechanical resonators. (a) Model of a mechanical resonator which consist in a generic second order mass-spring damper system with an external force applied on it. **(b)** Relation between Q-factor and frequency response of the device.

Micro resonators can be suitable for applications in biomedical field, as mass sensing device (like cantilever) with picograms to attograms resolution. The adsorption of molecules on the sensor causes an increase on mass and a change of the surface stress and of mechanical properties [1-27]. If we consider a device made of a rectangular beam, clamped at one end, its spring constant (k) and resonance frequency are mainly affected by analyte adsorption and their values are given by [1-28]:

$$k = \frac{Ewt^3}{4L^3} \tag{1-2}$$

$$f_0 = \frac{1}{2\pi}\sqrt{\frac{k}{m_{eff}}} \quad (1\text{-}3)$$

where E is the Young's modulus, m_{eff} is the cantilever effective mass, w is the width, h is the thickness and L is the length, respectively. The mechanical response is sensitive to different factors, such as temperature, heat, electromagnetic field, stress and mass, which may lead to a change in the angle of cantilever bending or a shift in its resonance frequency. The detection of these responses is usually referred as static and dynamic modes of operation, respectively.

1.3.2. Static and dynamic mode

In static mode detection, the deflection of the individual cantilever depends on the stress induced by the binding reaction of the specific compounds to the interface, which takes places on only one of the cantilever surfaces. The radius R of the curvature of a cantilever is linked to cantilever stress σ by Stoney's law [1-29]:

$$\sigma = Et^2\left(6R\left(1-\gamma\right)\right)^{-1} \quad (1\text{-}4)$$

where γ is the Poisson ratio and E is Young's modulus. The thickness of the cantilever t is an important parameter that can be varied to increase or decrease the sensitivity of the device. The cantilever deformation depends mainly on the forces involved in the bioreaction and the easiest and most extended model to study the surface stress produced on cantilevers is based on Stoney's work. This model relates the total surface stress change between the top and the bottom sides (σ_1-σ_2) with the cantilever free end displacement (dz), the Young's modulus (E), the Poisson coefficient (v), the cantilever length (L) and thickness (h), with the equation [1-30]:

$$\sigma_1 - \sigma_2 = \frac{Eh^2}{L^2(1-\nu)}dz \quad (1\text{-}5)$$

In order to sense biomolecular interactions in the static mode, only one surface of the micro cantilever must be previously biofunctionalized. One example of selective functionalization is gold-thiol, where the probe molecules are functionalized with a thiol group while one side of cantilever tip is coated with gold [1-31]. During the analysis, thiolated molecules bind to the gold layer, causing an initial bending of the structure and, later on, target molecules bind to the probe molecules, generating a second deflection of the cantilever. This technique has the advantage to be compatible with a liquid environment but it requires a certain amount of

compound in order to achieve a measurable deflection and shows a slow response [1-32]. In figure 1-4 we present the result obtain using microcantilever-based immunosensor with single-chain antibody fragments as receptor molecules [1-33] and the measurement of a single base mismatch between two 11-mer oligonucleotides, detected by comparing the response of different functionalized cantilevers in an array [1-34].

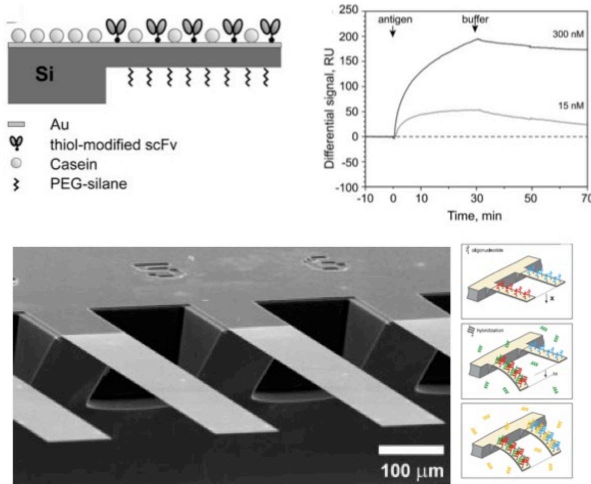

Fig. 1-4. Static and dynamic modes. (a) Side view of a gold-coated silicon cantilever functionalized with antibody fragments. The antigen AR-GCN4 was injected at concentrations of 15 nM (light gray line) and 300 nM (dark gray line). Binding was measured for 30 min and dissociation for 40 min. The arrow indicates the beginning of an injection [1-31]. **(b)** Scanning electron micrograph of a section of a microfabricated silicon cantilever array (eight cantilevers, each 1 μm thick, 500 μm long, and 100 mm wide, with a pitch of 250 μm, spring constant 0.02 N m^{-1}[1-34].

In contrast to the static case, the dynamic mode does not require the functionalization of only one side of cantilever surface. On the other hand, analyte mass can produce a change in the cantilever spring constant and asymmetric stress on the structure. Cantilevers respond to surface biochemical interactions through resonant frequency change caused by a change in its mass or stiffness. The change in mass during the experiment can be described by the following equation, as a function of the resonance frequency of device [1-35]:

$$m_S = 0.24 m_C \left(\frac{f_C^2}{f_0^2} - 1 \right) \quad (1\text{-}6)$$

where m_s is the sample mass, $0.24 \bullet m_c$ the cantilever effective mass and f_0 and f_C the resonance frequency before and during the experiment, respectively. In this way, very high sensitivity can be obtained. As already mention in the previous subparagraph, the micro cantilever resonator is also characterized by the quality factor (Q). The dissipative mechanisms could be both internal and external and, when operating in air or liquid, the external damping is the dominant factor. In particular, when operating in liquids, the resonance frequency shifts toward much lower values than in air, due to the damping effect of the viscous surroundings, while the quality factor could be up to 100-fold lower than in air, reducing the frequency resolution. In figure 1-5 three experiments using cantilever in dynamic mode for cell, virus and DNA detection are presented [1-36 – 1-38].

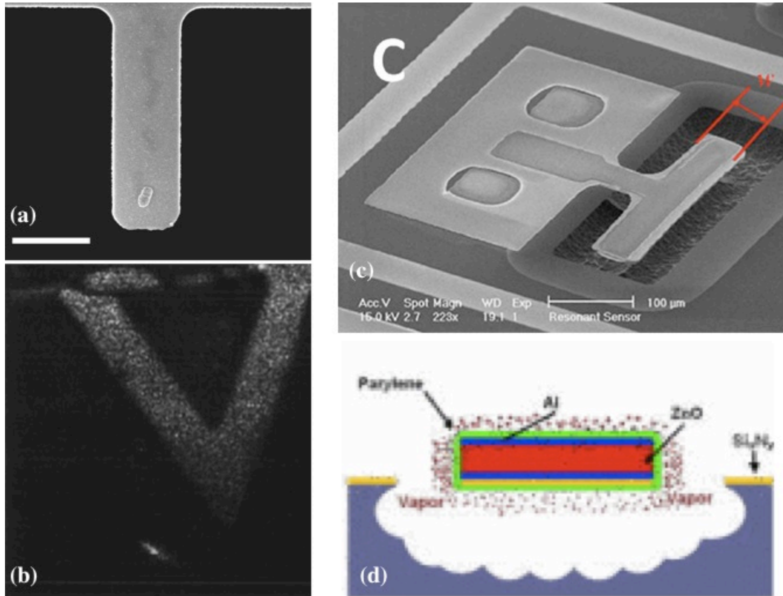

Fig. 1-5. Examples of micro cantilevers.

(a) Scanning electron micrograph ~SEM! of a single E. coli O157:H7 cell bound to the immobilized antibody layer on top of the oscillator. Tapping mode atomic force microscopy revealed the average thickness of the cells to be about 350 nm [1-36].

(**b)** Total ion image of a microcantilevers used to detect DNA strands with a specific sequence using gold nanoparticle modified DNA [1-37].

(c) (d) T-shaped cantilever with femtogram sensitive lateral extensional mode [1-38].

Resonant cantilevers immersed in liquid suffer from high damping losses and reduced sensitivity [1-39]. For this reason the dynamic mode is normally limited to the detection of gas-phase samples, while the static mode can be used for both gas and liquid samples.

In dynamic mode, external influence to the resonant frequency, such as ambient pressure and temperature, or operating conditions, such as driving voltage, has to be minimized. Hence, it is necessary to tune the driving frequency, if resonant frequency is shifted, and reduce noise influences using an analog or digital phase-locked loop circuit (PLL) [1-40]. PLL can be used also to resume additional informations connected to binding reaction time. If an oscillator is actuated by an electric signal at frequency f, the phase difference ϕ between the actuation and the readout amplitude oscillation is equal to:

$$\phi = \tan^{-1} \frac{-f_0 f}{Q\left(f_0^2 - f^2\right)} \tag{1-7}$$

At the resonance f_0, the phase difference ϕ is -π/2. PLL controls the actuating signal, compares it with the input signal coming from readout instrumentations of cantilever deflection and keeps them at --π/2 shifted. When $f=f_0$, phase difference of the two signals is null and no changing is made to the output signal. On the other end, if the phase difference (error signal) is different of zero, as shown in figure 1-6, PLL negative feedback changes the

actuating in order to null it. In 2001, Battiston et al. [1-41] realized a chemical sensor based on an array of eight silicon cantilevers and recorded the mechanical response of the resonating structure after exposure to analyte vapor by a PLL PCB (printed circuit board) controlled by software. This method has the big advantage to allow the measure in real-time and to perform very fast measurements but has the drawback that it gives no information about the change of the device compliance or the *Q-factor*. An example of this technique, applied on a bridge resonator, is reported on [1-40], where the adsorption of individual protein was recorded in real-time. Their results are shown in figure 1-7.

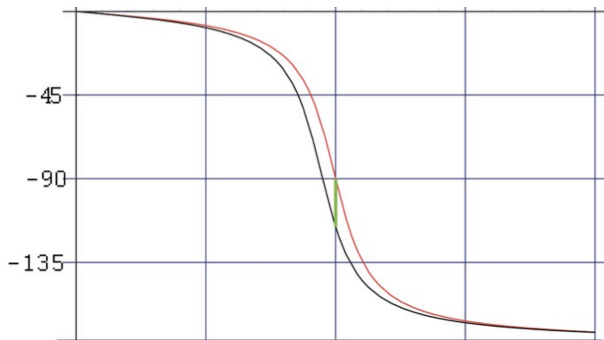

Fig. 1-6. Two curves of phase shift in function of frequency with different resonance frequency.

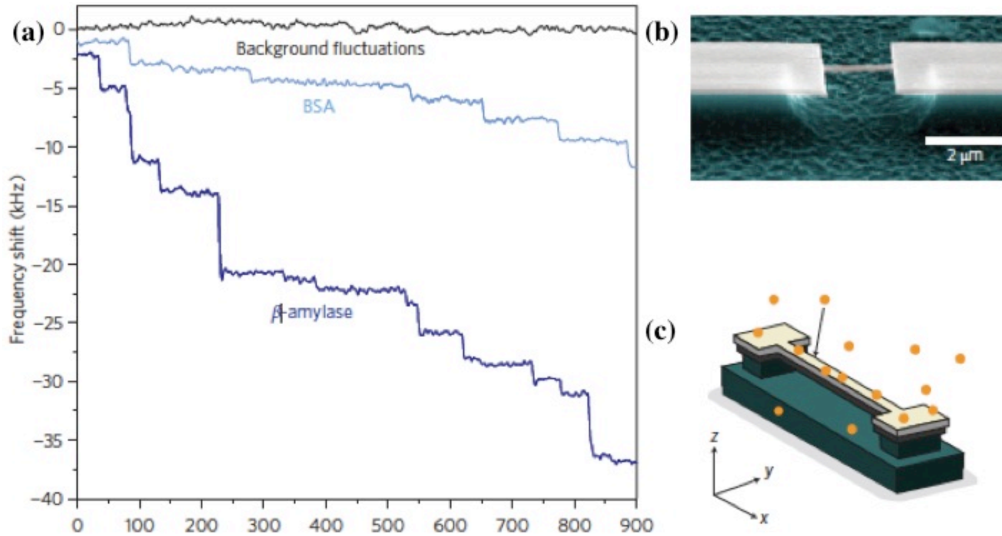

Fig. 1-7. (a) Raw experimental data show the distinctly different, precipitous resonance frequency shifts of the NEMS during ESI-induced adsorption of BSA (66 kDa) and b-amylase (200 kDa). **(b)** Scanning electron micrographs showing one of the doubly clamped beam [1-40]. **(c)** Schematic illustrating single-molecule adsorption events on a NEMS resonator and the coordinate system used to define its position-dependent mass responsivity,

1.3.3. Detection techniques

The ability to monitor changes in cantilever motion in the order of subnanometer amplitude is crucial for detecting the biochemical recognition process.

For detecting several analytes at the same time, the readout schemes requires to control in parallel large arrays of microcantilevers. Moreover, a parallel detection configuration may be used to reduce or eliminate the influence of surrounding environment factors, such as temperature changes, by using reference cantilevers. There are several techniques implemented for the cantilever response readout. The most common ones are based on piezoresistivity, piezoelectricity, interferometry, capacitance [1-42 – 1-45] and optical beam deflection. Above all, the last technique is preferred for biochemical applications [1-46], due to its high sensitivity.

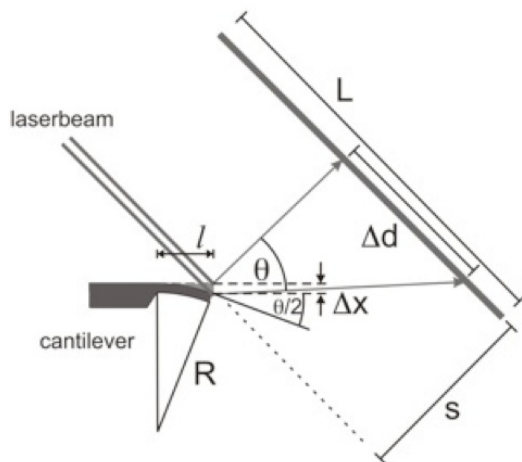

Fig. 1-8. Optical deflection mode. Beam-deflection concept to determine microcantilever bending with an accuracy of one nanometer.

In optical beam deflection method, the vibrating device is detected by focalizing a laser spot on the cantilever free end and by measuring the displacement of the reflected beam with a position-sensitive photodetector (PSD), as represented in figure 1-8. The recorded wave typically shows a linear response. The deflection angle of a cantilever at its free end can be expressed using elasticity theory as [1-47]:

$$\vartheta = \frac{3}{2}\frac{\Delta z}{l} \qquad (1\text{-}8)$$

where l is the cantilever length and Δz the displacement of the structure. This method has the advantage to be simple to implement and to offer sub-angstrom resolution but, at the same time, the implementation of multiple readout in parallel is technologically challenging, as it requires a system of aligned laser sources with the same number of elements as the cantilever array. New ways to overcome this problem involve a CCD camera [1-48] or a scanning laser source to sequentially illuminate each device.

The use of cantilevers as optical waveguide for conducting light was also implemented [1-49]. The sub-micron thickness of the cantilevers provides a high sensitivity, while the overall dimensions help to miniaturize the device and make it suitable for further integration in lab-on-chip applications. Essentially, light is injected into

the output waveguide, called the "receptor," from the cantilever. Both the cantilever and the receptor are total internal reflection waveguides and are separated from each other by a short gap. If the gap is in the order of several hundreds of nanometers, the energy transmitted into the receptor changes dramatically with the displacement of the cantilever's free end. In this case, the cantilever bending is related to the reduction in intensity of the collected light with respect to the input light and, in order to register deflection of the structure caused by any biomolecular interaction occurring on its surface, changes in the power are measured.

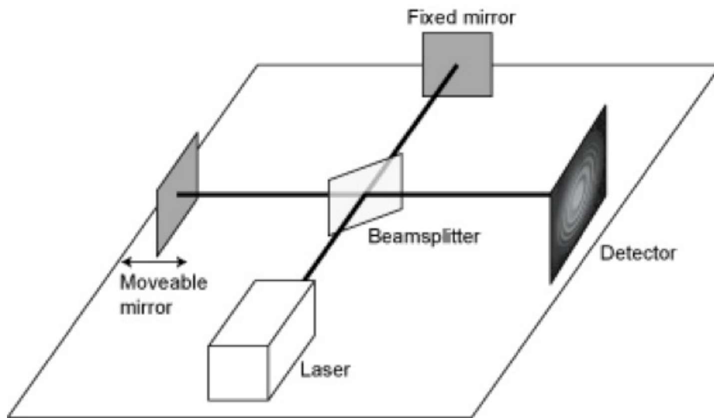

Fig. 1-9. The Michelson interferometer experimental apparatus.

Other optical detection techniques are base on constructive or destructively interference. Adaptation of Fabry-Perot and Michelson interferometers has been implemented on cantilever [1-50, 1-51]. In the basic set-up of Michelson interferometer, a collimated laser beam is reflected from a cantilever, which acts as a movable mirror, and interferes at the detector with the reference beam from a fixed mirror (figure 1-9). Interferometers rely on the change in the optical path of incident beam cause by the movement of the cantilever while the reference beam parameters (intensity, optical path, etc.) remain constant during the experiment. Both beams recombine at the detector and produce interference pattern, visible to the observer as light intensity fringes. Changes in sensor geometry are translated in changes in interference pattern characteristics. Under optimal conditions, optical beam deflection method is as sensitive as the interferometer (deflection of the order 0.01 angstrom can be measured) but they share also the same practical limitations.

As mention before, some common readout techniques involve the integration of the sensor into a IC. An example is the capacitive readout, where the motion of the MEMS causes a change in the charge on the actuation-electrode, which in turn causes a current to flow. Capacitive readout is easy to integrate in a chip, but is extremely sensitive to stray capacitance and integration of elaborate electronic readout systems on the cantilever chip are necessary [1-52, 1-53]. Furthermore, the strong actuation signals contaminate the desired readout-signal since they share the same frequency, and therefore advanced measurement techniques must be used.

Another widespread method used in MEMS readout, especially on AFM configurations, relies on piezoelectric means. When piezo-electric material is strained between two electrodes, it generates a proportional voltage,

which can also be used for readout. However, when combined with piezo-electric actuation, the strong actuation signal contaminates the desired readout signal since they share the same frequency as in the case of capacitive readout.

1.3.3. Actuation techniques

The main actuation techniques implemented in research filed rely on piezoelectricity, static electricity, magnetism and mechanical coupling.

By piezoelectricity, we can induce a crushing/elongation of the material structure by applying a potential difference at its two ends. The most used piezoelectric materials are quartz, zinc oxide and the lead zirconate titanate. They must be put in contact with the sample and have the advantage to present low power dissipation. At the same time, they suffer of hysteresis phenomena, non-linear relationship between strain and applied electric voltage and are affected by frequency and temperature.

Capacitive devices can be divided in single- and double-anchored actuators. Single-anchored configurations are constituted by a set of one or more electrodes fixed to the substrate and one or more electrodes that are free to move along a particular direction, with precise and controlled displacement. The simplest structure is characterized by a capacitor with flat and parallel faces. In double-anchored actuators, global capacitor distance and area of overlap are fixed while the movement is applied to a dielectric material sandwiched between the electrodes.

Structures based on capacitors are easy to produce on a large scale on planar device. This method involves a low consumption of energy but enable small displacement of the structure sensitive to temperature variations. On the contrary, magnetic actuators are more difficult to build on the micrometer scale than capacitive ones and, with dimension reduce of the devices, the efficiency of the magnetically actuated decreases, much more than for electrostatic systems.

Other common actuation techniques are the optical ones, which rely on the conversion of optical energy into electrostatic, thermal and elastic energy [1-54, 1-55]. These techniques relax the limit of fabrication process but, like their equivalent readout method, require the focalization of the optical setup into a specific region of MEMS sensor, making them time consuming.

1.4. PILLAR APPROACH

Micro-cantilevers are an example of resonator systems and are typically used as mass sensor since they display a great sensibility and versatility [1-56]. Suspended resonators can weigh single nano-particles, single bacterial cells and sub-mono-layers of adsorbed proteins when the sample is placed in its free end. Unfortunately, the fabrication techniques, the difficulty in controlling the sample-position [1-57] and the absorbed molecules affect the beam mechanical property in a complex way and the measure of the resonance frequency hardly provides a quantitative result. Indeed the mass response of a resonating mass sensor changes with the position of the added mass because all parts of the beam do not move at equal distances and no control on analyte position makes the approach inconsistent with the vision of having single molecule sensitivity Several approaches were developed to overcome this issue. In 2005, B.Ilic & al. [1-58] defined lithographically a small adsorption spot of 5 10^{-7}, which results to be only a tiny fraction of the overall detector size. Moreover they recognized a very low concentrated analyte, with long time of reaction time.

An alternative solution is represented by the development of columnar silicon μ-resonators. This configuration presents several sensibility advantages [1-59] but also some drawbacks. In contrast to the existing methods of oscillating cantilevers, pillar geometry allows the localizations of a small sensing surface at the top end by directional deposition system, without inducing stress on the oscillating part.

Due to the small sensitive areas, in the range of few μm^2, spotted on larger volumes, pillars are closer to a nanosphere rather than to a planar surface and response in the diffusion limited regime should be about three orders of magnitude faster. No asymmetrical residual stresses are induced by fabrication, which is an intrinsically symmetrical process. Moreover, on pillar, there is no modification of the elastic constant of the resonator due to molecular adsorption on the lateral walls, which guarantee a more precise resonance-frequency-change vs. mass calibration. The inverted tapered geometry confines the stress induced by the oscillation on pillar base and sensor mass is reduced, with an enhancement of the sensitivity. In fact, the minimum detectable mass depends on the ratio between the mass of the sensor and the resonant frequency of the resonating MEMS.

At the same time, their characteristic vertical geometry and fabrication strategy hinders a direct integration within integrated circuits. Additional material can only be deposited on sensor top end , therefore no direct electrical contacts can connect pillar to the external environment, making it electrically floating with respect to the surrounded structure. Moreover, addressing each resonator with integrated metal lines located nearby the sensors can be applied to a limited number of pillars, unless a complex multilevel fabrication approach is adopted.

REFERENCES

[1-1] S. McNamare, Y.B. Gianchandani, “MEMS-Based sensors”, Comprehensive Semiconductor Sicence and Technology: Device and Applications, vol. 5, pp. 527-559, 2011.

[1-2] H. Xie, G. Fedder, and R.E. Sulouff, “Accelerometers”, Comprehensive Microsystems, vol. 2, pp. 134-180, 2008.

[1-3] M. Poot and H. S. J. van der Zant, “Mechanical systems in the quantum regime”, Phys. Rep., vol. 511, no. 5, pp. 273–335, Feb. 2012.

[1-4] Y. T. Yang, C. Callegari, X. L. Feng, K. L. Ekinci, and M. L. Roukes, “Zeptogram-Scale Nanomechanical Mass Sensing”, Nano Letters, vol. 6, no. 4, Apr. 2006.

[1-5] M. P. Orthner, S. Buetefisch, J. Magda, L. W. Rieth, and F. Solzbacher, “Development, Fabrication, and Characterization of Hydrogel Based Piezoresistive Pressure Sensors with Perforated Diaphragms”, Sens. Actuators. A. Phys., vol. 161, no. 1–2, pp. 29–38, Jun. 2010.

[1-6] J. Arcamone, G. Rius, G. Abadal, J. Teva, N. Barniol, and F. Pérez-Murano, “Micro/nanomechanical resonators for distributed mass sensing with capacitive detection”, Microelectron. Eng., vol. 83, no. 4–9, pp. 1216–1220, Apr. 2006.

[1-7] J. Kehrbusch, P. Bozek, B. Radzio, E.A. Ilin, and E. Oesterschulze, “Columnar shaped microresonators for mass detection and gas analysis”, Microelectron. Eng., vol. 87, no. 5–8, pp. 817–820, May 2010.

[1-8] S. Vonderschmidt, J. Müller, ”A fluidic bridge based MEMS paramagnetic oxygen sensor”, Sensors and Actuators B, vol.188, pp.22– 30, 2013.

[1-9] P. Estevez, J. M. Bank, M. Porta, J. Wei, P. M. Sarro, M. Tichem, and U. Staufer, “6 DOF force and torque sensor for micro-manipulation applications”, Sensors Actuators A Phys., vol. 186, pp. 86–93, Oct. 2012.

[1-10] A. Erbe, R. H. Blick, A. Tilke, A. Kriele, and J. P. Kotthaus, “A mechanically flexible tunneling contact operating at radio frequencies”, Appl. Phys. Lett., vol. 73, no. 25, p. 3751, 1998.

[1-11] W. Boyes, “Instrumentation Reference Book, Fourth Edition”, pp.217-218, 2010.

[1-12] L H Ting, and N J Sniadecki, “Biological and Tissue Analyses”, Biological Microelectromechanical Systems (BioMEMS) Devices, pp. 257-278, University of Washington, Seattle, WA, USA, 2011.

[1-13] S. Niu and R.F. Saraf, “An approach to sequence DNA without tagging”, Smart Materials and Structures, vol. 11, pp. 778–782, 2001.

[1-14] S. Kamal-Bahl, “In situ DNA synthesis on glass substrate for microarray fabrication using self-focusing acoustic transducer”, IEEE Trans. Autom. Sci. Eng., vol. 3, no. 2, pp. 152–158, Apr. 2006.

[1-15] C. Lee, S. Kamal-bahl, H. Yu, J. W. Kwon, E. S. Kim, and S. Member, “On-Demand DNA Synthesis on Solid Surface by Four Directional Ejectors on a Chip”, J. Microelectromechanical Syst., vol. 16, no. 5, pp. 1130–1139, 2007.

[1-16] A. B. Junhon, Ming, “The Micro- Total Analytical System for the Detection of BActeria/Viruses”, J. Ind. Eng. Chem., vol. 9, no. 1, pp. 1–8, 2003.

[1-17] Y. Huang, E. L. Mather, J. L. Bell, and M. Madou, “MEMS-based sample preparation for molecular diagnostics”, Anal. Bioanal. Chem., vol. 372, no. 1, pp. 49–65, Jan. 2002.

[1-18] M. Kakuta, H. Takahashi, S. Kazuno, K. Murayama, T. Ueno, and M. Tokeshi, “Development of the microchip-based repeatable immunoassay system for clinical diagnosis”, Meas. Sci. Technol., vol. 17, no. 12, pp. 3189–3194, Dec. 2006.

[1-19] W.-H. Tan and S. Takeuchi, “A trap-and-release integrated microfluidic system for dynamic microarray applications”, Proc. Natl. Acad. Sci. U. S. A., vol. 104, no. 4, pp. 1146–51, Jan. 2007.

[1-20] M. Shi, Y. Peng, J. Zhou, B. Liu, Y. Huang, and J. Kong, “Immunoassays based on microelectrodes arrayed on a silicon chip for high throughput screening of liver fibrosis markers in human serum”, Biosens. Bioelectron., vol. 21, no. 12, pp. 2210–6, Jun. 2006.

[1-21] P. Bingger, J. Fiala, A. Seifert, N. Weber, K. Foerster, C. Heilmann, F. Beyersdorf, P. Woias, and H. Zappe, “In vivo monitoring of blood oxygenation using an implantable MEMS-based sensor”, in 2010 IEEE 23rd International Conference on Micro Electro Mechanical Systems (MEMS), 2010, pp. 1031–1034.

[1-22] D. Desmaele, M. Boukallel, S. Régnier, “Actuation meansforthemechanicalstimulationoflivingcellsvia microelectromechanicalsystems: A critical review”, Journal of Biomechanics, vol. 44, pp. 1433–1446, 2011.

[1-23] H. Cho, T. Hashimoto, E. Wong, Y. Hori, L. B. Wood, L. Zhao, K. M. Haigis, B. T. Hyman, and D. Irimia, “Microfluidic chemotaxis platform for differentiating the roles of soluble and bound amyloid-β on microglial accumulation”, Sci. Rep., vol. 3, p. 1823, Jan. 2013.

[1-24] 7] K. A. Davis, K. A. Burke, P. T. Mather, J. H. Henderson, and M. Science, “Surface Shape Memory Substrates For Active Cell Culture”, IEEE, pp. 6–7, 2011.

[1-25] T. P. Burg, M. Godin, S. M. Knudsen, W. Shen, G. Carlson, J. S. Foster, K. Babcock, and S. R. Manalis, “Weighing of biomolecules, single cells and single nanoparticles in fluid”, Nature, vol. 446, no. 7139, pp. 1066–9, Apr. 2007.

[1-26] M. Imboden and P. Mohanty, “Dissipation in nanoelectromechanical systems”, Phys. Rep., vol. 534, no. 3, pp. 89–146, Jan. 2014.

[1-27] H. Xie, J. Vitard, S. Haliyo, and S. Régnier, “High-sensitivity mass and position detection of micro-objects adhered to microcantilevers”, J. Micro-Nano Mech., vol. 4, issue 2, pp 17-25, Nov. 2008.

[1-28] C.N. Phan, M. Aureli, and M. Porfiri, “Finite amplitude vibrations of cantilevers of rectangular cross sections in viscous fluids”, J. of Fluids and Structures, vol. 40, pp. 52–69, 2013.

[1-29] G. G. Stoney, “The Tension of Metallic Films Deposited by Electrolysis,” Proc. R. Soc. A Math. Phys. Eng. Sci., vol. 82, no. 553, pp. 172–175, May 1909

[1-30] M. Hegner and Y. Arntz, “Advanced biosensing using micromechanical cantilever arrays,” Methods Mol. Biol., vol. 242, pp. 39–49, Jan. 2004.

[1-31] M. Nordström, S. Keller, M. Lillemose, A. Johansson, S. Dohn, D. Haefliger, G. Blagoi, M. Havsteen-jakobsen, and A. Boisen, “SU-8 Cantilevers for Bio/chemical Sensing; Fabrication, Characterisation and Development of Novel Read-out Methods,” Sensors, vol. 8, pp. 1595–1612, 2008.

[1-32] D. Snow, B. L. Weeks, D. J. Kim, A. Loui, B. R. Hart, and L. J. Hope-Weeks, “Static deflection measurements of cantilever arrays reveal polymer film expansion and contraction,” J. Colloid Interface Sci., vol. 316, no. 2, pp. 687–93, Dec. 2007.

[1-33] H. Lang, N. Backmann, C. Zahnd, F. Huber, A. Bietsch, A. Plu, M. Hegner, C. Gerber, and H. Gu, “A label-free immunosensor array using single-chain,” PNAS, vol. 102, no. 41, pp. 5–10, 2005.

[1-34] J. Fritz, M. K. Baller, H. P. Lang, H. Rothuizen, P. Vettiger, E. Meyer, H. Güntherodt, C. Gerber, and J. K. Gimzewski, “Translating biomolecular recognition into nanomechanics,” Science, vol. 288, no. 5464, pp. 316–8, Apr. 2000.

[1-35] V. Toffoli, S. Carrato, D. Lee, S. Jeon, and M. Lazzarino, “Heater-Integrated Cantilevers for Nano-

Samples Thermogravimetric Analysis”, Sensors, vol. 13, pp.16657-16671, Dec. 2013.

[1-36] B. Ilic, D. Czaplewski, M. Zalalutdinov, H. G. Craighead, P. Neuzil, C. Campagnolo, and C. Batt, “Single cell detection with micromechanical oscillators,” J. Vac. Sci. Technol. B Microelectron. Nanom. Struct., vol. 19, no. 6, p. 2825, 2001.

[1-37] M. Su, S. Li, and V. P. Dravid, “Microcantilever resonance-based DNA detection with nanoparticle probes,” Appl. Phys. Lett., vol. 82, no. 20, p. 3562, 2003.

[1-38] W. Pang, L. Yan, H. Zhang, H. Yu, E.S. Kim, and W.C. Tang, ”Femtogram mass sensing platform based on lateral extensional mode piezoelectric resonator”, Appl. Phys. Lett. vol. 88, issue 243503, Jun. 2008.

[1-40] A. K. Naik, M. S. Hanay, W. K. Hiebert, X. L. Feng, and M. L. Roukes, “Towards single-molecule nanomechanical mass spectrometry,” Nat. Nanotechnol., vol. 4, no. June, pp. 445–450, 2009.

[1-41] F. Battiston, J.-P. Ramseyer, H. . Lang, M. . Baller, C. Gerber, J.K. Gimzewski, E. Meyer, and H.-J. Güntherodt, “A chemical sensor based on a microfabricated cantilever array with simultaneous resonance-frequency and bending readout,” Sensors Actuators B Chem., vol. 77, no. 1–2, pp. 122–131, Jun. 2001.

[1-42] T. Sharma, S.-S. Je, B. Gill, and J. X. J. Zhang, “Patterning piezoelectric thin film PVDF–TrFE based pressure sensor for catheter application,” Sensors Actuators A Phys., vol. 177, pp. 87–92, Apr. 2012.

[1-43] P. Gonzalez, B. Guo, M. Rakowski, K. De Meyer, and A. Witvrouw, “CMOS compatible polycrystalline silicon–germanium based pressure sensors,” Sensors Actuators A Phys., vol. 188, pp. 9–18, Dec. 2012.

[1-44] O. Ferhanoglu, M. F. Toy, and H. Urey, “Two-Wavelength Grating Interferometry for MEMS Sensors,” IEEE Photonics Technol. Lett., vol. 19, no. 23, pp. 1895–1897, Dec. 2007.

[1-45] G. Langfelder, T. Frizzi, A. Longoni, A. Tocchio, D. Manelli, and E. Lasalandra, “Readout of MEMS capacitive sensors beyond the condition of pull-in instability,” Sensors Actuators A Phys., vol. 167, no. 2, pp. 374–384, Jun. 2011.

[1-46] J. X J Zhang, and K. Hoshino, “Molecular Sensors and Nanodevices: Principles, Designs and Applications in Biomedical Engineering”, Micro & Nano Technologies, 2013.

[1-47] L. Y. Beaulieu, M. Godin, O. Laroche, V. Tabard-Cossa, and P. Grütter, “A complete analysis of the laser beam deflection systems used in cantilever-based systems,” Ultramicroscopy, vol. 107, no. 4–5, pp. 422–30, 2007.

[1-48] C.D.W. Jones, C.A. Bolle, R. Ryf, M.E. Simon, F. Pardo, V.A. Aksyuk, W.Y.-C. Lai, J.E. Bower, J.F. Miner, F.P. Klemens, R.A. Cirelli, T.W. Sorsch, E.J. Ferry, L.A. Fetter, C.-S. Pai, J.A. Taylor, B. Vyas, G.P. Watson, B. Stekas, M.R. Baker, A.R. Papazian, N.R. Basavanhally, W.M. Mansfield, A. Kornblit, R.C. Keller, J.V. Gates, and A.P. Ramirez, "MEMS thermal imager with optical readout", Sensors and Actuators A, vol. 155, pp. 47–57, 2009.

[1-49] W.-C. Wang, M. Fauver, J.N. Ho, E.J. Seibel, and P.G. Reinhall, "Micromachined optical waveguide cantilever as a resonant optical scanner", Sensors and Actuators A, vol. 102, pp. 165–175, 2002.

[1-50] S.T. Koev, W.E. Bentley, and R. Ghodssi, Interferometric readout of multiple cantilever sensors in liquid samples", Sensors and Actuators B, vol. 146; pp. 245–252, 2010.

[1-51] J.W. Ochsmann, A.Cavaliere, S. Lenz, R. Raitieri, J.S. Gutmann, and R. Berger, "Simplifying cantilever sensors: Segmental analysis, a way to multiply your output", Sensors and Actuators B, vol. 177, pp. 1142–1148, 2013.

[1-52] M. Zimmermann, T. Volden, K.-U. Kirstein, S. Hafizovic, J. Lichtenberg, Oliver Brand, and A. Hierlemann, "A CMOS-based integrated-system architecture for a static cantilever array", Sensors and Actuators B, vol. 131, pp. 254–264, 2008.

[1-53] Z. J. Davis, G. Abadal, B. Helbo, O. Hansen, F. Campabadal, F. Pérez-Murano, J. Esteve, E. Figueras, J. Verd, N. Barniol, and A. Boisen, "Monolithic integration of mass sensing nano-cantilevers with CMOS circuitry," Sensors Actuators A Phys., vol. 105, no. 3, pp. 311–319, Aug. 2003

[1-54] B.R. Ilic, S. Krylov, M. Kondratovich, H. G. Craighead, and S. Member, "Optically Actuated Nanoelectromechanical Oscillators," IEEE J. Sel. Top. Quantum Electron., vol. 13, no. 2, pp. 392–399, 2007.

[1-55] M. Stuchlik, and S.R. Elliott, "All-optical actuation of amorphous chalcogenide-coated cantilevers", J. of Non-Crystalline Solids, vol. 353, pp. 250–262, 2007.

[1-56] M. Villarroyaa, J. Verd, J. Teva, Gabriel Abadal, E. Forsen, F.P. Muranò, A. Uranga, E. Figueras, J. Montserrat, J. Esteve, A. Boisen, and N. Barniol, "System on chip mass sensor based on polysilicon cantilevers arrays for multiple detection", Sensors and Actuators A, vol. 132, pp. 154–164, 2006.

[1-57] D. Ramos, J. Tamayo, J. Mertens, and M. Calleja, and A. Zaballos, "Origin of the response of nanomechanical resonators to bacteria adsorption", J. Appl. Phys. Vol. 100, issue 106105, 2006.

[1-56] B. Ilic, Y. Yang, K. Aubin, R. Reichenbach, S. Krylov, and H.G. Craighead, "Enumeration of DNA MoleculesBound to a Nanomechanical Oscillator", Nano Letters, vol. 5, no. 5, 924-929, 2005.

[1-59] M. Melli, A. Pozzato, and M. Lazzarinoa "Inverted tapered pillars for mass sensing", Microelectronic Engineering, vol. 87, issues 5–8, pp. 730–733, May 2010.

2. MICROFABRICATION AND MICROELECTRONICS

Microelectronics was born in 1948, when the first transistor, a point-contact one, was invented. In the 1950s the bipolar junction transistor (BJT) was developed while the first junction field-effect transistor (JFET) was proposed by Shockley (1952). These two types of electronic devices are at the heart of all microelectronic components, but it was the development of integrated circuits (ICs) in 1958 that spawned today's computer industry, thanks to the invention of the lithographically based planar process [2-1]. The constant improvement of silicon technology has resulted in a decreasing device size and in the increase in the number of transistors contained within a single IC.

However, the microelectronics revolution has led to increasingly complex signal-data processing chips, combined with sensors and actuators to make an information-processing triptych. The final ambitious goal is to fabricate monolithic or integrated chips that can not only sense (with microsensors) but also actuate (with microactuators). In this global vision, microelectronic integrated circuits can be thought of as the "brains" of a system and MEMS augments this decision-making capability with "eyes" and "arms", to allow microsystems to sense and control the environment. Sensors gather information from the environment by measuring mechanical, thermal, biological, chemical, optical, and magnetic phenomena. The electronics then process the information derived from the sensors and, through some decision making capability, direct the actuators to respond by moving, positioning, regulating, pumping, and filtering, thereby controlling the environment for some desired outcome or purpose. Natural evolution will then lead to MEMS devices that move around by themselves (micromachines), with sophisticated microsensors and wireless communication system.

In this chapter, a brief overview of the fundamental microfabrication technologies used for microelectronic engineering will be presented. During the thesis, these techniques were applied to realize both resonator sensor and integrated electronic elements.

2.1. MICROFABRICATION

Micro- and nanofabrication offers the opportunity to manufacture structures from the nanometer to the millimeter scales, ranging from sensors to computation and control systems. Most nanofabrication techniques were introduced first in the semiconductor industry and only later translated to sensors and MEMS applications.

The goal was to place many transistors on a silicon wafer in order to fit more and more electronic devices into a smaller working area, to increase electronic device performance and to reduce the cost for computing unit.

The fabrication strategy used today for MEMS fabrication may be divided in two classes: surface micromachining and bulk micromachining. Surface micromachining is relatively independent from the substrate. Therefore, it can be easily mixed with other fabrication techniques, which modify the substrate, and therefore is complementary to bulk micromachining. It provides additive fabrication techniques where materials are added above the surface to act as spacers or sacrificial layers to be removed at a later stage to produce freestanding structures and moveable parts. Surface processes present a limitation on layers thickness, since only thin films of various materials can be deposited onto the substrate. On the other hand, bulk micromachining is a mainly subtractive technique, which converts the substrate into an electro-mechanical part of the MEMS. Devices fabricated by this process are usually bonded to a rigid support for packaging purpose.

These processes take place into controlled environment knows as “clean room”, where particle concentration, temperature and humidity must be inside well defined ranges in order to obtain robust and repeatable results. During the ongoing of this thesis, we used a clean room of class 1000, i.e. an environment with not more than 1000 particles of diameter > 0.5 μm per cubic foot of air.

2.1.1. Lithography and lift-off

Optical lithography has been an industrial workhorse for many decades and has reached a wavelength of 193 nm [2-2]. It generally involves the transfer of a pattern from a master into a pattern transfer layer, the resist, which is then used for subsequent pattern transfer onto a working surface, e.g. silicon. The term “resist” is used because this layer is used as a masking layer for the next etching, deposition process or ion implantation. Hence, the resist allows not only the removal or addition of material to or from a specific region of the wafer but also the selective alteration of sample characteristics. Two different types of optical exposure can be implemented, contact and projection. They differ on the distance between the mask and the sample. In contact mode, a pressure of 0.04-0.3 atm is applied between the wafer and the mask, in order to ensure perfect adhesion, and the final resolution is determined by diffraction. In projection, lens system reduces the size of the design reported in the mask and the exposition of entire wafer occurs by step & repeat. Before being exposed, resist is baked at temperature in the range of 90 to 450 °C, to dry and strengthen resist adhesion to the wafer. Furthermore, photoresist is subjected to a stronger further heat treatment after being exposed, to improve the definition of the pattern and obtain more smooth vertical edges. The maximum resolution achievable with this technique is given

by:

$$R = \frac{3}{2}\sqrt{\lambda\left(s + \frac{z}{2}\right)} \tag{2-1}$$

where λ is the wavelength of the incident light, z the thickness of the photoresist and s the distance between photoresist and the mask. If $s = 0$, we have contact printing.

During lithography, the base steps are:

- The substrate is coated with a photosensitive material, known as photoresist.
- The patterns on the mask are aligned with features that already exist on the wafer.
- A light source with proper wavelength (usually UV) is used to expose the photoresist.
- The exposed photoresist is immersed in, or sprayed with, a developing solution to remove the extra photoresist as defined by the mask patterns.

A particular pattern-transfer technique, referred to as lift-off, uses a positive resist to transfer a metal pattern on a substrate which is complementary to resist one. In lift-off a film is deposited over the resist. Typically the film is a metal one and its thickness must be smaller than that of the resist. Using an appropriate solvent, the remaining parts of the resist and the deposited film above these parts of the resist are carried away, as shown in figure 2-2. The lift-off technique is capable of high resolution and is often used for the fabrication of discrete devices.

Light source with a smaller wavelength results in a better lithography resolution but, as the wavelengths get shorter, it becomes increasingly more difficult to have a light source with enough output energy.

Electron and ion beams can also be used to directly draw the desired patterns on photoresist. Due to their shorter wavelengths, e-beam or ion beam lithography systems are capable of producing features as small as a few nanometers on photoresist. However, due to the nature of their operation, the throughput of these systems is much less than the conventional systems that expose the chip area or even the whole wafer surface in one shot. Moreover, both ions and electrons are charged particles and, therefore, the exposure has to be performed under vacuum. For these reasons, e-beam and ion-beam lithography are currently used only for research or for low volume production.

Another technique to print small features on the substrates is nanoimprinting, where pattern is define onto a plastic flat surface by pressing a stamp into it. Nanoimprinting has been observed to create patterns with the aspect ratio of 10:1 and features as small as 10 nm [2-3]. Usually, this method involves the transfer of a pattern

from a micromachined quartz or metal master to a heated plastic sheet. After cooling, the plastic sustance is solidified and the mold is removed. Polymethylmethacrylate (PMMA) is often used as the plastic material.

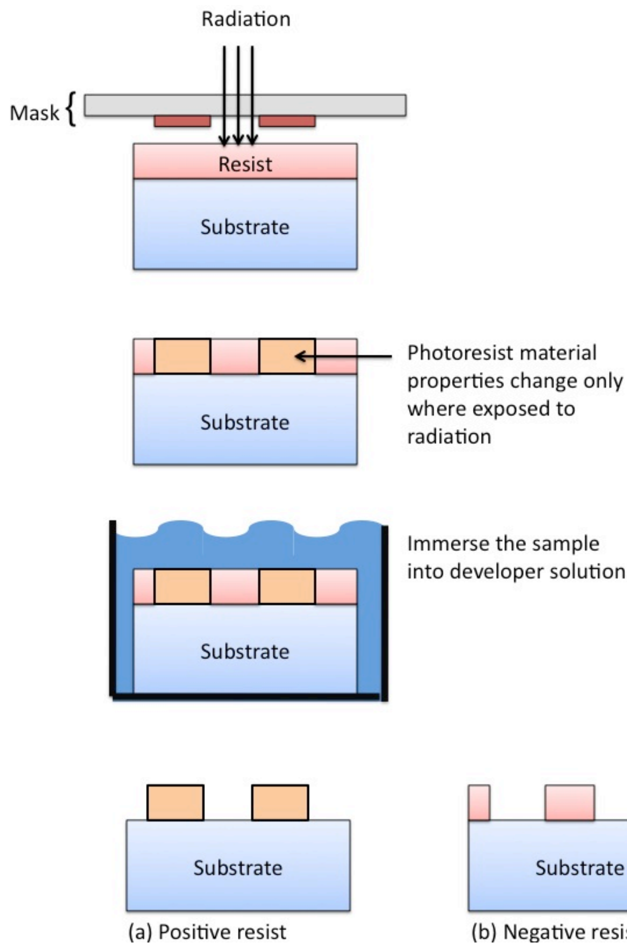

Fig 2-1. Pattern definition in **(a)** positive and **(b)** negative resist.

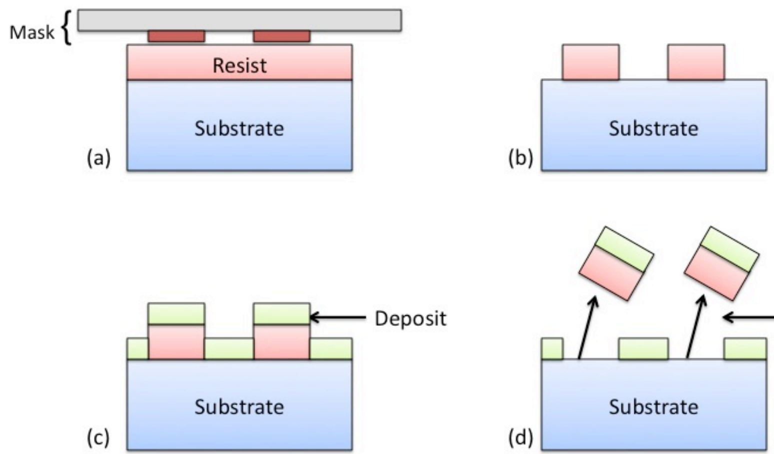

Fig 2-2. Lift-off process basic steps.

1.1.2. Film deposition

In order to fabricate a micromachined device, it is often required to work with thin films. These films can be deposited by employing various physical and chemical techniques or can be grown using the substrate material. The main techniques used to deposit the desired film are:

- Thermal oxidation: This technique can be employed to grow a silicon dioxide (SiO_2) film on a silicon substrate or a polysilicon film. In fact, silicon oxidizes if it is kept in an oxygen rich environment at elevated temperatures. The required oxygen can be supplied by a flow, and this process is called dry oxidation, or by water vapor, the so-called wet oxidation.

- Physical Vapor Deposition (PVD): A seemingly straightforward process to coat a substrate with a thin film is to force the atoms of the target material to leave a source and settle on the substrate. No chemical reactions are involved. The two main PVD processes are:

  - Evaporation: One common technique, especially used for deposition of metallic films, requires to evaporate the target material and hold the substrate at a given distance from the target. The whole process is performed under vacuum at low pressures. Two techniques are often employed to melt the target materials: Joule effect and electron beam.

  - Sputtering: It is another method for coating a substrate with a thin film of a target material in a physical manner. The surface of the target is bombarded with a flow of relatively heavy ions to knock off atoms at the surface of the target material, which then settle on the surface of the substrate and gradually form a film of the material. The ion flow needed for bombardment of the target is produced with the aid of a plasma at pressures on the order of a few mTorrs.

- Chemical Vapor Deposition (CVD): Solid films, such as silicon dioxide, silicon nitride and amorphous or polycrystalline silicon (polysilicon), can be deposited on the surface of a substrate by a CVD process. It relies on the reaction of gaseous species at the surface to form the film. The three most common types of CVD process are low-pressure CVD (LPCVD), atmospheric pressure CVD and plasma enhanced CVD (PECVD), in which radio frequency (RF) power is used to generate a plasma to transfer energy to the reactant gases.

2.1.3. Etching

Etching is a very critical step in microfabrication. In most cases, a lithography step is followed by the selective etching of films or substrates to produce the required patterns and structures. The most commonly used materials for mask layers when etching polysilicon or crystalline silicon are silicon dioxide and silicon nitride but also metal films have also been used as masking layers in dry etching processes. Base on etchant physical state (plasma or liquid), we can distinguee between:

- Wet Etching: It is a purely chemical approach for the removal of layers or bulk material. The following processes are recognized as standards. Buffered oxide etch (BOE) contains $NH_4F/HF/H_2O$ and is used for the etching of thermal oxide, LPCVD oxide and PECVD oxide, or low temperature oxides (LTO). Tetramethylammonium hydroxide (TMAH) [2-4] and potassium hydroxide (KOH) [2-5] are silicon etchants used for the crystal-oriented anisotropic etching of mono silicon using respectively thermal oxide or LPCVD nitride as etching masks materials. Polysilicon etch is a mixture of HF and HNO_3 and is used for isotropic etching of silicon and polysilicon layers. Many other reagents are used for special applications, including special etchants for metal layers (Au, Cr, Ni, Cu, Ti). The chemistry of the reactions is isotropic in nature, unless selective etch-rates are established due to crystallographic planes, change in solution substance or change in bulk materials.
- Dry Etching: Many available dry-etch processes bombard the wafer with ions through a masking layer (e.g., ion milling) and are not affected by the orientation of the crystal structure. In these approaches, parallel plates configuration makes plasma in an inert gas under reduced pressure and forces positively charged ions to hit the wafer surface, resulting in surface bombardment. It has been demonstrated that a planar etching system, when operated in the RIE mode, is capable of highly directional and high-resolution etching. Deep reactive ion etching has become very popular since the development of the "Bosch process", where both an inductively coupled plasma (ICP) source and alternating gas chemistry are used to control steps of reactive ion etching (RIE) and deposition. Such a process results in a high quality and fast etch rate and provides s selectivity between silicon and the photoresist of 100:1, thanks to the charged plasma and the high control over the ion bombardment energy. Moreover, the use of fluorine-containing etch gases, such as SF_6 (etching) and C_4F_8 (passivation), means that the Bosch process can coat the side walls and also opens the bottom of the structure, by highly directional ion bombardment. Usually passivation and etching cycles are automatically switched every 5 to 15 s.

The etching is characterized by the etching rate, i.e. the speed at which a material is removed. This parameter is not constant but depends on many factors which characterize each process:

- Selectivity: It is the ratio between the etching speeds of different materials. Selectivity can be modified by altering the chemical composition of the etch solution, adjusting the etch solution temperature, modifying the dopant concentration of one of the materials involved on the process and modifying which crystallographic planes of the substrates are exposed to the etchant solution.
- Isotropy: An etching can attack differently each crystallographic plane of a crystalline material. Wet anisotropic chemical etching is typically described in terms of etch rates according to the different normal crystallographic places, usually <100>, <110>, and <111>. In general, silicon anisotropic etching proceeds more slowly along the <111> planes than all the other planes in the lattice and the difference in etch rate between the different lattice directions can be as high as 1000 to 1. This result in profiles with tilted flat walls. If the material is instead amorphous, or the etching is isotropic, the etching will be uniform causing a spherical profile.
- Aspect ratio: it is the ratio between the lowest dimension of the pattern and the height of the etching. It appears in many etch process, especially at high rates, where the rate is often limited by the transport of etching species to the trench bottom and the transport of etch products out of the trenches. There are ways to reduce these effects, typically at the expense of rate, selectivity or profile.

2.1.4. Supercritical drying

The final rinsing and drying of the sample represents an important challenge in MEMS fabrication sequence. After wet processes, during the final drying process, a meniscus forms between suspended resonator and nearby structures. As the liquid dries, meniscus pulls resonator toward the adjacent structures and they become stuck together. Several techniques have been developed to circumvent this problem. One of them is supercritical CO_2 drying technique, in which the liquid surroundings the structures is taken from the liquid phase to the gas phase at pressures and temperatures that go above the so-called critical point. Liquid CO_2, has the critical point at T = 31 °C and P = 72.9 atm. The wafer is placed in a dedicated chamber and, by acting on the pressure in, it is possible to reduce surface tension and release structures that are micrometer in size.

2.1.5. SEM and FIB

Focus ion beam is a versatile technique, which enable imaging, mask-less milling and the deposition of conducting and insulating material with high local precision (below 1 μm). It operates similarly to a scanning electron microscope (SEM). Indeed, both instruments use charged particle from a source, focus the particles to a

beam through lenses and scan them across small areas of a sample. FIB differs from SEM for the use of charged ions orders of magnitude heavier than electrons, therefore a FIB rather mills the sample surface instead of imaging it. The subtraction of material by the impact of the ion beam has been used for microfabrication whit a resolution in the order of 1 nm. FIB can also be used for the deposition of material. A precursor gas is sprayed onto the surface of the substrate by a fine nozzle and gets absorbed. This layer is hit by the beam, which triggers a reaction whose volatile products are removed by the vacuum system. Commercial columns generally use Ga^+ ions .

On the other hand, SEM can be used for fabrication of MEMS structures and not just for imaging purpose. Electron beam writing may be performed in electron sensitive polymers such as PMMA and be implemented for micro-resolution lithography. Moreover, FIB and SEM operate with both beams at a common coincidence point on the sample. Thus, SEM can image any FIB procedure (either milling or deposition) either intermittently or simultaneously throughout the process and can give direct feedback on any FIB procedure.

2.2. MICROELECTRONICS

Solid-state technology, which has increased by orders of magnitude our computational power, is now being employed to interface computers to the physical world through sensors and actuators. Much of the motivations for using these silicon devices are linked to their ability to merge, on the same chip with the transducer, circuits for buffering, amplifying, multiplexing, or processing the electrical signal coming from the transducer. Next-generation sensors will also need integrated circuitry for controlling bus interfaces and performing self-tests and auto-calibration. This on-chip electronics is increasingly important as sensors are being applied in machinery on the factory floor, automobile and jet engines, deep-well instrumentation, chemical processing plants, and many other remote or electrically noisy environments. Generally speaking, CMOS is an attractive technology for smart sensors because it has high input impedance and good noise immunity. Equally important is the fact that silicon is an excellent material [2-6] for fabrication of the micromechanical structures, which serve as transducers in solid-state pressure and motion sensors.

3.2.1. Integration strategy

The monolithic integration of micromechanical devices (MEMS) with driving, control, and signal-processing electronics has become a relevant aspect of industrial and research matters. This integration promises to improve

the performance of micromechanical devices as well as reducinge the cost of manufacturing and packaging. Moreover MEMS can be combinied with an electronic subsystem in the same manufacturing and packaging process, improving signal acquisition and elaboration processes. For example, in the '90, Analog Devices has demonstrated the commercial viability of this integration by interleaving the micromechanical fabrication steps of an accelerometer with the microelectronic fabrication steps of its controlling electronics.

There are three basic approaches to monolithically integrating surface micromachined polysilicon devices with their controlling electronics: microelectronics-first, interleaved, and micromechanics-first. Each of these strategies must overcome the limitations of the processing requirements of both the microelectronic and micromechanical devices. Polysilicon micromechanical devices often have large vertical topologies (typically 4 to 10 microns in height) and require long, high-temperature anneals for stress relaxation (such as 3 hours at 1100 °C). Microelectronic devices use precision photolithographic techniques that require planar substrates. They also have thermal processing budgets limited by dopant diffusion and metallization.

- The microelectronics-first approach overcomes planarity restraint imposed by the photolithographic processes by building the microelectronics before the non-planar micromechanical devices. The limitation on thermal budget of the microelectronic devices remains a problem. Although the dopant diffusion problem is mitigated by changing the fabrication technology, the aluminum metallization used in conventional microelectronic technologies melts at the temperatures needed for polysilicon anneals. To overcome the temperature limitation of the aluminum metallization, researchers at Berkeley have prototyped an all-tungsten CMOS process [2-7]. After having completed this process, the micromechanical devices are fabricated.
- The interleaved approach may be the most economical for large-scale manufacturing since it optimizes and combines the manufacturing processes of both the micromechanical devices and the microelectronic devices. This optimized manufacturing mix imposes limits on both the microelectronic device performance and the micromechanical device performance. It also requires extensive changes to the overall manufacturing flow in order to accommodate changes in just the microelectronic devices or the micromechanical devices. This limits the usefulness of this approach for rapid prototyping of different technologies or development work.
- The third approach, micromechanical devices are both annealed and planarized before the microelectronic device fabrication steps. In this way topology and thermal processing limitations of the microelectronic devices are overcome.

REFERENCES

[2-1] “Milestones:First Semiconductor Integrated Circuit (IC), 1958". IEEE Global History Network. IEEE.

[2-2] B. J. Lin, “Optical lithography—present and future challenges,” Comptes Rendus Phys., vol. 7, no. 8, pp. 858–874, Oct. 2006.

[2-3] B.D. Gates, Q. Xu, J.C. Love, D.B. Wolfe, and George M.Whitesides “Unconventional nanofabrication”, Annu. Rev. Mater. Res. 2004.

[2-4] Y. Fan, P. Han, P. Liang, Y. Xing, Z. Ye, and S. Hu, “Differences in etching characteristics of TMAH and KOH on preparing inverted pyramids for silicon solar cells,” Appl. Surf. Sci., vol. 264, pp. 761–766, Jan. 2013.

[2-5] I. a. Shah, W. J. P. van Enckevort, and E. Vlieg, “Absolute etch rates in alkaline etching of silicon (111),” Sensors Actuators A Phys., vol. 164, no. 1–2, pp. 154–160, Nov. 2010.

[2-6] T.P. Sidiki, and C.M.S. Torres, “Silicon-based nanostructures”, Nanostructured Materials and Nanotechnology, chapter 10, pp. 387-443, 2002.

[2-7] W. Yun, R. Howe, and P. Gray, “Surface micromachined, digitally force-balanced accelerometer with integrated CMOS detection circuitry,” Proc. IEEE Solid-State Sensor and Actuator Workshop, pp. 126, 1992.

3. PARALLEL OPTICAL READOUT

As described in chapter 1, while hundreds of individual sensors can be produced from silicon, the development of multiple and independent sensing readout is a complex task. Conventional optical lever readout methods are not suitable for the massively parallel detection and require the focalization and the alignment of each laser spot on sensor surface to optimize the signal. Nevertheless, they are preferred in the research field since they allow separating the readout system from the physical-biological phenomenon occurring on the microtransducer. In this chapter, the work done to develop two alternative optical setups for parallel readout will be introduced and the results obtained from the implementation of these techniques on MEMS resonators will be presented.

3.1. DIFFERENTIAL CONTRAST MEASUREMENTS

Differential phase-contrast measurement involves the detection of small phase differences between light beams, which interfere with closely adjacent part of a specimen. It is widely used in light optical microscopy in both biological and geological sciences, to distinguish between structures with similar refractive indexes or topography. Differential phase-contrast (DIC) microscopy is able to highlight small details and the result is an image with increased contrast. Its structure was integrated with a microfluidic chamber and laboratory instrumentations to record MEMS frequency response in viscous environment. In the following chapter we will introduce DIC structure and our setup. Moreover we will present the results obtain with cantilever operating in dynamic mode in air and liquid.

3.1.1. HDIC microscope and experimental setup

Differential interface contrast (DIC), according to Nomarski's patent [3-1], is a widespread interference microscopy method where differences in height are converted in differences in phase shifts and, then, in light intensities. As shown in figure 3-1, a Wollaston prism produces splits a polarized light beam in two spatially separated beams, with orthogonal polarization. The two beams are focalized by an objective on the two adjacent region of the sample and generate two images of every object structures with lateral offset. This offset is function of the height z (smaller than object field) of the specimen or of difference phase interaction of the light with sample surface. The analyzer combines the beams and the result image is presented in the image plane (y)

of microscope tube lens, with standardized amplitude of the EM field vector described by [3-2, 3-3]:

$$u(x) = e^{-i\phi(x)} + e^{-i[\Psi + \phi(x-s)]} \tag{3-1}$$

where ϕ represents the relative object phase difference, x the location coordinates in the direction of the image split and s the shear (the size of the image split). By moving the Wollaston prism perpendicular to the optical axis, it is possible to modify the phase difference between the object wave and the laterally displaced reference wave Ψ. The image intensity profile ($I(x)$) along x direction is obtained by multiplying $u(x)$ with its complex conjugate and it is equal to:

$$I(x) = I + \cos[\phi(x) + \phi(x-s) - \Psi] \tag{3-2}$$

under the assumption $\Psi \ll \pi$. Equation 3-2 can also be expressed as:

$$I(x) = s\frac{d\phi(x)}{dx} = s\frac{4\pi}{\lambda}\frac{dz}{dx} \tag{3-3}$$

where the variation of intensity of image in plane y is proportional to the first derivate of ϕ with respect to the direction of the image split. Since ϕ can be express as $4z \bullet \pi/\lambda$, where λ is the light wavelength, I is proportional to the sample slope. Obviously, larger split s of the polarized images results in a more sensitive detection system. Moreover the maximum contrast is presented in a preferential direction or, in other words, those line structures that lie in the direction of the split are not contrasted (figure 3-2). We implemented and tested this technology in order to simultaneous monitoring of multiple resonating cantilevers operating in dynamic-deflection mode for gas and liquid applications. Since cantilever has an upward-downward slope during resonance, z increase-decrease continuously along the cantilever so, in general, averaging in time the motion of the cantilever would have no effects on the image intensity. However, by setting the optical path in a suitable way, so that the reflection intensity is either at maximum or at minimum, every deviation from the steady state will always create, respectively, a decrease or an increase of intensity, which can be easily detected. High interference contrast images are obtained from microscope where light source has a narrow spectral linewidth. Indeed, white light sources would create a continuum of interference patterns, flattening the image intensity.

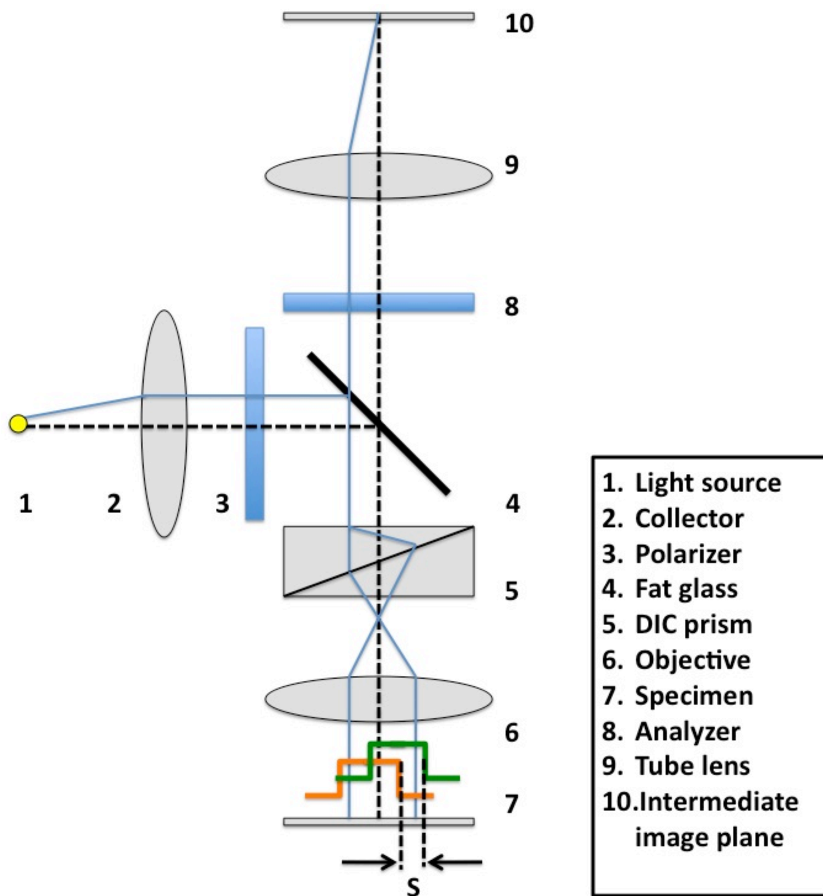

Fig. 3-1. Optical diagram of differential interference contrast (DIC) microscope.

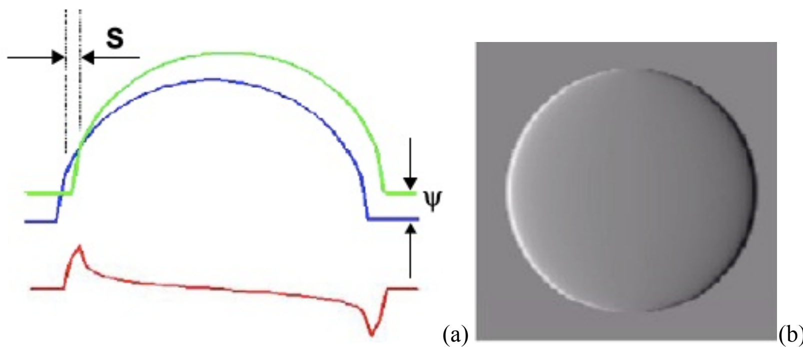

Fig. 3-2. (a) The resulting phase difference (red), obtained by DIC microscopy, represents the difference of the two identical light wave fronts displaced laterally (green and blue). **(b)** This DIC image is generated from a spherical object.

The scheme of measurement system is presented in figure 3-3. In contrast with the existing and commercial readout methods, this configuration does not require any alignment, allows the monitoring of multiple structures

and uses a light bulb as source. The introduction on the optical path of a narrow bandpass filter drastically would decrease image light intensity and, for this reason, was not implemented. The main components are an Olympus focus mount (BXFM), a high contrast prism (U-DICRHC) for reflected light and a CCD camera (IMAGINGSOURCE DBK 41BU02 - 1280 x 960 pixels and a dynamic range of 8 bit) located in a vibration-isolated table. In order to achieve high-resolution, it is particularly important to considerate image light intensity [3-4]. The sample will appear too ''noisy'' if the image is not bright enough and this noise will be amplified by video contrast enhancement. The standard deviation of photon noise in the image is the square root of the number of photons per picture element (or ''pixel''). In our setup, a common 100 W halogen bulb lamp and a camera with long exposure time ($2.57 \bullet 10^{-2}$) and low gamma correction were applied. Long working distance microscope objectives were used because of PMMA sample holder hindrance. In particular, Plan N 4x/0.10 Olympus objective allowed the view of sample of 1500x1100 μm and, due to the design of the device, 2 cantilevers can be measurement simultaneously in liquid environment.

The sample under test was placed in the objective lens focal plane and actuated by a voltage signal supplied by function generator (AGILENT 33250A). A piezoelectric crystal (lead zirconate titane) was used as actuator and the sample was glued to the elastomeric material (PDMS) that covers the crystals by means of a common nail polish. In order to perform experiments in air and liquid environment, a dedicated microfluidic chamber was built (figure 3-4). The sample package was designed to be easy to fabricate, reusable and cleanable so multiple device can be tested without cross-contaminations. It consisted of a bottom layer of polymethyl methacrylate (PMMA) with a window containing the actuating element, a middle layer of PDMS reproducing the layout of the channels and the chamber, a window of glass and a top layer in PMMA. As already mentioned, PDMS was also used to isolate the electrical elements from the liquid environment. The PDMS layer and the chip were held together between two PMMA slides by custom-made clamps. Since fluids were diffused into the microfluidic channel and not injected using a pump, light mechanical pressure was sufficient to ensure good sealing of the different layers.

An important feature of this package is that sample can be easily removed from the liquid chamber. After each experiment, channels and chamber were cleaned in isopropanol, which does not damage the material. The glass layer (a thin coverslip - 0.17 mm thickness) provided the top face of the liquid chamber, enabled the view of the sample by optical setup and presented inlet and outlet port. All package layers were aligned with each other using some markers printed on each one of them.

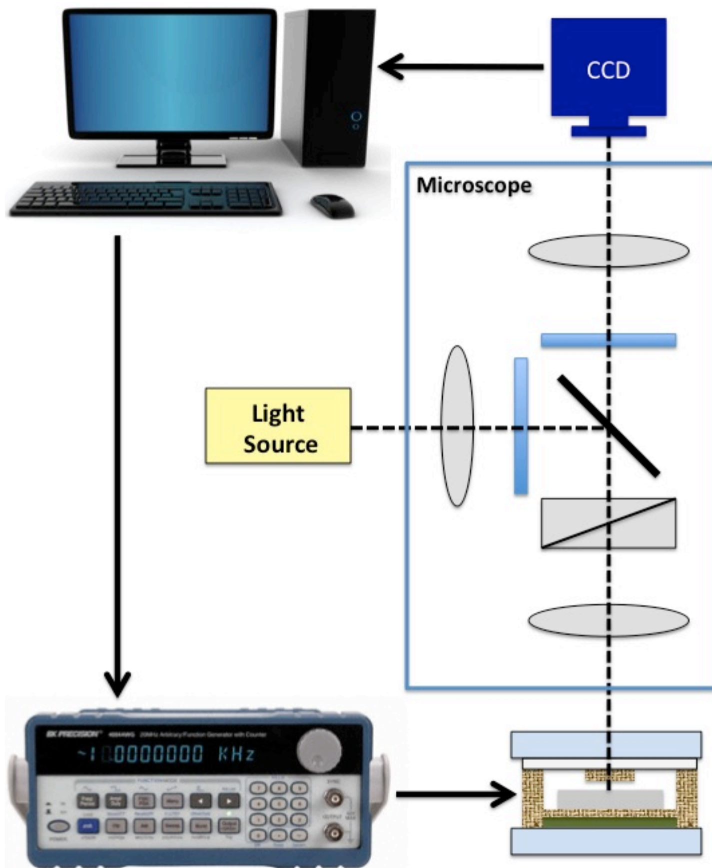

Fig. 3-3. Schematic of DIC measurement system containing equipment for image acquisition, analogue and digital image processing, image display and recording.

Liquid flow plays an important role in mass measurement applications, since it increases the developing on chemical bonding between different substances. At the same time, it does not have to modify MEMS mechanical properties. In most cases of microdevices, flow can be considered laminar and the velocity profile is continuous at the boundary between the fluid and the wall, i.e. the fluid has zero velocity relative to the boundary. This assumption is called the no-slip condition. Reynolds number (*Re*), which is the ratio of the inertial forces to the viscous forces, can be used to characterize the flow and, in microfluidic device, it is usually below 100 [3-5]. For rectangular channels, it is given by:

$$\mathrm{Re} = \frac{\rho v}{\mu}\frac{2ab}{(a+b)} \tag{3-4}$$

where ρ is the fluid density, v is the flow velocity, μ is the fluid viscosity and a and b are the cross sectional

dimensions of the channel. As systems are made smaller, inertia becomes even less relevant and, without its non-linearity, straightforward microfluidic systems have regular, deterministic flow [3-6] that impacts on our resonant structures. Since fluid density and viscosity can be assumed constant, *Re* is function of the flow velocity and the channel dimensions. Our microfluidic device was made out of a chamber (700 μm deep, 1 mm width and length), which contains the sample, and two channels (100 μm deep), which allow liquid income and outcome. For our design, note that the water density and viscosity are 997 kg/cm^3 and 8.9 10^{-4} Pa•s at 25 °C, respectively, *Re* is 100 when the flow velocity is less than 10^{-4} m/s. Under these operating conditions, a typical laminar flow is found for liquid analysis on our MEMS sensors. The need of low velocity of water flow, caused by our channel implementation, dictates a quasi-static liquid condition for our experiments, in order to avoid any non-linear phenomenon. If we consider an average sample dimension of 5x5x0.5 mm, the total liquid hold in the chamber is 22,5 μl. Liquid (deionized water - DI) was placed in the input well with a pipette and was sucked into the channel over the sample. All layers were cutted and patterned with a glass-tube laser-cutting machine (GLC NS5040W). After the cutting, layers were cleaned in water and isopropanol to remove remaining dust.

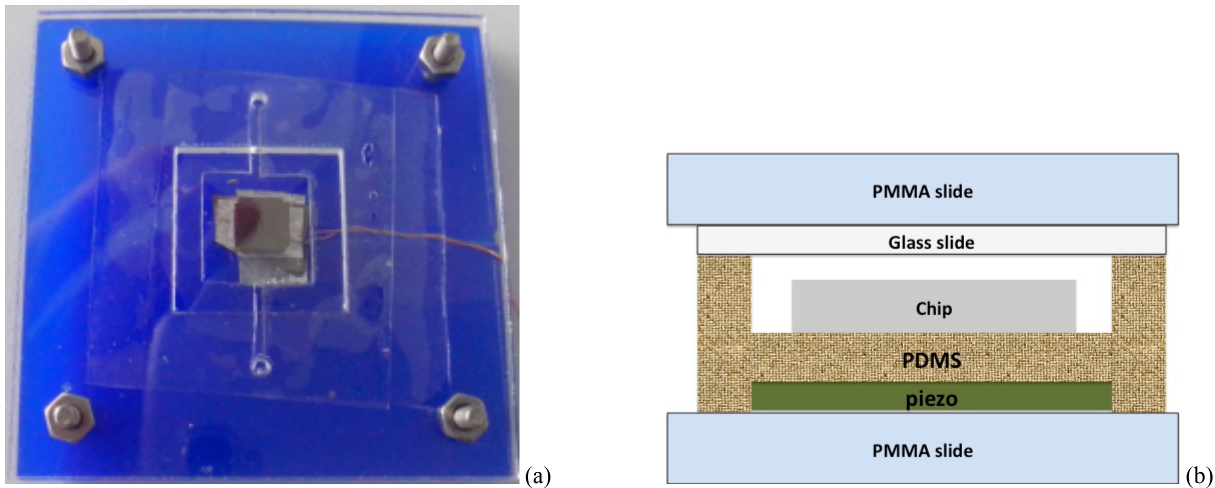

Fig. 3-4. (a) Picture of the sample holder and **(b)** cross section of assembled package along the fluidic channel.

A computer, with dedicated software, controls the actuation elements and performs interferogram processing. A more details description of the developed software can be find in subparagraph 4.2.2.. When a sinusoidally vibrating object under test is illuminated by continuous radiation and the time of interference image registration is much longer that the vibration period, intensity distribution in the interferogram can be described by the equation [3-7]:

$$I_{aver}(x,y) = I_0(x,y)\left\{1 + K(x,y)J_0\left(\frac{4\pi}{\lambda}a(x,y)\right)\cos\left[\Delta\varphi(x,y)\right]\right\} \quad (3\text{-}5)$$

where I_0 is the sum of interfering beams, K the contrast, J_0 the Bessel function of the first kind and zero order, a the amplitude and $\Delta\varphi$ the phase difference between the interfering beam. Thus image contrast depends on vibration amplitude. When using a narrow spectral linewidth microscope, changes in the interference pattern can be used to roughly estimate cantilever vertical displacement upon the detection of a sample by counting the number of fringes (either minima or maxima) [3-8]. In order to do that, narrow bandpass filter has to be introduced in the optical path of our setup, between light source and collector. One drawback of filter integration is reduction on the light intensity of the image and increase noise interference on the measures.

3.1.2. Cantilever in air

Three identical coupled silicon nitride cantilevers (three coupled cantilevers - TCC) [3-9] were tested in air. This device consists in three nearly identical cantilevers coupled at their fixed end by means of an overhang. In order to understand the physics of this system, each cantilever can be model as a damped harmonic oscillator while the effect of the coupling can be model with springs connecting each oscillator to the others [3-10]. When cantilevers are identical, each mode, which, with zero coupling, is threefold degenerate, is splitted in three independent modes with well-defined symmetry. In the first mode, at the lowest resonance frequency, the three cantilevers oscillate in phase. However, manufacturing tolerance and material variations cause the properties of the cantilevers to differ from another and, therefore, one cantilever could oscillate more than the others. An example is reported in figure 3-5, where a gold layer, deposited on one lateral pillar, modifies system symmetry. Oscillation modes of a TCC device made of three cantilevers of 2 μm thick, 50 μm long and 20 μm wide were first observed with SEM. The device was glued to a piezoelectric crystal by bi adhesive tape and electrically isolated from the vacuum chamber. An actuation signal was applied by polished copper wires and vacuum feed-throughs. The pressure inside the microscope chamber was about $5 \cdot 10^{-6}$ Torr. Frequency scans were performed (from 350 kHz to 400 kHz) and three modes were identified with no information on vibrating relative directions or, in other words, phase/anti-phase behaviour (figure 3-5). In particular, for increasing frequency, it was observed the first mode where only one of the lateral cantilevers vibrates while the others do not move, the second mode where two cantilevers (inner and lateral one) oscillate and the third mode where all cantilevers move.

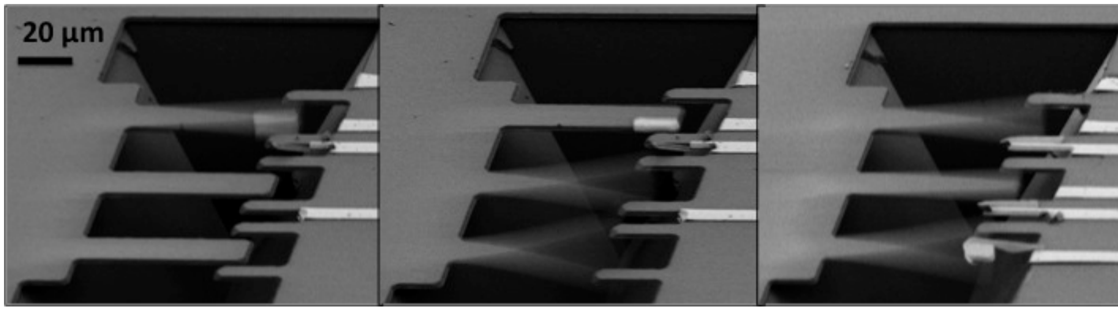

Fig. 3-5. Observation of cantilever displacements through SEM. Sample was tilted of 60° and actuated with 10 V_{PP} sinusoidal signal. Pictures were captured at different frequencies.

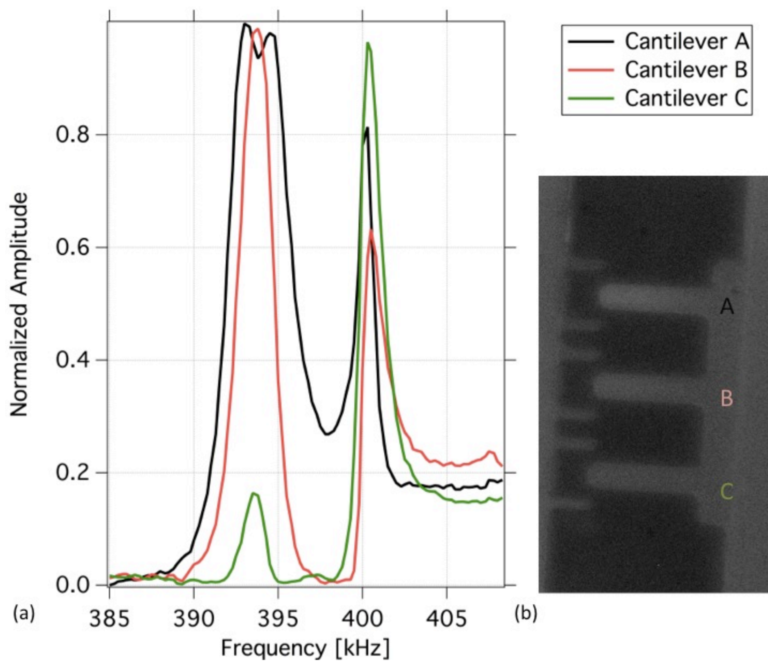

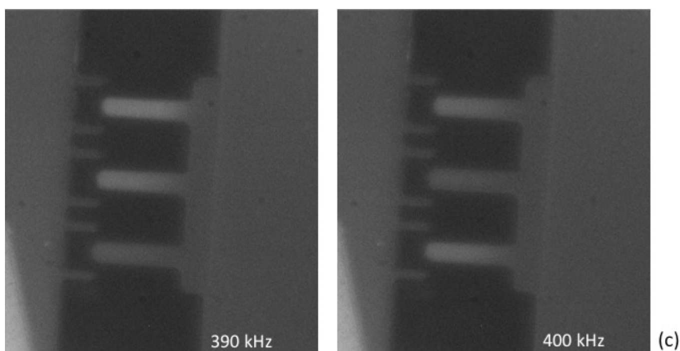

Fig. 3-6. Results obtain in air for TCC sample. **(a)** Frequency response of the different ROI. **(b)** CCD image of the sample under test, where the different regions of interest (ROI) are marked with colour squares and **(c)** sequence of images captured on frequency peak positions.

To avoid artefacts due to gold layer on cantilever tip, a TCC with no metal deposition was placed in the PDMS holder described on chapter 3.1.1. and observed with DIC instrumentation. The movements of cantilevers were recorder simultaneously and the results are presented in figure 3-6 (a). CCD snapshots taken at the two resonant frequencies are displayed in figure3-6 (c) as a further help to figure out the actual motion of the cantilevers. At 393 kHz, all cantilevers oscillated in phase but with different amplitudes. By looking in detail at device behaviour (figure 3-6 (c)), we observed how cantilevers A and B presented displacements that are transferred to cantilever C by mechanical coupling. The second mode was detected at 400 kHz, where the central cantilever only slightly moves, while the two lateral cantilevers oscillate with almost equal amplitude. In this scenario, cantilever B was mechanically induced to vibration by lateral cantilevers movements and this was confirmed by its reduced displacement.

It is worth to notice here that, from previous optical lever method measurements, in the second mode cantilevers A and C move in opposite directions. However, since the DIC method only records the intensity difference, only an absolute difference signal, regardless of the up or down directions is recorded. Moreover, since this method averages over many oscillation cycles, the phase information is also not acquired.

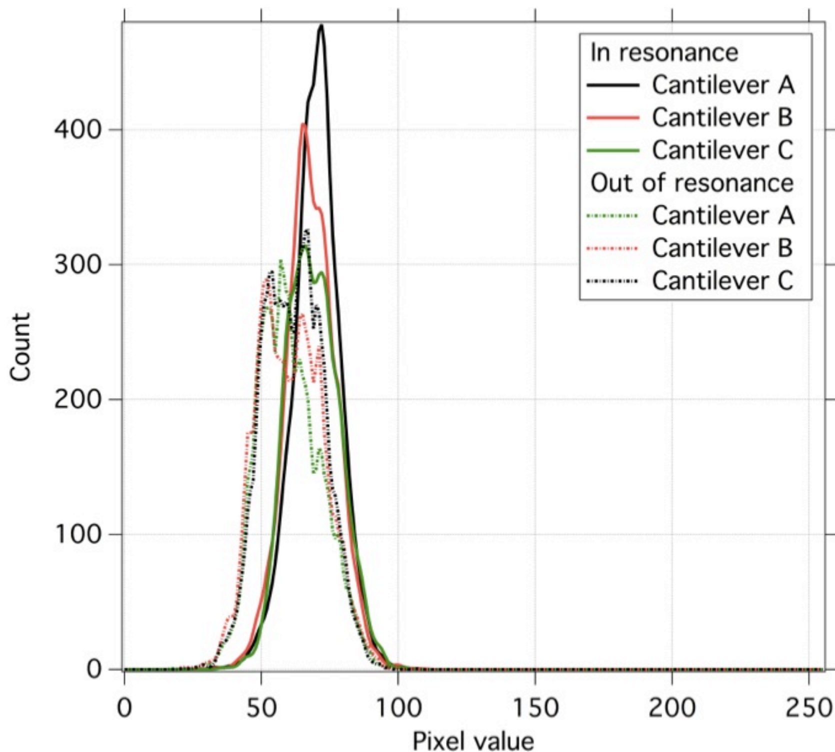

Fig 3-7. Cantilever histograms in and out of resonance frequency.

During scans, for each cantilever, we considered sensor total vibrating area as region of interest, derived the number of pixel for each tonal value (histogram) and saved the data into a text file. As shown in figure 3-7, histograms reported different behaviour in and out resonance mode and the curves were analyzed to find the characteristic parameter that better discriminate between the two operating mode (in and out of resonance) of the resonator. We took into account mean, confidence intervals for the mean, standard deviation, kurtosis, skewness, maximum value and compared them in terms of S/N and accuracy of the measurement. Standard deviation shown the best results with a ratio between resonance amplitude and average dispersion of data for a no-peak signal (S/N) of 14.6 and accuracy on peak location of $\pm 1.5 \cdot \Delta f$, where Δf is the frequency scans step.

3.1.3. Cantilever in liquid

In order to test DIC method in liquid environment, a different mechanical resonator was taken under consideration. The operation in liquid reduces the sensor quality factor and the oscillation amplitude because of the viscous damping [3-11]. One promising approach to overcome the challenges of liquid sensing for the first out-of-plane flexural mode is the use of u-shape cantilever [3-12]. Cantilever was obtained from silicon nitride membrane and the formation of a meniscus in the groove restricted the wetting of the sensors at one side of it, reducing the viscous damping. More details on device fabrication can be found in [3-12]. The spectral response of this device was tested in air and liquid with DIC setup described in the paragraph 4.1.1. To investigate cantilever behaviour, mechanical excitation was applied at difference amplitude and frequency scans were performed with step of 50 Hz. A tape was stuck on sample base to block liquid and to avoid cantilever total wetting while the space between the chamber walls and the cantilever was filled with DI water. As mentioned before, measurements were performed in static environment and liquid entrances were blocked with plastic paraffin film to limit water evaporation during the experiments.

A typical frequency response of a u-shape device in its first vibrating mode in air is shown in figure 3-8, for various driving voltages. Actuation signal has to be strong enough to induce cantilever oscillation but has not to introduce cantilever mechanical non-linearities, optical artefacts and thermal phenomena. Indeed, by increasing actuation amplitude, cantilever displacement on z direction increases as well and, by applying actuation voltages above 5 V_{PP}, a non-linear behaviour is recorded. An example of non-linearity is presented in figure 3-8 (c), where over-actuation modifies cantilever physical properties, which leads to a shift on frequency resonance peak and a typical saw-toothed shape [3-13]. Over-actuation can also cause thermal heating of the device by Joule effect on piezo electrical contacts. As a consequence, undesired damages of PMMA package and of the liquid

under test can take place. Moreover, when cantilever displacement on z direction exceeds n•λ/4, where λ is the wavelength of microscope light source, the optical waves interference switches from constructive to destructive, and vice versa. In other word, in the region of interest, the optical analyzer sums the intensities of the twin images generated by DIC polarizer, instead of subtracting them. As shown in figure 3-8 (d) a change in wave interference during frequency scans is converted into a change in curve trend and, as a result, resonance curves displayed negative peaks. Frequency response with multiple peaks can be recorded and this optical artefact should be avoided by applying low actuation voltages.

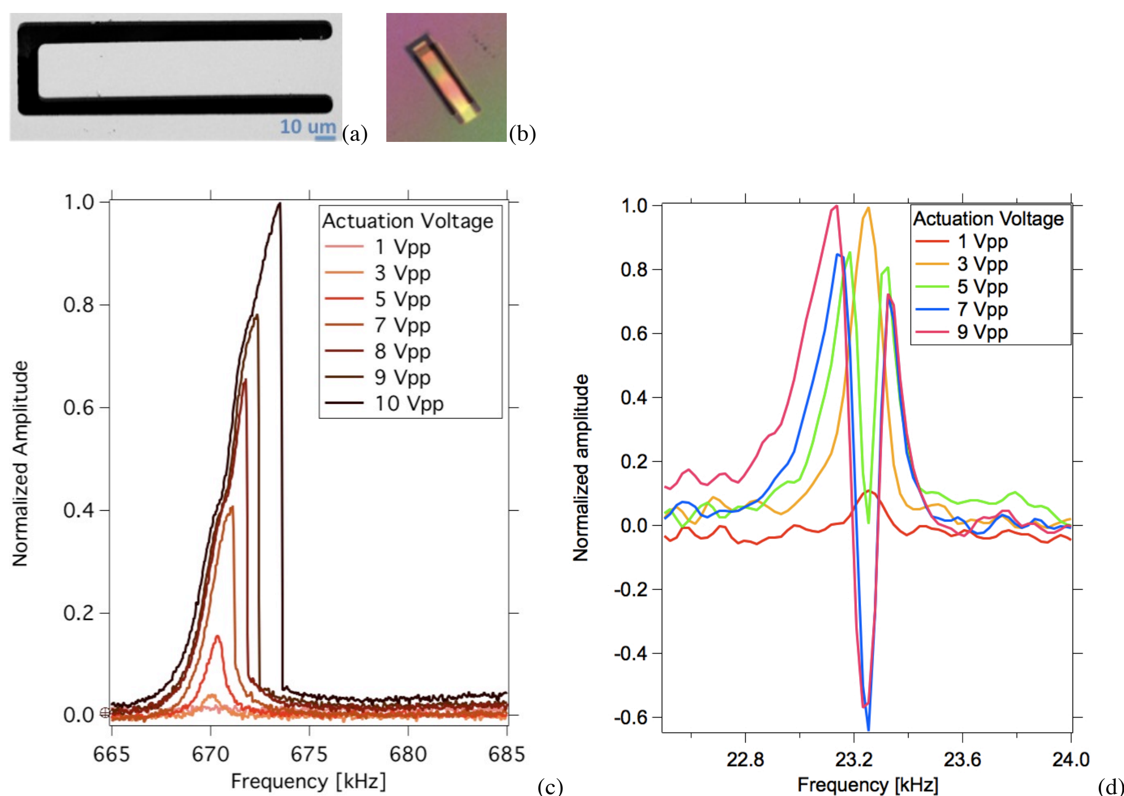

Fig. 3-8. (a) SEM and **(b)** CCD images of a u-shape cantilever. Cantilever is 175x30x2 µm and presents a gold deposition on its backside to enhance light reflection and facilitate the measurement. Gold can be use for further sensor functionalization. Non-linear frequency response: in air **(c)** over-actuation of the cantilever and **(d)** optical artefacts.

Cantilever structures 2 µm thick, 175 µm long and 30 µm wide were fabricated for measurements in liquid environment. At low actuation voltage cantilever response can be fitted with a Lorentzian function and, under air, the devices show a resonant frequency around 650-750 kHz, with a quality factor range of 400-750. The same cantilever was tested in air and immersed in DI water, under the same actuation conditions (10 V_{PP},

frequency steps of 50 Hz). Resonance frequency shifted from 713 kHz to 212 kHz, with a drop of the quality factor by a factor of about 30, owed to the added fluid mass and the viscous loss. The results confirmed the restriction of the wetting to the top surface of the cantilever and agree with theoretical model [3-14]. Indeed our cantilever shown a quality factor bigger than 10, which cannot be associated with the frequency response of a cantilever completely immersed in liquid.

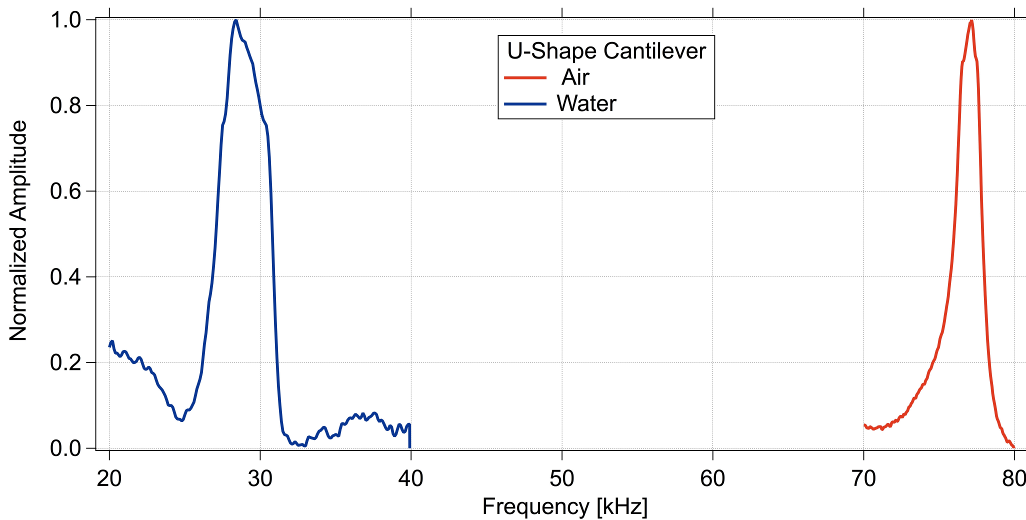

Fig. 3-9. Frequency response of an u-shape cantilever, in air and in liquid.

Furthermore, we were not able to observe sensor movements in a complete wet condition, since cantilever displacements were moderated by water damping affects.

3.2. LIGHT INTENSITY MEASUREMENTS

DIC technique shows good results in both air and liquid environments but presented several limitations. Optical view of the sample and re-composition of the polarized images are strictly linked to objective focal length and magnification. Furthermore, just a limited number of cantilevers can be tested simultaneously. Under these considerations, a second optical configuration was developed and improvements on MEMS fabrication were made in order to maximize parallel detection of sensor arrays.

Thanks to their vertical structure, pillars are suitable for high dense array configuration. Moreover, it was demonstrated that a regular matrix of pillars with a surrounding frame may result in a super hydrophobic surface

and induced a droplet to be on Cassie state [3-15]. Contact angle between 100° and 150° can be measured.

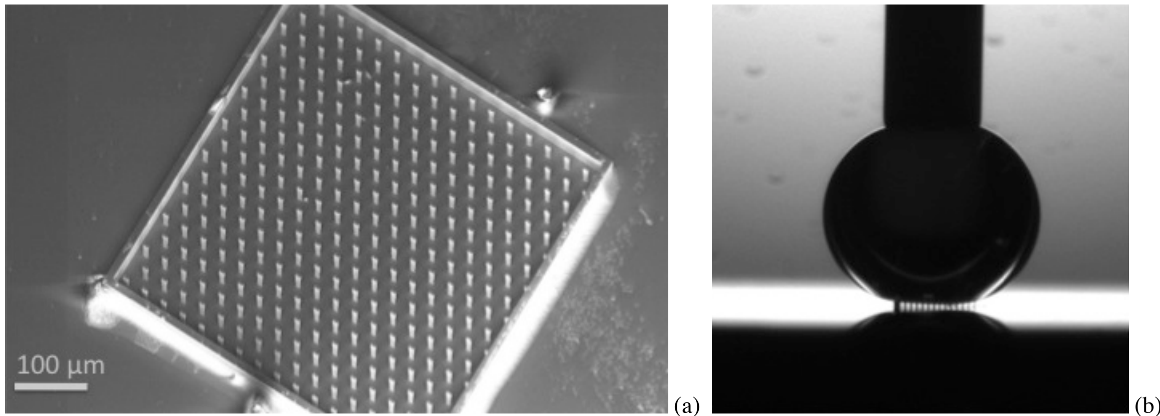

Fig. 3-10. (a) SEM image of an array of pillars surrounded by a protection frame. **(b)** Hydrophobic test performed on the sample in order to quantify its contact angle [1-59].

All these aspects make pillar array an excellent candidate for multiple resonance frequencies detection by optical setup and CCD camera.

3.2.1. Acquisition system

The implemented optical setup is shown in figure 3-11 and was built using *Thorlabs* cage system. Four steel rods acted as rigid armature and allowed aligning all optical components with a common optical axis. The setup served the purpose to visualize by means of a CCD camera the device and involved a long working distance microscope objective. 100 W halogen lamp acted as the illumination source. To reproduce Koehler illumination and ensure the best resolution, contrast and bright operating condition, the lamp was coupled with an optical fiber and a lens (3). A cubic beam splitter (4) divided the incident and the reflective light while a tube lens (2) (focal lens 200 mm) was used to correct the infinity focus of the objective. The sample was placed in a vacuum chamber in order to maximize oscillation amplitude. As it will be discussed in a following subparagraph, light intensity results were compared to optical deflection ones. It follows that the two setups needed to be integrated. A DPSS green laser (532 nm) was added to the white light in the optical path by a second beam splitter (11) and a 10x beam expander (12) was placed between the laser and the beam splitter to illuminate the entrance pupil of the objective. A mirror (8), after the tube lens (7), was used to direct the light either to the photodetector (14) or to a CCD camera (10).

While optical system was fixed, sample was moved by moving the entire chamber. By means of xy micrometrical translation stage and a lab jack, it was possible to scan and focalize the sample. The sample holder lodged 4 samples at a time and actuation was performed by piezo-electric crystal. Bi adhesive tape was used to glue samples to the crystals.

In order to generate an even and high illumination of the sample measured by CCD pixel, we improved the efficient transmission of light through the optical path. The efficiency of light transmission within the optical system is primarily a function of the transmission properties of the objective lens and of the number of optical elements in the system. For example, uncoated lens surfaces typically reflect 4–5% of the light incident upon them. Therefore, all unnecessary optical elements were removed from the light path. The light gathering ability of the optical setup is also a direct function of the numerical aperture (N.A.) of the objective lens. The importance of this point is clearly appreciated when one considers the relationship of magnification, numerical aperture, and light intensity [3-16]:

$$I \propto \frac{(N.A.)^4}{Mag^2} \tag{3-6}$$

The demand of high N.A. should be clear to capture more light. On our setup, an Olympus objective (LMPLANFL 50x / 0.5) with 10.6 mm working distance was employed.

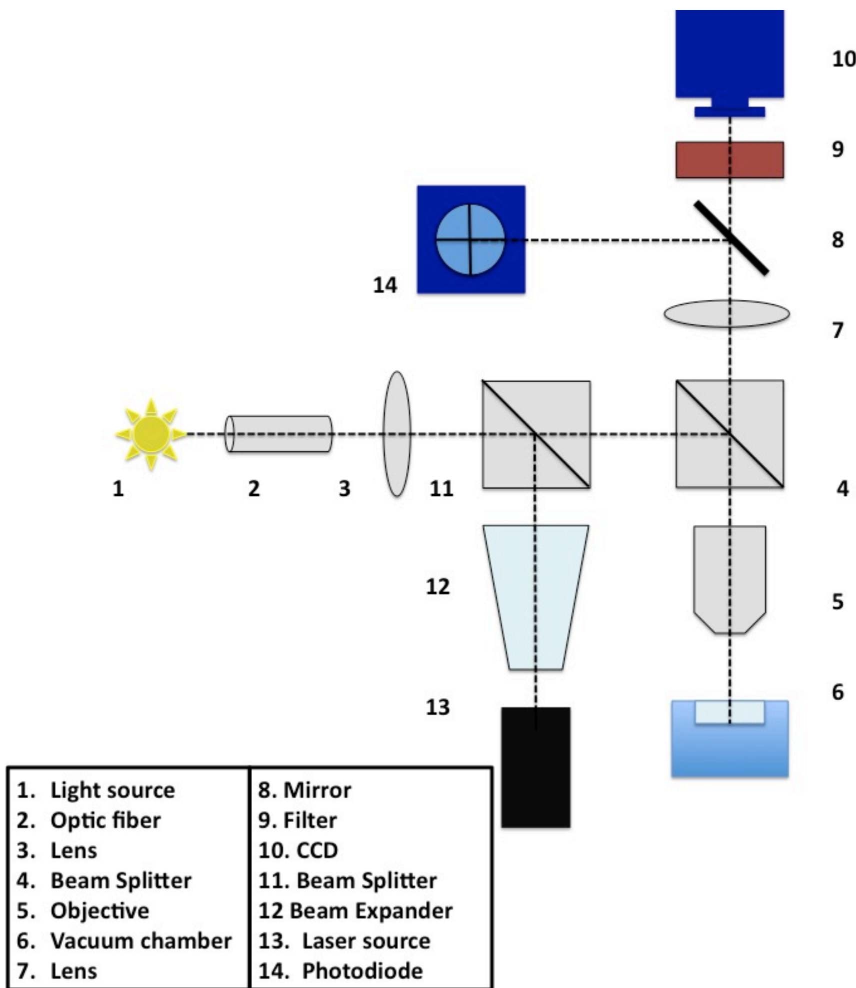

Fig. 3-11. Scheme of the experimental setup.

3.2.2. Data acquisition and elaboration

The Optical setup previously described in previous paragraph was tested on a cluster of pillar arrays obtained from Si wafer. Details of the fabrication procedure are reported elsewhere [1-59]. Pillar shows rectangular base less than 1 μm on its shorter side, to increase oscillation amplitude, and gold top, which offers excellent (98%-99%) reflectivity throughout the infrared. Gold was also used as mask for further silicon wet etching, aimed to reduce pillar base without compromising its top dimension.

An example of the fabricated matrix is presented in figure 3-12. Pillars were arranged with hexagonal lattice pattern and inserted into a frame that surrounds the whole array in order to protect the sensors from mechanical

damages and prevent solution diffusion from the sides of the matrix. We considered pillars in the middle of matrix to avoid frame interferences during fabricative process. When pillar enters in resonance mode, the direction of the reflected light changes and CCD converts this information into a change of light intensity, since the amount of photons detected by pixel decrease (as shown in the black box into figure 3-12).

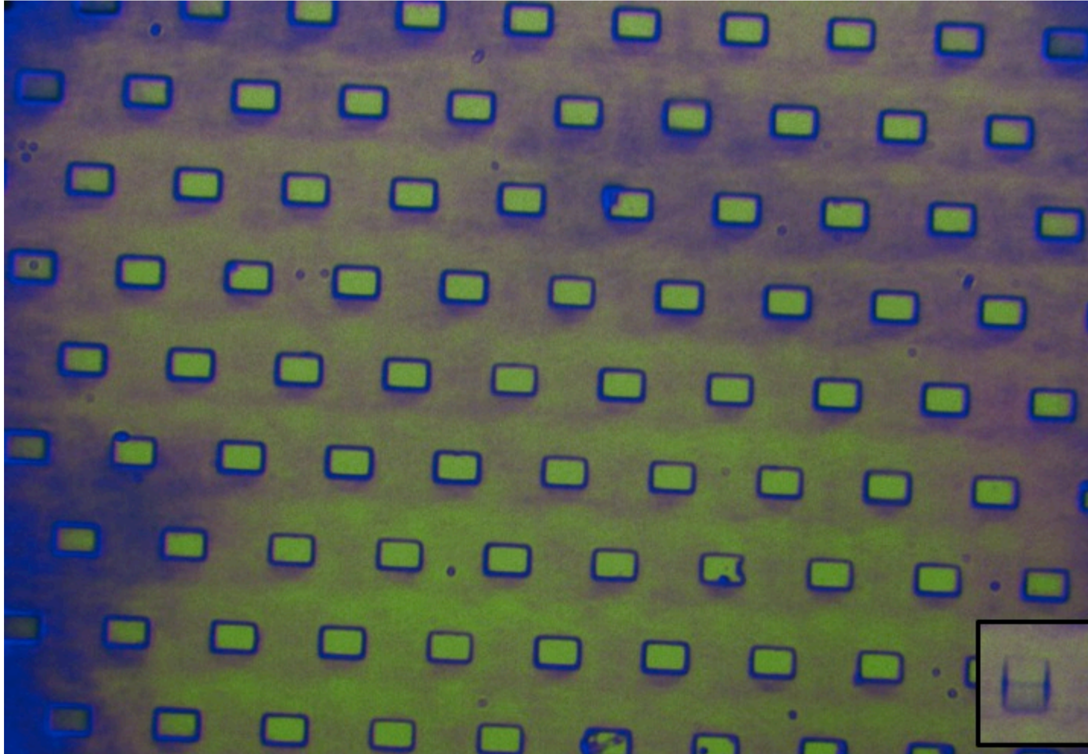

Fig. 3-12. CCD image of an array of matrix made by 19 x 16 pillars and, in the black box in the bottom-right corner, an example of oscillating pillar.

In order to speed sample analysis, data acquisition was managed by LabVIEW software while the elaboration was performed by *Igor PRO*. LabVIEW offers a free driver (NI-IMAQ), which allows to acquire and to configure driver software and hardware (analog, parallel digital, Camera Link cameras as well as general electronic instrumentations). However it is not a powerful tool for numerical computation, analysis and development algorithms to create models, like *Igor PRO*.

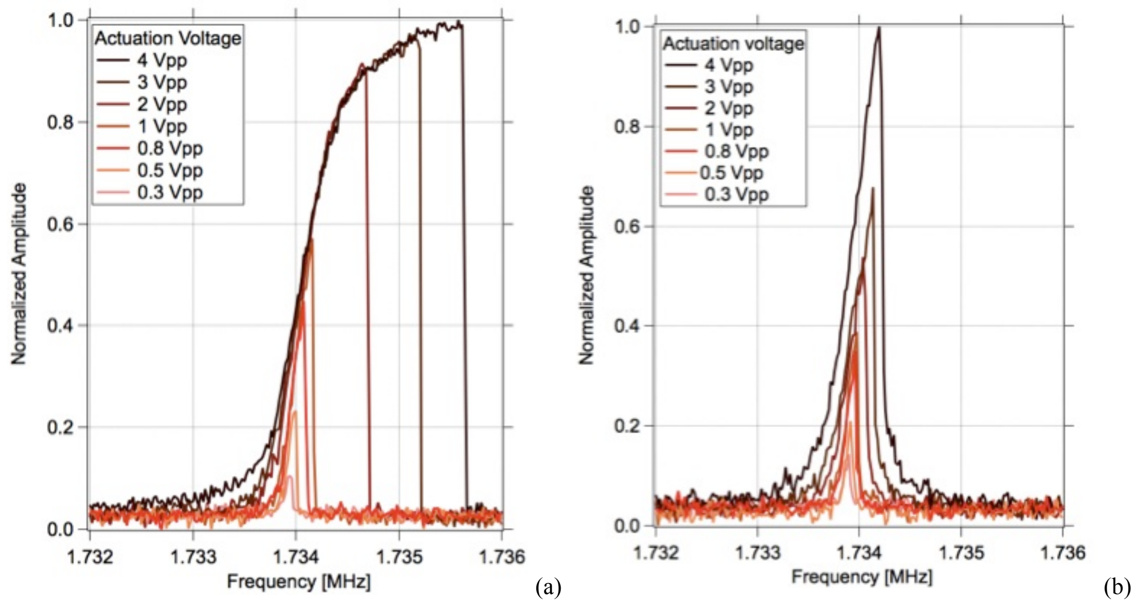

Fig. 3-13. Over-actuation of pillar sample during positive **(a)** and negative **(b)** scans performed at different actuation voltages.

After focusing the specimen and correcting light source intensity, CCD camera was configured (gain and offset), so part of the specimen of interest displays the most information, and background image was acquired and placed in memory (*image0*). Manually, we defined scans parameters (actuation voltage as well as start, stop and step frequencies) and selected the region on interest (ROI - the top end of the pillars) for data acquisition and further analysis during the scans process. ROI coordinates were saved and reference ROI (*ROI0*), where no-vibration takes place, was specified. At every frequency steps, LabVIEW software captured specimen image and, for each ROIs, estimated RGB-histograms, analyzed data and saved the result into a text file. In particular LabVIEW performed:

- Mottle subtraction: To eliminate inhomogeneities in background brightness and patterns of image imperfections, an initial image of the blank wafer (*image0*) can be stored in memory and then subtracted from each frame of the incoming video signal.
- Enhancement of motion by sequential subtraction: In order to observe and detect only moving elements, ROI data obtained from a reference image was subtracted from those acquired frame by frame. This method only worked satisfactorily with a very stable setup.
- Light noise: Since light source does not present DC power stabilizer, intensity shown irregular behaviour and *ROI0* data was used as background information that can be subtract to original data and offer S/N improvement.

Data were saved in raw and elaborated versions and loaded on *Igor* where further elaborations were performed. For every ROI, we performed Lorentzian fitting and estimated resonance frequency and *Q-facto*r. Over-actuation of MEMS resonator can cause the shift of resonance frequency to higher value due to a non-linear contribution of resonator stiffness, as reported in figure 3-13. This asymmetrical behaviour is presented in both positive and negative scans and, over an actuation range of 0.2-4 V_{PP}, the average peak frequency shift artefacts is 1.95 kHz and 940 Hz, respectively. In order to estimate the analyte mass correctly, *Igor* we defined a symmetry parameter α as:

$$\alpha = \frac{\Delta f_1}{\Delta f_2} = \frac{f_0 - f_1}{f_2 - f_0} \tag{3-7}$$

where f_1 and f_2 are the frequencies where the amplitude of pillar oscillation is – 3 dB the one at resonant frequency. Parameter α is function of the actuation voltage and value closes to 1 identifies symmetrical condition. In the cases reported in figure 3-13, α ranges on 0.21-1.2 for negative and 10.8-25 for positive scans. It follows that negative frequency scans have to be preferred for mass sensing applications.

3.2.2. Results and comparison with optical lever technique

Samples described in chapter 3.2.1. were tested under vacuum (10^{-6} mbar) with an actuation voltage of 6 V_{PP}. A preliminary frequency scans was performed from 2.5 to 2.75 MHz and 29 pillars were selected and tested simultaneously, using their tops as ROI. The obtained results are reported in figure 3-14, where 8 pillars shown a resonance negative peak on the considered range of frequency. CCD converts light information into an unsigned 8-bit integer value while the peak negative value is caused by the reduction of detected photon from the CCD and by the subtraction of the reference ROI to reduce signal noise and. In fact, the pillar area is smaller than cantilever one, making the signal noisier. Moreover, pillar resonance movements modified the reflection index of the sensing surface, which is converted into a reduction of light intensity. The entire test took less than 5 minutes, which is an outstanding result compared to the acquisition time of deflection mode, where the detection of a single pillar can took more than 1 minute.

The green component shows a higher resonance peak compare to red and blue ones. This is due both to higher number green sensors in CCD camera and to pillar gold top, which gives excellent reflectivity through the infrared and limited reflectivity at wavelength shorter than 550 nm. Light-intensity technique results and its sensibility on frequency shift detection were compared with those obtain with conventional optical deflection

mode. In fact, to characterize our setup and define the quality of its measurements we must quantify its precision. As mentioned before in chapter 3.2.1., the results obtain with our setup were compared with those obtained with deflection mode technique, under the same operating conditions. 34 pillars, with an average resonance frequency of 1.385 MHz and biological sample on their top, were measured with both techniques. The absence of a clean metal layer on pillar is typical in biological analysis and we wanted to test our setup in the most common operating conditions. The resonance frequencies detected with deflection mode and intensity light setup shown an average deviation of 290 Hz. This result is connected to cross-talk phenomenon between sample and detection mode, which alters the measurement. In particular, with the optical deflection technique, sample was illuminated with a 100 mW green laser, which warmed the sample and caused the onset of degassing phenomenon. On the other hand, our light source was a 10-50 W bulb halogen lamp, whose light was decrease during the optical path and evenly distributed over the sample.

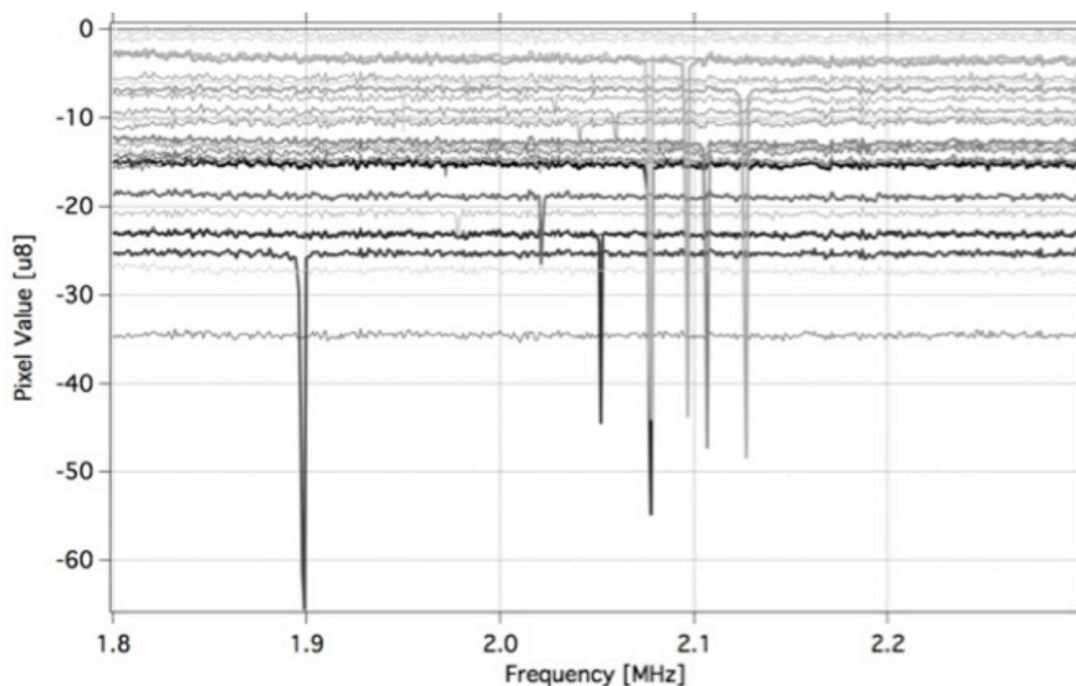

Fig. 3-14. Results obtained by scanning 28 pillars simultaneously.

The aim of light intensity setup is the detection of biomarkers thought mass sensing applications. For this reason, we deposited 1.5 nm of aluminium on the top of the previous 34 pillars and recorded the new frequency responses. Since the metal deposition is a well-controlled process by a calibrated microbalance inside the e-beam evaporator, we know the amount of the added material and we correlated it with the change in resonance

frequency, obtaining the sensitivity factor:

$$\beta = \Delta m_{Al} \Delta f_{Al} = hS\rho_{Al} \Delta f_{Al} \quad (3\text{-}8)$$

where S is the pillar top surface, h is the thickness of the gold layer , ρ_{Al} is the aluminium density and Δf_{Al} the variation of resonance frequency after the deposition. We deposited on our sensors a mass of 54.67 fg. As suggested by equation 1-6, frequency dependency to sample mass has a square root trend but, for small amount of deposited analyte, it can be approximated as linear. Intensity light measurement reported mass sensitivity of $3.1 \bullet 10^{16}$ and a total frequency shift of 1.7 kHz. Metal deposition improved both light intensity and deflection detection performances and the measurements performed with the two techniques differed between each other of 109 Hz on the definition of the resonance frequencies. Moreover, deflection mode reported a frequency shift of 1.9 kHz but since, it shown more cross-talk phenomenon with the sample than light intensity mode, its measurement of the frequency response is less accurate.

Another important feature of measurement setup is the repeatability of a measurement system or, in other words, the degree to which repeated measurements under unchanged conditions show the same results. In order to quantify this parameter, we tested a pillar with aluminium deposition on its top face, actuated it with several actuation voltages and, for each one of them, we performed 5 measurements of the frequency response. Frequency scans presented a step (Δf) of 20 Hz, which is consistent with the mass measurement application this setup is design for, and we considered the maximum amplitude frequency as the resonance one.

Blue component exhibited the worst performance while the set up showed an average repeatability of $1.8 \bullet \Delta f$ Hz, with a contribution to uncertainty of $0.5 \bullet \Delta f$. In other words, the repeatability depend on function generator frequency step and, in our experiment, it is equal to repeatability in mass measurements of 10 fg, which are promising for biological mass-sensor application.

3.3. SUMMARY AND DISCUSSIONS

We developed two different optical setups to measure MEMS resonator in vacuum and liquid environment. Our approaches for MEMS detection in dynamic mode overcome most of the limitations of the conventional optical measurement methods described above. For both setups, we performed initial characterization to identify the best parameter of discrimination between vibration and static condition.

In DIC measurements, instead of a custom-made optical setup, we used a standard microscope with a digital

camera controlled by a PC. Provided that sensors are in the field of view of the camera, the response of a whole array of sensors can be captured and no optical optimization is needed. On the other hand, with light intensity measurements, we were able to measure 29 pillars in parallel in less than 5 minutes. Moreover, the results confirmed s limited cross-talking effect between light intensity technique and resonator mechanical behaviour, making this measurement method promising for MEMS applications in air and liquid environment. All instrumentations were controlled by LabVIEW program while we elaborated data by dedicated Igor macro.

In contrast with MEMS using integrating displacement sensors, our devices are much simpler to fabricate and do not require external electrical connections. Moreover these methods can be greatly improved by further automation of image acquisition and analysis and resonators can be adapted for a variety of sensing applications by using an appropriate biomolecular coating.

REFERENCES

[3-1] G. Nomarski, “Interféromètre à polarisation”, French Patent 1.059.123, 1952.

[3-2] R. Danz and P. Gretscher, “C–DIC: a new microscopy method for rational study of phase structures in incident light arrangement”, Thin Solid Films, vol. 462, pp. 257–262, 2004.

[3-3] W. Lang, “Nomarski differential interference-contrast microscopy, II. Formation of interference image”, Zeiss information, vol. 70, pp.12–16, 1969.

[3-4] E.D. Salmon and P. Tran, “High-resolution video-enhanced differential interference contrast light microscopy”, Methods in Cell Biology, vol. 81, no. 6, pp. 335–364, 2007.

[3-5] C. Xing, C. Dafu, C. Haoyuan, L. Hui, S. Jianhai and Z. Lulu Zhang, “MEMS-based microdevice for cell lysis and DNA extraction”, Microelectromechanical Systems and Devices, InTech, vol. 2, pp. 22-38, 2012.

[3-6] T. M. Squires, “Microfluidics : Fluid physics at the nanoliter scale”, Review of Modern Physics, vol. 77, no. 3, pp. 977-1026, 2005.

[3-7] J. Kacperski and M. Kujawińska, "Direct visualization of vibration modes of microobjects using an LCoS SLM in a Twyman-Green interferometer", Photonics Letters of Poland, vol. 2, no. 1, pp. 49-51, 2010.

[3-8] S.T. Koev, W.E. Bentley and R. Ghodssi, "Interferometric readout of multiple cantilever sensors in liquid samples", Sensors and Actuators B, vol. 146, pp. 245–252, 2010.

[3-9] H. Pakdast and M: Lazzarino, “Triple coupled cantilever systems for mass detection and localization”, Sensors and Actuators A: Physical, vol. 175, pp. 127–131, 2012.

[3-10] M. Spletzer, A. Raman, A.Q. Wu, X. Xu and R. Reifenberger, "Ultrasensitive mass sensing using mode localization in coupled microcantilevers", Applied Physics Letters, vol. 88, issue 254102, 2006.

[3-11] M.K. Ghatkesar, T. Braun, V. Barwich, J.P. Ramseyer, C. Gerber, M. Hegner and H.P. Lang, "Resonating modes of vibrating microcantilevers in liquid", Applied Physics Letters, vol. 92, issue 043106, 2008.

[3-12] J. Linden and E. Oesterschulze, “Improving the quality factor of cantilevers in viscous fluids by the adaptation of their interface”, Applied Physics Letters, vol. 100, issue 113511, 2012.

[3-13] B. Ilic, S. Krylov, M. Kondratovich and H.G. Craighead, "Selective vibrational detachment of microspheres using optically excited in-plane motion of nanomechanical Bbams", Nano Letters, vol. 7, no. 8, pp. 2171-2177, 2007.

[3-14] C. Vancura, Y. Li, J. Lichtenberg, K.U. Kirstein, A. Hierlemann and F. Josse, "Liquid-phase chemical and biochemical detection using fully integrated magnetically actuated complementary metal oxide semiconductor resonant cantilever sensor systems", Analytical Chemistry, vol. 79, no. 4, pp. 1645-1654, 2007.

[3-15] M. Melli, G. Scoles, and M. Lazzarino, “Fast detection of biomolecules in diffusion-limited regime using micromechanical pillars”, ACS Nano, vol. 5, issue 10, pp. 7928–7935. 2011.

[3-16] D.G. Weiss, W. Maile, R.A. Wick, and W. Steffen, “Video microscopy”, Light Microscopy in Biology: A Practical Approach, pp. 72-122, 1999.

4. ELECTRIC ACTUATION AND READOUT ON PILLAR

As already mentioned in chapter 1, one of the MEMS devices studied in this thesis consists of an array of pillars with tapered design. To use it as a mass sensor in real-time applications, the resonance frequencies of multiple pillars have to be measured in parallel while the sample to analyze is subjected to different biological and physical treatments.

In the previous chapter we investigated optical readout techniques to detect multiple MEMS movements while in this chapter we want to address the attention on the development of new electronic strategies to interface pillars with common laboratory instrumentations. Indeed, this is a not a trivial task since, due to their characteristic vertical geometry and fabrication process, the most common electrical excitation and readout methods, such as electrostatic actuation, piezoresistivity or piezoelectricity, cannot be used. One actuation method that can be easily applied to pillar arrays consists in vibrating the whole chip, which is coupled to a macroscopic piezo-electric element. However, in this way, all the pillars are stimulated at the same time and it is impossible to selectively stimulate one resonator at the time. This behaviour can hinder several device applications, especially when simultaneous optical observation of the sample is required (e.g. SEM). Furthermore, a common practice used to attach piezo-crystal and sample involves bi adhesive tape or paste, which does not guarantee a uniform and consistent mechanical coupling.

The possibility to use an electronic detection approach would relax the alignment procedures required by laser and, more in general, optical detections. Moreover it is suitable to further integration in an all-in-one device, which includes, on the same chip, the actuation, the sensing system and the detection system. One possible readout strategy, which can be applied on vertical structures, involves the use of hard contact method. In this configuration, during resonance, the pillar hits a nearby electrode. Indeed, in principle, it is possible to detect pillar resonance frequency by measuring the time average current flowing from one electrode to the other through a pillar using simple low bandwidth electronics. At the same time, single actuation of pillar can be achieve by Kelvin polarization force, which does not need any electrical connections to the dielectric resonator. In this configuration, pillar is enclosed into two electrodes and it can be easily integrate with hard contact method by properly adding the needed electrodes to device layout.

Since the main aim of this work was to obtain a full integration of pillars with on-chip electronic actuation and detection system, measurements on pillar were performed in vacuum and both actuation and readout layouts, as

well as electronic setup, were not designed to operate inside a viscous medium. Nevertheless this goal can be reach by slightly modifying device design and fabrication.

4.1. ELECTRIC ACTUATION

From the actuation point of view, a recent publication [4-1] introduced an alternative dielectric route to the universal excitation of microelectromechanical sensors and decoupled resonator from excitation components. When a polarizable object is placed is a non-uniform electric field, a force is applied on it. This force does not require the object to be charge and its intensity depends on the object electrical and geometrical properties, as much as on the frequency of the electric field. The same physical principle, in different spectral range, is used to investigate electrical properties of the sample and, in particular, in the optical tweezers, it is used to hold and move micrometer-sized particles. Indeed, as the relative polarizabilities of the particle are frequency-dependent, varying polarizing signal and measuring the way in which the force changes can be used to investigate and characterized the dielectric properties of the object itself. In practice, the electric field polarizes the particle and the resulting poles experience a force along the field lines, which can be attractive or repulsive, according to the orientation of the dipole.

Kelvin force can occur in both AC and DC electric fields and, if we consider a pillar located in between two electrodes, the actuation is directly related to pillar position and to the intensity of the polarization. For this reason, it is of interest to understand the best geometrical operating conditions and how the voltage bias dependence on the resonance frequency affects the resonator performances.

4.1.1. Dielectric material and polarization force

When a neutral object is polarized and placed is a non-uniform quasi-static electric field, a dielectric force is applied on it. The polarization is responsible for force generation and is the cause of the translational movements of the object. At the same time the force experienced by the object is a function of the material properties of the involved dielectrics. From a microscopic view, if we consider an infinitesimal dipole, the dielectric force acting on it can be express as [4-2, 4-3]:

$$F = p \bullet \nabla E \tag{4-1}$$

where p is the dipole moment and E is the electric field. When E is homogeneous, its gradient results equal to

zero and no force is applied. From a macroscopic point of view, the polarization force acting on an object can be calculated by means of the polarization bulk force. Kelvin polarization force density can be written as:

$$f_{KP} = \frac{1}{2}\varepsilon_0(\varepsilon_r - 1)\nabla(E \bullet E) \tag{4-2}$$

where ε_0 is the vacuum dielectric constant and ε_r is the sensor dielectric constant. It follow that, in order to quantify the Kelvin polarization force acting on a dielectric object (F_{KP}), the analytical expression of f_{KP} must be integrated on the entire volume of the object under study and this operation requires the knowledge of E inside the material. Equation 4-2 depicts that the strength of the force depends on the polarizability, on the volume of the attracted medium and on the field intensity squared. In an aqueous environment, however, charges, bound ions and a diffuse double layer create electric shells at the interface between the object and the water [4-4]. These induced charges alter the net polarization of a dielectric object. We choose to operate in vacuum to remove the air or liquid dissipation contribution and to better investigate the effect of the actuation mechanism on the resonance quality factor and frequency for pillar resonator. Even thought liquid dissipation effect is not treated in this work, it has to be considered in an application where a dielectric is surrounded by water or biological liquid.

Based on this actuation scheme, dielectric microresonators made from polymeric materials (SU8) have been successfully actuated in vacuum [4-1], air and DI water [4-5]. In this last configuration, gold electrodes were covered with a 120-nm thick insulating layer of aluminium oxide in order to eliminate electrolysis reactions in water and an effective quality factor of 31 was obtained.

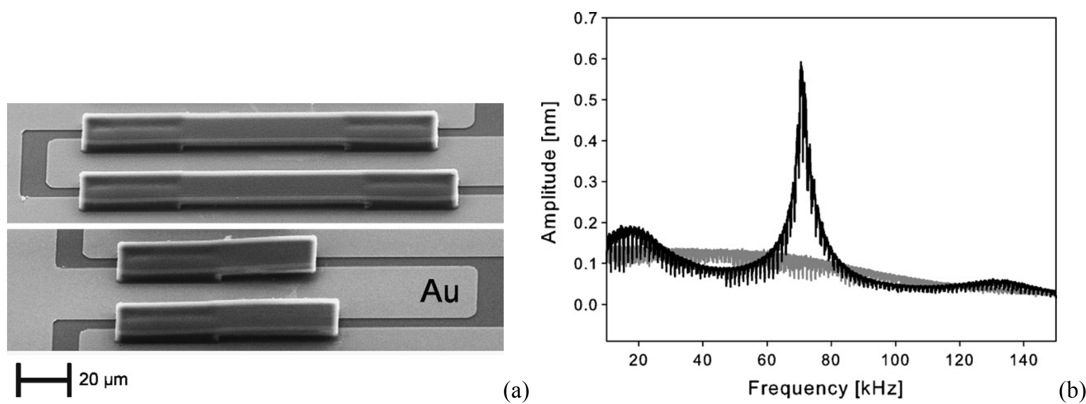

Fig. 4-1. (a) SEM image and **(b)** amplitude response of a SU-8 cantilever in water [4-5].

4.1.2. Analytical model and simulation results

In order to understand pillar behaviour on different physical conditions and the relationship between pillar displacement and Kelvin polarization force, finite element analysis simulations were performed with the commercial software package COMSOL. The proposed actuation configuration consisted of four major components: a tapered pillar 15 μm tall characterized by a top face with a rectangular geometry (size of 8x3 μm), two external electrodes and an inner one. The gap between the electrodes and the pillar resonator was set to 500 nm to ensure a successful etching of the silicon layer by the Bosch^{TM} process. Two electrodes were sufficient to develop the Kelvin polarization force but a third electrode was introduced in the geometry to study the effects of a non-symmetric electric field on the pillar. In order to maximize the actuation force intensity applied on the resonator, we performed a 2D simulation under the assumption that all the relevant parameters involved (i.e. pillar-electrode geometry and separation) do not depend on z, and thus the more realistic 3D results can be obtained extrapolating the 2D model. The entire model structure is schematized in figure 4-2 (b) and it consists of four monocrystalline silicon blocks in vacuum. The parameter *g,* shown with a black marker, is the displacement of the pillar in the y direction from the electrodes edge. When the dielectric pillar is introduced into the electric field it gets polarized and, in return, it alters the field, which remains symmetric but looses its rounded shape inside and nearby the pillar. By reversing the actuation principle, the motion of the resonator can be electrically detect by observing the changes of electrodes capacitance and converting them into an electric signal. In this way the frequency response of the system can be recorded. We investigated:

- The variations of electrical capacity caused by pillar displacements, under the assumption of using the external electrodes as plates of a capacitor.
- The Kelvin polarization force applied on a pillar located at different distances from the external electrodes.
- The effect of non-symmetrical electric filed.

By varying *g* from -5 μm to 5 μm, the 2D capacitance of the whole pillar and electrodes system reported a change of 47 pF/m, which is much less than the parasitic capacity of the system, package and cables included. In fact, package parasitic capacitors typically range around 1-5 pF, making hard the detection of any significant signal.

The influence on the Kelvin polarization force of the pillar position *g* within the two electrodes was evaluated. Figure 4-3 shows the polarization force in vacuum calculated by integrating the force density on the pillar top surface [Eq. 4-2], with a differential voltage applied on the electrode of 20 V_{DC}.

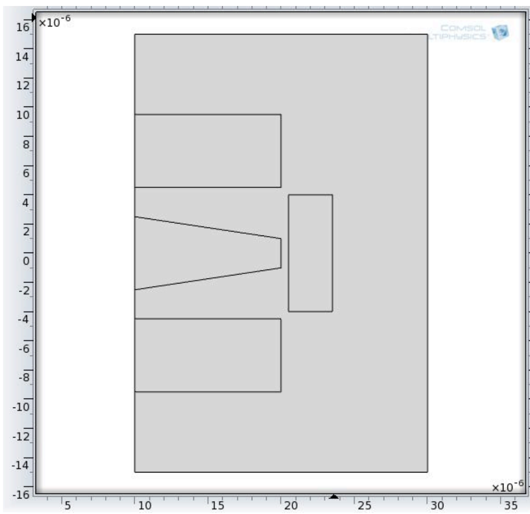

Fig. 4-2. 2D schematic drawing of the MEMS sensor for the modelling of the F_{KP} on pillar top. It consists of the external electrodes, the inner electrode, the pillar and the vacuum chamber

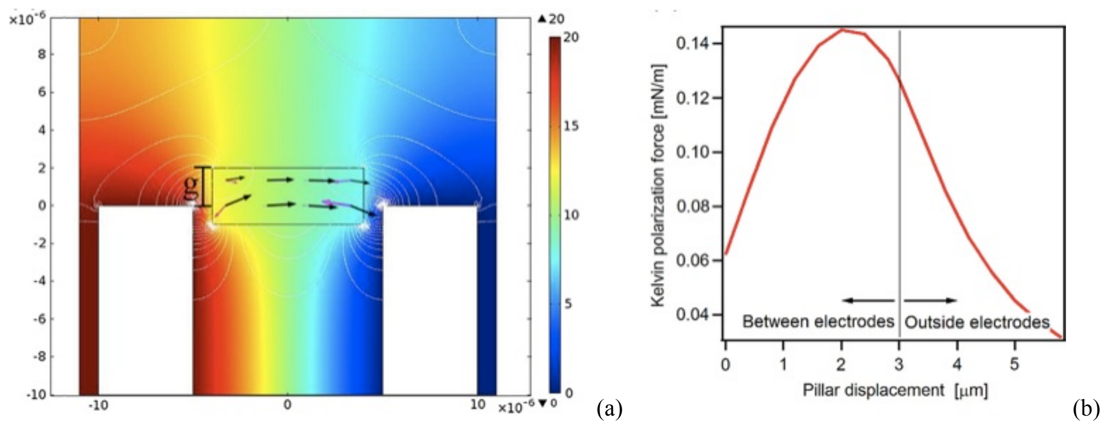

Fig. 4-3. (a) 2D schematic drawing of the electric potential (*V*) for the Kelvin polarization force modelling. The white lines represent the electric field (*E*) while the black arrows indicate the local polarization (*P*). **(b)** F_{KP} plotted against the displacement *g* of the dielectric in vacuum.

The pillar experienced a force parallel to the electrode plates and the maximum for Kelvin polarization force developed by the system was reached at *g* equal to 1 µm (figure 4-3 (b)). Integrating the obtained result on the z dimension (under the assumption of operating with a 20 µm height pillar) the overall force in the y direction was 0.25 nN. A typical map of the electric potential distribution obtained with COMSOL is shown in figure 4-3 (a),

where the inner electrode does not interference with the physical simulation.

We also investigated pillar behaviour when inner electrode was used to actuate the pillar by V_{DC}, RF voltage was applied to one lateral electrode and the other one was connected to electric ground. Figure 4-4 (a) shows a map of the electric field when pillar is polarized under these assumptions. We noticed that the largest electric field gradients were localized at the edges of the structures. We evaluated the electric field magnitude and the polarization magnitude at the positions indicated with the letter "A" and "B" in the map. The dependences of ||E|| and ||P|| on V_{DC} are displayed in figure 4-4 (b) and 4-4 (c). Both curves, calculated in the point market with "A" in the figure, show a minimum for V_{DC} = 13 while those related to position "B" are monotonic. It is clear that the presence of more than two electrodes and the break of the symmetry in the actuation potential require a detailed simulation of the actuation mechanism if we aim at setting properly all the parameters.

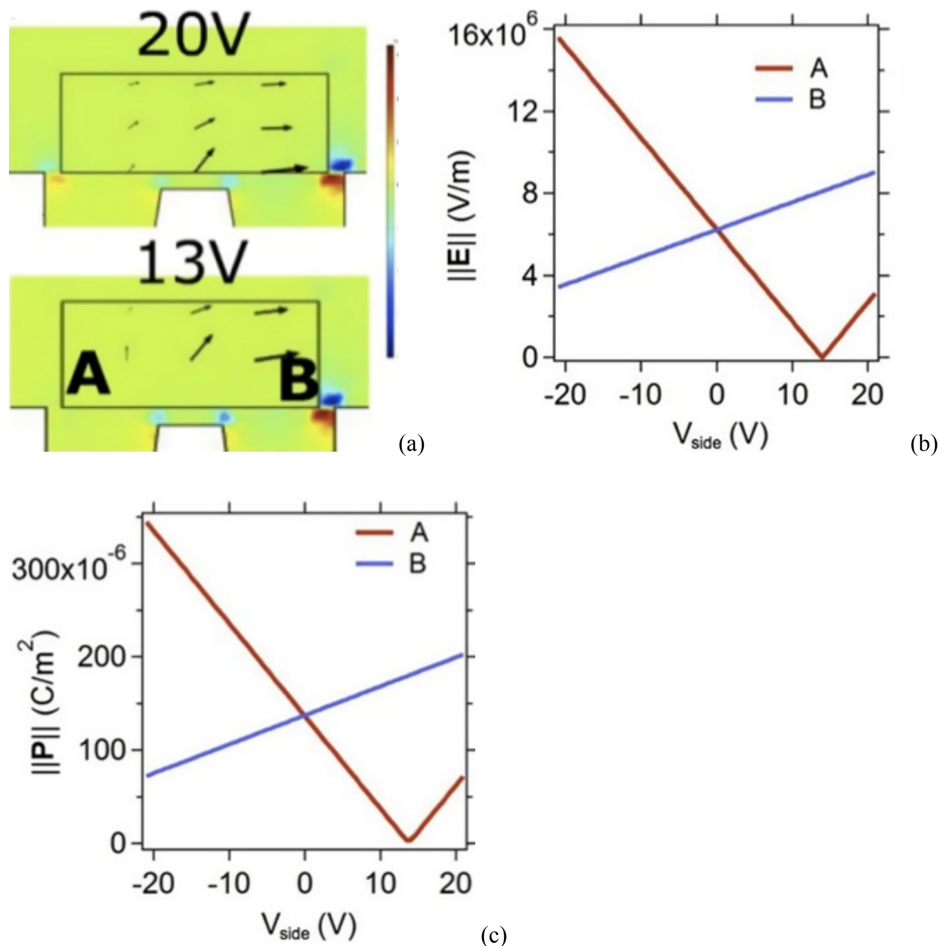

Fig. 4-4. (a) Finite element analysis when inner electrode is at 20 and 13 V, respectively. **(b) (c)** Modulus of the electric field and of the polarization vector calculated at the pillar corners ''A'' and ''B'', as indicated in panel **(a)**.

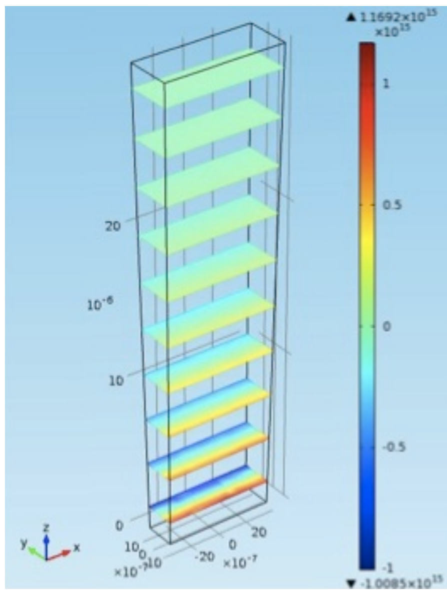

Fig. 4-5. Pillar stress distribution (N/m^2) during first resonance mode.

To investigate pillar mechanical behaviour and define the proper frequency scan range, we performed simulations on COMSOL frequency domain. In particular, by performing parametric simulations, pillar was dimensioned and the design parameters were chosen to operate it above 10 MHz. Indeed, resonance frequency is proportional to base thickness and, as a consequence, is a function of the initial cross-section and of the length of the pillar. As shown in figure 4-5, the stress induced by the oscillation was confined on the base of the tapered pillar. On the contrary, from conventional cantilever design [4-6, 4-7], stress is equally distributed.

4.1.3. Fabrication

The fabrication consisted of two main processes: the definition of contacts and pillar cross-section by lithography and a deep anisotropic etching. A silicon on insulator (SOI) wafer composed of 15 µm thick p-doped monocrystalline silicon layer (100), a 2 µm thick buried oxide layer and a 500 µm thick handle silicon layer was the starting point. We decided to develop our device on SOI to take advantage of few silicon oxide properties. Indeed, not only SiO_2 guarantees the fabrication of vertical structures electrical independents to each other (electrodes and pillars) but it also allows practicing high control on pillar dimension by acting as stopping layer during silicon dry etching. Indeed, pillar height was defined by the thickness of the silicon layer in the SOI and etching process was optimized to guarantee a define undercut angle.

After piranha and HF cleaning, s1818 resist was spin coated and baked at 120 °C for 1 min. Large area contacts were later aligned using optical lithography, 18/100/20 nm Ni/Al/Ni multiplayer evaporation and lift-off. The sample was then spin coated with 500 nm of polymethylmethacrylate (PMMA) and baked for 10 min at 180 °C. The pillar rectangular geometry and the electrodes were defined by e-beam lithography. After PMMA developing, a 20 nm nickel layer was evaporated by means of e-beam. Lift-off process was performed with hot acetone to obtain the Ni mask for the subsequent plasma etching. Before the etching, oxygen plasma was performed in order to remove the residual resist and argon plasma was used to better define the metal mask. Finally, we performed a Bosch™ process to define the vertical pillar geometry with an inductively coupled plasma reactor (ICP, STS-Surface Technology). After annealing at 500 °C for 1 min, metal alloy was created and the device can be used. Figure 4-6 shows the final device obtained by fabrication process and pillar layout.

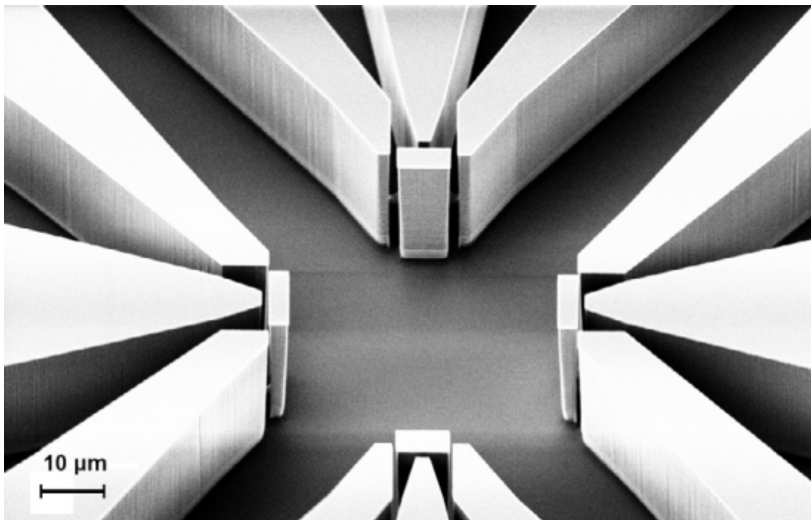

Fig. 4-6. SEM image of a microfabricated device with four pillars, each independently actuated by Kelvin force through three separated electrodes.

4.1.4. Experimental setup

Optical setup, based on deflection mode, was built to measure the resonance curve. The measurements were performed by placing the device in a vacuum chamber with pressure of about $1 \cdot 10^{-6}$ mbar. The electrical connections were realized by gluing the wafer to a dual in line (DIL) package and by connecting package pads and electrodes with thin gold wires and bonding machine. Bonding was performed at 120 °C and, to prevent damages of device structures, low force was applied. The communications with external instrumentation were ensured by a set of feed-throughs. We actuated the beam through a bias voltage (V_{DC}) coupled with an RF signal (V_{RF}). Indeed, from equation 4-2, it results that the Kelvin polarization force is linked to the applied differential voltage. In our configuration RF and DC voltages were coupled and the actuation force can be defined as [4-1]:

$$F(V_{DC}+V_{RF})=c_1\left(V_{DC}+V_{RF}\right)^2\approx c_1V_{DC}^2+2V_{DC}V_{RF} \tag{4-3}$$

where c_1 is a proportionality coefficient. High RF voltages signal are easily dispersed or affected by the environment noise, and the readout electronics should be able to discriminate the signal of interest based on its specific frequency. Moreover the RF generators are usually limited to low voltage output. A DC voltage, which alone does not produce any motion, was mixed with the RF component in this configuration (last term of Eq. 4-3): therefore, the V_{DC} can be used to amplify the effect of the RF signal. In order to obtain high actuation force and low RF noise, the DC component should be dominant. A network analyzer was used to generate the RF. The DC and the RF voltage are combined together using a tee-bias and the resulting signal is routed to the device under test. The resonance amplitude was probed by the optical lever method. A green laser (DPSS @ 532 nm) was focused on the top face of the pillar by using a long working distance microscope objective with 0.4 numerical aperture, and the reflected signal is detected by a four-quadrants photodetector (4QPD, Hamamatsu S7379-01), which presents a cut-off frequency of 80 MHz. The same optical set up was used with a white light source and a CCD camera to visualize the microresonator and to align the laser spot on the top of the pillar. The output of the 4QPD was compared with the RF signal by a network analyzer, and the resulting oscillation amplitude vs. frequency curve was obtained. The entire acquisition system was controlled by a LabVIEW application, which enabled multiple frequency scans for different polarization voltages and extracted the information on resonance frequency and *Q-factor*.

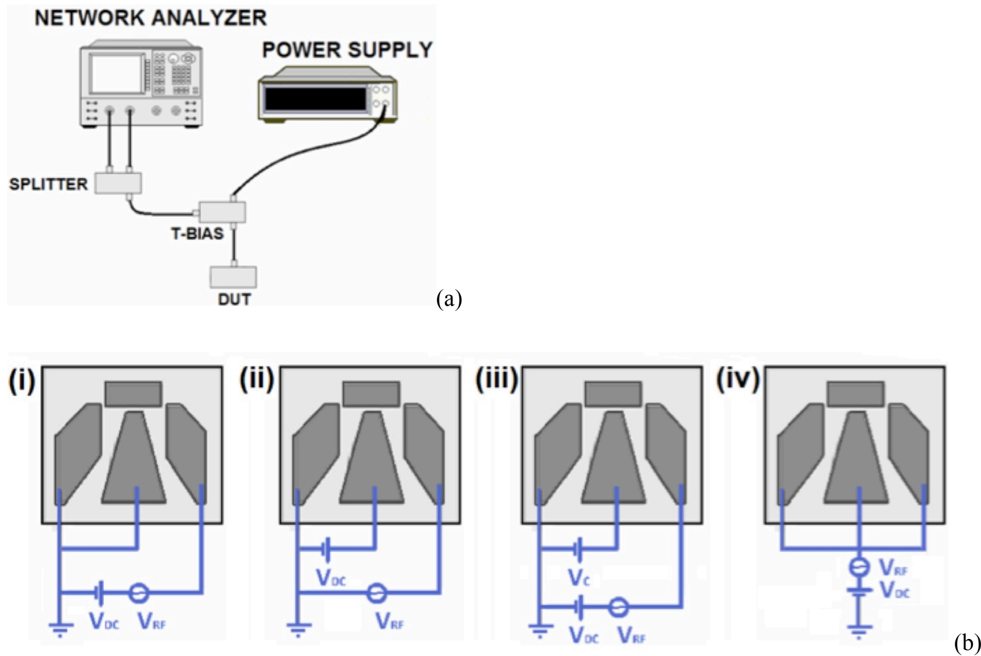

Fig. 4-7. Schematic of the actuation set-up. **(a)** The actuation system involved a network analyzer, a power supply and a tee-bias. **(b)** The four configurations used in this experiments

4.1.5. Experimental results

The resonance frequency of the pillars was preliminary investigated using a piezo-actuation (0.4-0.9 nF). The resonance frequency was 7.2±0.1 MHz, and the *Q-factor* was 9200± 70. The three independent contacts fabricated with sub-micron gaps allowed the investigation of four distinct configurations:

i. In the first, both signals (V_{RF} and a variable bias V_{DC}) are applied to a lateral electrode while the inner electrode and the other lateral electrode are grounded.
ii. In the second one signal was fed to a lateral electrode (for instance V_{RF}), the other signal to the inner electrode (i.e. V_{DC}), and again the third electrode was grounded.
iii. The third configuration was like (i) but here the central electrode was set to a positive fixed voltage (V_{CONST} = 20 V) while the other electrode was maintained at ground.
iv. In the last all three terminal were connected to V_{DC} and V_{RF}.

In all experiments V_{RF} was kept constant at 2 V_{PP} and V_{DC} was varied between -20 V and 20 V. Moreover in all configurations but (iv), left and right electrodes have been interchanged without observing significant

differences. All configurations are illustrated in figure 4-7 (b). We first focused on the configuration (iv) to rule out the possibility that the actuation we observed can be ascribed to a capacitive scheme. Indeed, in this configuration, with a nearly constant field, we did not observe any actuation. Configuration (ii), on the contrary, was effective. Resonance curves at increasing V_{DC} are shown in figure 4-8 (a). We observed that the resonance frequency does not depend on the applied bias and that the resonance shape is not affected by the increased bias. Indeed the *Q-factor* remains unchanged within 10% of indetermination at low DC voltages, which indicates that the Kelvin force actuation is a not dissipative process, and therefore is suitable to be applied to high *Q-factor* resonators. The resonance curves at 0 V_{DC} and V_{RF} = 2V_{PP} are still measurable although with very low amplitude and amplitude increases linearly with polarization voltages.

The maximum amplitude oscillation versus V_{DC} is plotted in figure 4-8 (b) for several sequential scans of V_{DC} from -20 V to 20 V with steps of 1 V. We first observed that the curves are superimposed. This means that no residual polarization is present in the devices, which is consistent with the absence of dissipation in the *Q factor* measurements. The minimum oscillation amplitude is for nonzero V_{DC}. This is explained considering that at V_{DC} = 0 the actuation is dominated by the V^2_{RF} term. The total actuation potential is minimized when $2V_{DC} = V_{RF}$. In the experiments V_{RF} was set to 1 V thus the minimum is for V_{DC} = 0.5V configuration. The same behaviour was obtained using the configuration (ii). The only difference was that in that case the minimum amplitude was obtained for V_{DC} = -0.5 V, for the system has a different symmetry and DC and RF voltage are subtracted rather than added. As already discussed, in configuration (i) V_{RF} and V_{DC} have been mixed using an RF bias-tee mixer, and then fed to the device. On the contrary, in the configuration (ii) they were supplied separately. The sensors response was identical, thus indicating that the three terminal configurations, when operated at the resonance frequency, behave as a micromechanical RF mixer. The configuration (iii) is characterized by a less intuitive behaviour. The oscillation amplitude versus V_{DC} is plotted in figure 4-9 (grey curve) together with the curve for configuration (i) (red curve). We first focused our attention to the maximum oscillation amplitude which, in configuration (iii), with an overall ΔV = 40V, is nearly a factor 1.5 larger than in configuration (i) with the same ΔV. This result suggests that higher actuation efficiency, with respect of two terminal configurations, can be obtained by an accurate tuning of electrode positioning and polarization. Second, the value of V_{DC} for which the oscillation amplitude is minimized is shifted at higher values. At a first sight, one would expect that a minimum is reached when V_{DC} = 20 V. At this value, lateral and central electrodes have the same DC bias. The RF modulation is applied between the lateral and the central electrode, and the latter screens the RF component with respect to the third electrode. The experimental results show instead that the minimum amplitude is reached for V_{DC} = 13 V. In agreement with FEM simulations, this specific case demonstrated that the description we adopted to simulate our device using the Kelvin force approach is adequate.

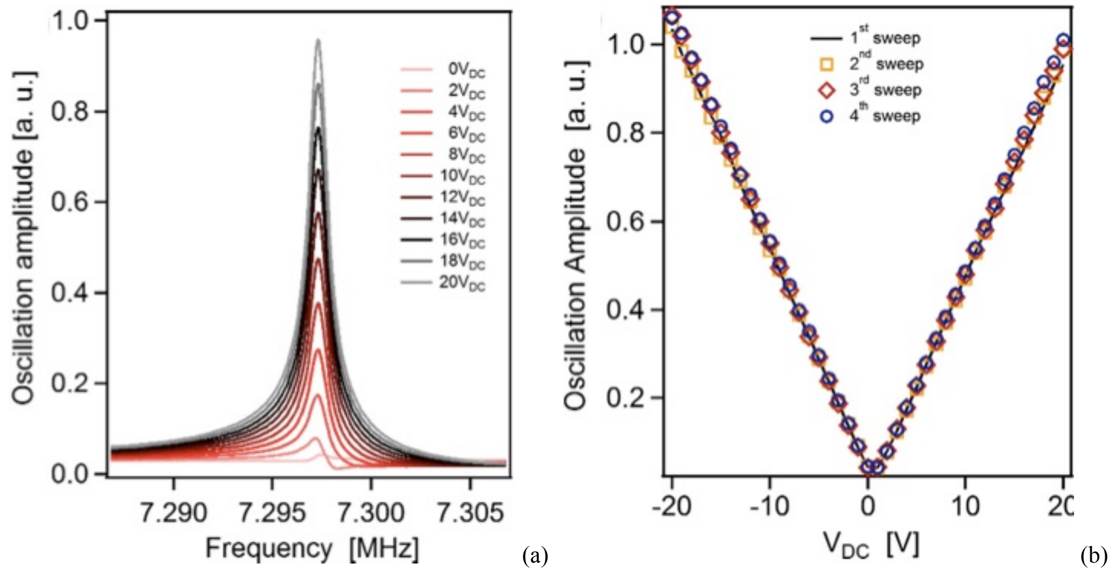

Fig. 4-8. (a) Resonance amplitude versus frequency with different polarization voltages acquired in configuration (ii). The oscillation amplitude depends linearly on the applied DC bias, while the resonance frequency remains unaffected. **(b)** Maximum oscillation amplitude vs. polarization voltage V_{DC} from four consecutive sweeps showing no hysteresis or charging effects.

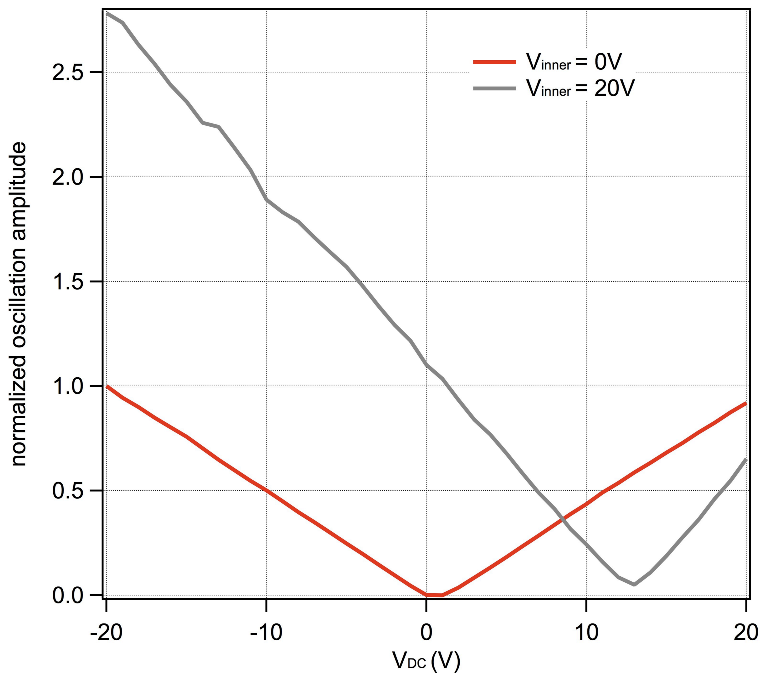

Fig. 4-9. Maximum oscillation amplitude as a function of V_{DC} in configuration (iii).

4.2. HARD CONTACT READOUT

As previously described, in optical detection the delicate alignment makes the system hard to use. Electronic detection relaxes the alignment requirements and can be highly compact but integration strategies have to be implemented. This aspect is critical for pillar geometry and fabrication process. Here we propose the detection of the resonant frequency by measuring the current flowing from one electrode to the other through the pillar during hard contact. Indeed, mechanical contact between electrode and pillar occurs once every cycle of the sensor vibration, giving birth to a pulsed electric signal. This technique has been already investigated for cantilever [4-8, 4-9] and disk [4-10, 4-11] applications, where the disk resonator operates as capacitive transducer. However on both these reports the contacts were bigger than those allowed by the geometrical constraints imposed by pillar layout.

The noise in mechanical systems is an unavoidable factor that influences every measurement. The source of noise present in a system originates from two different kinds of sources: thermo-mechanical noise and noise from measurement equipment [4-12]. The latter depends highly on the system, mode of operation and measurement parameters. Compared to other electrical setups implemented on MEMS resonators, one of the main advantages of this technique is the reduction of the noise sources of the measurement equipment.

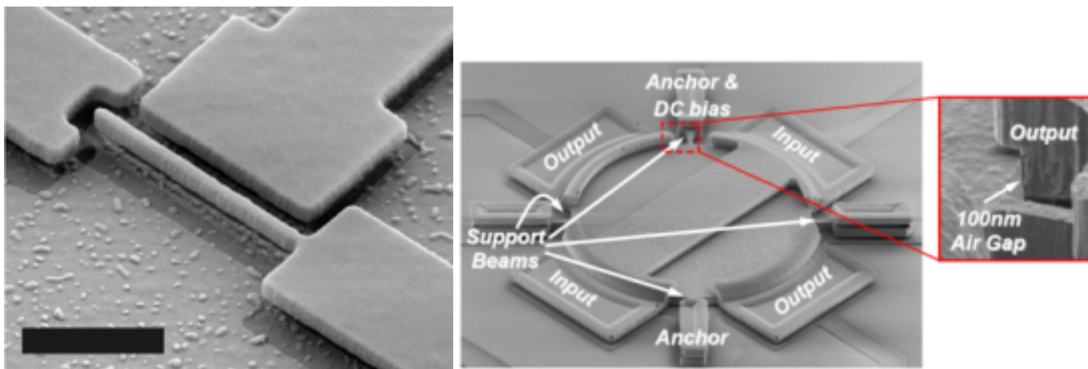

Fig. 4-9. (a) SEM images of the Si cantilever used in experiments on hard contact readout [4-13], with a scale bar of 2 µm. **(b)** SEM of the polysilicon disk and **(c)** zoom-in on the electrode-resonator gap of the device along the switch axis.

In electrical applications, in order to reduce noise, it is important that the primary conversion of frequency response to an electrical signal results in a large signal. In hard contact method the primary electrical output signal can be increase by acting on the DC voltage applied on one of the electrode, resulting in a signal higher than, for example, electron tunneling detection one ($I \approx 1pA$) [4-13].

4.2.1. Mechanical considerations

MEMS/NEMS operations often involve the formation of a mechanical contact between one or more moving parts. In these cases elastic or restoring forces should overcome adhesion forces otherwise these movable parts may remain attached together, hindering the further operations of the device: this effect is commonly known as "Sticktion effect". The elastic energy of a beam deflected is:

$$E_{ELASTIC} = \frac{1}{2}kd^2 = \frac{1}{8}\frac{Ewt^3d^2}{L^3} \qquad (4\text{-}4)$$

where d is the distance between the electrode and the resonator. The adhesive energy due to a contact area A_C is $A_C \bullet E_{ADH}$, where E_{ADH} depends strongly on the mechanisms involved in the adhesion. If the formation of covalent chemical bonds is involved, the order of magnitude of E_{ADH} is 1 J/m^2 [4-14]. These considerations lead to the geometrical design rule:

$$\lambda = \frac{1}{8}\frac{wt^3d^2}{L^3}\frac{E}{A_C E_{ADH}} > 1 \qquad (4\text{-}5)$$

where λ is a design parameter. If we consider nanometer size contacts and silicon resonator, A_C ranges from 2 to 10 nm^2 and dimensional parameter $wt^3/L^3 \bullet d^2$ must exceeds $0.025 \bullet 10^{-26}$ m^3. During contact, the average current measured with hard contact readout method depends on the contact resistance and on the ratio between contact time and cycle time. The second one is a function of the actuation voltage while the first one is a design parameter. A high conductivity metal coating needs to be applied to the pillar to ensure a low contact resistance and thus a detectable current.

During mechanical contact, resonator acts as a free and clamped pillar at the same time. Its movements are a superposition of multiple modes, which can lead to a temporary loss of contact between pillar and electrode. To define pillar frequency behaviour, we performed COMSOL simulations and determined the resonance frequency for a free and a clamped resonator. More in details, we considered a tapered pillar made of silicon with a 1x3 μm base and 15 μm height. In the model, resonator topside was in contact with a static wall and its resonance frequencies were determined with and without wall influence. The resonance frequency of a clamped pillar is $f_{CLAMPED} \cong n \bullet f_{FREE}$, where n depends on the operating mode and is 7.8 for the first one. Since contact time, t_C, is inversely proportional to $f_{CLAMPED}$ and the cycle time, T, is inversely proportional to f_{FREE} , it follows that:

$$t_C \alpha \frac{1}{f_{CLAMPED}} = \frac{T}{n} \quad (4\text{-}6)$$

Electronic devices, which have to handle primary signal, must present a bandwidth that include $f_{CLAMPED}$.

4.2.2. Fabrication

In order to ensure mechanical contact between pillar and electrode, pillars chip was placed in a SEM with electrical feed-throughts added to the vacuum chamber, to facilitate electrical connection to the PZT beneath pillars chip through shielded cables. Indeed, with the SEM it is possible to do accurate, visual measurements of the vibration amplitude, which can be used for determining the resonant frequency as well as the amplitude. The frequency response of a pillar with 1x3 μm base cross-section was previously measured using deflection mode under vacuum. SEM was pumped to a vacuum of $5 \bullet 10^{-6}$mbar and the device was piezo-actuated with 10 V_{PP} sinusoidal signal. Figure 4-10 shows the results obtained. Outside its resonance frequency, the image displays a blur of about 230 nm, due to the motion of the piezo under actuation. Since this motion affects rigidly the whole chip, no contact is generated. At the resonance frequency, the image of the solely pillar displays a 210 nm larger blur, that we attributed to the actual oscillation of the pillar. In this way the oscillation amplitude was evaluated. By reducing dimension of cross-section fixed end of the beam, vibrating amplitude may be further increased, to match with device requirements.

The important parameters to consider during the design phase are the resonant frequency and the coating of the pillar, as well as the sticktion phenomenon. The resonant frequency scales with the thickness and the inverse of height and its maximum value is dictated by the capability of the readout circuitry. Also sticktion coefficient is linked to pillar geometry. With the above considerations in mind, it follows that an important design parameter is the ratio between thickness and height, where the minimum value is imposed by sticktion restrictions. The design dimensions of pillar are listed in table 4-1. Height range from 15 to 25 μm while width of pillar base was kept constant to 800 nm in order to range resonance frequency from few hundreds of kHz to MHz. During the design process, we considered electrodes placed 300-500 nm apart from the resonating structure, to ensure contact. Pillar was coated with 100/20 nm of Al/Au and sticktion coefficient was calculated assuming $A_C = h_M \bullet w_T$, where h_M is the thick of total metal deposition and w_T is the width of pillar on its topside.

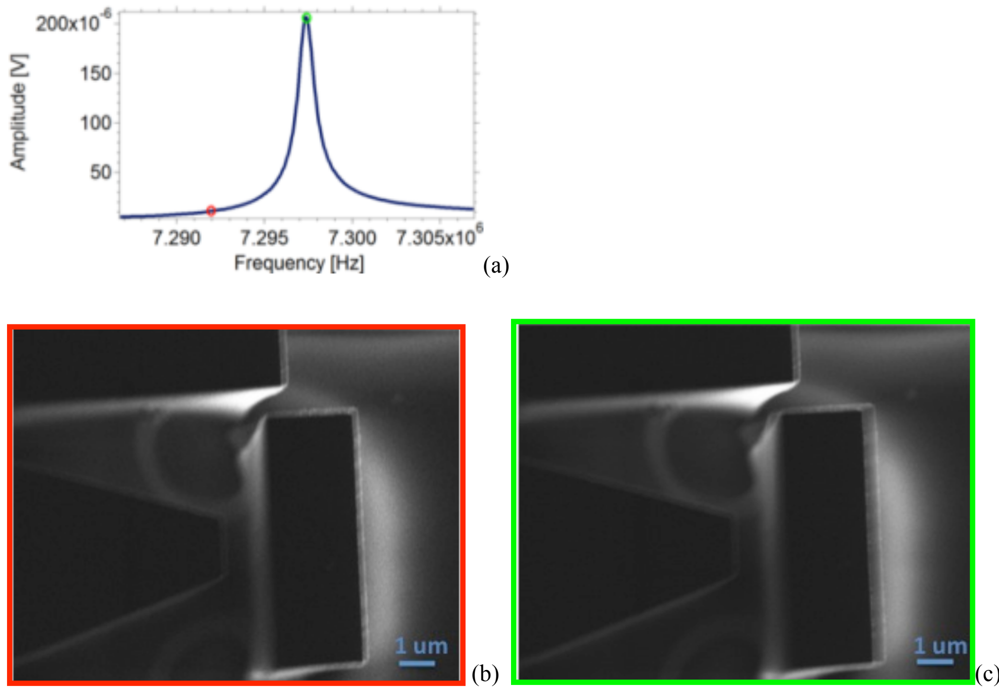

Fig. 4-10. Resonance amplitude vs. frequency **(a)**. The pillar oscillations were observed by SEM in two different conditions: **(b)** out of resonance and **(c)** in resonance.

Parameter	Value		
L [µm]	15	20	25
f_{FREE} [MHz]	2.03	1.03	0.594
F_{PINNED} [MHz]	15.9	8.02	4.63
λ_{300}	2.29	0.85	0.39
λ_{400}	4	1.5	0.69
λ_{500}	6.35	3.73	1.5

Tab. 4-1. Design dimensions of the device.

Two different designs were fabricated, both having the same initial fabrication process. The major difference is the number of electrodes. The masks and the schematics of electrical readout are presented in figure 4-11. The two different processes will be described in the following:

- Double electrodes configuration: The starting material is a silicon wafer with a 100 nm silicon nitride (Si_3N_4) layer deposited by low-pressure chemical vapor deposition (LPCVD) on both faces. We decided to develop our sensor based on Si_3N_4/silicon because silicon nitride is insulating and allows the localization

of current flow phenomena in metal electric contacts. Moreover this material is compatible with CMOS manufacturing process, making possible a future integration with control electronic system. SOI wafer are not suitable for this configuration since etching plasma does not penetrate homogeneously between close vertical structures. Therefore, as shown in figure 4-12 (a), residual silicon tales connect pillar with electrodes and disable device readout system. Sample was spin coated with S1813 resist (4000 rpm per 1 min) and baked for 1 min at 150 °C. Large area contacts and electrodes were printed by optical lithography on the resist. Metal deposition and lift-off defined the electrical tracks of the device. By a second spin coating of 500 nm of poly-methylmethacrate (PMMA) 950 K resist (2000 rpm per 1 min), a baking of 180 °C for 5 min, e-beam lithography (Zeiss Leo 30keV) and lift-off, pillar in-plane geometry and overall pattering were printed on the wafer. To define all the structures, we deposited an initial adhesive Cr layer with a thickness of approximately 5 nm on wafer substrate and then evaporated 5/40/40 nm Cr/Au/Ni multilayer. While gold was used to realize electrical contacts, thanks to its low oxidation at room temperature in air, nickel masked the structures during Bosch™ etching. Before etching, the specimen was annealed at 350 °C for 10 min in nitrogen flux [4-15], to create a stable Si/Cr/Au/Ni alloy. Finally, we performed a Bosch™ process to define the vertical pillar geometry with an inductively coupled plasma reactor (ICP, STS-Surface Technology). In this configuration, pillar was enclosed by two electrodes and acted like an RF switch that closes the electrical circuit. On one electrode DC voltage was applied while the second one was used in the readout system.

- Single electrode configuration: A second configuration was implemented starting from highly doped silicon wafer (0,001-0,005 Ω•cm). After thermal deposition of 170 nm silicon oxide (1h @ 1200°C), pillars and nearby electrodes were extruded using the same process implemented for previous configuration, with nickel as ICP mask. In order to electrically charge pillar structure through wafer bulk, we engraved a nano-ramp on the top of the microstructures by ion milling. FIB calibration and difference ramp geometries were tested in order to reduce material residuals and ensure electrical contact. In particular, we decided to perform ICP before FIB to reduce milling resides interferences on devices fabrication (figure 4-12 (b)). The ramps were 1x1 μm wide, 1 μm deep and presented an initial slope of 20 degree, as shown in figure 4-13 (b). To ensure electrical contact and metal continuity on the top of the pillar, 100/20 nm Al/Au was sputtered on the device. With this configuration, DC voltage was applied to chip bulk while the electrode was used for the readout.

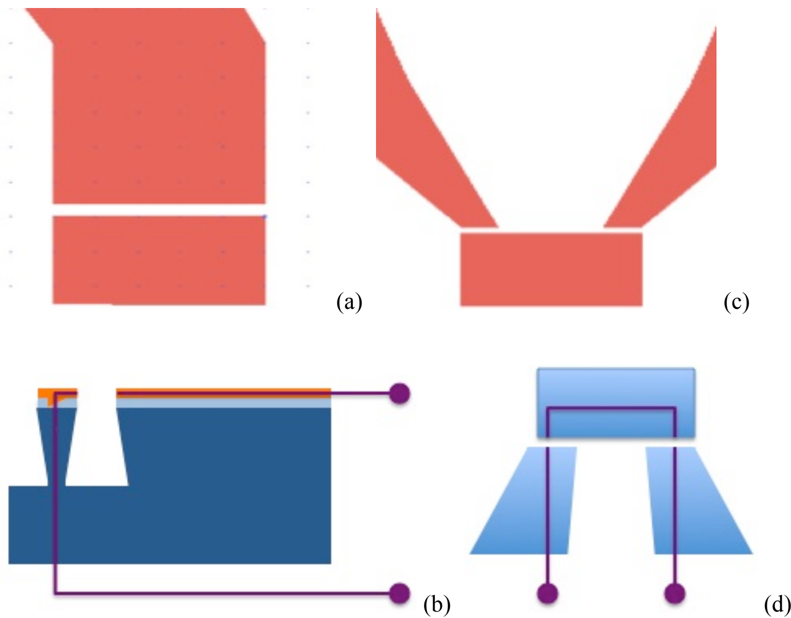

Fig. 4-11. Schematic draws of the two readout configurations implemented with **(a)** single and **(c)** double electrodes. Readout configurations are shown in **(b-d),** for single and double electrodes layout, respectively. Purple lines represent the electrical tracks. In particular, in single electrode configuration, metal layer (orange) contacts silicon bulk (dark blue) through an aperture realized by FIB on silicon oxide (sky blue).

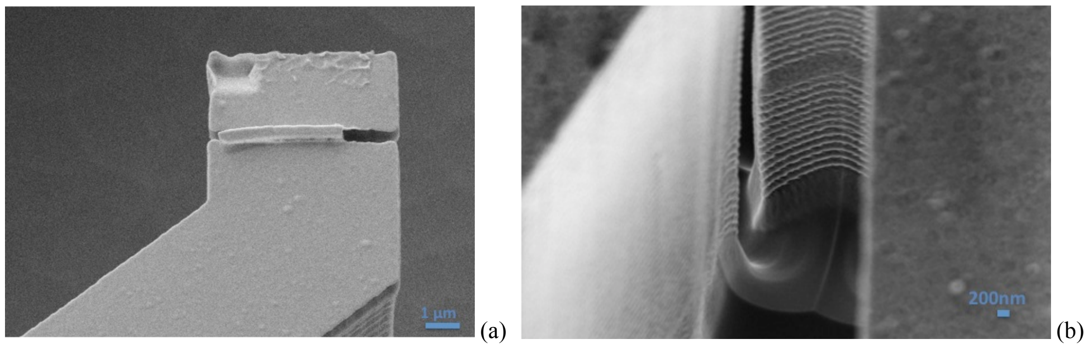

Fig. 4-12. Artefacts in **(a)** single and **(b)** double configurations. In the first case, when FIB was performed before ICP, residual dusts hindered PMMA lift-off process. In the second case, ICP plasma was not able to remove silicon tale that electrically connect close structures.

A dedicated dry etching process was developed to ensure a more efficient control on the process and on pillar height. Since we did not have silicon oxide as stopping layer, like in dielectric pillar, process has to be calibrate to settles the height and base dimensions of the pillar. For passivation, we used plasma of mixture of C_4F_8 and Ar (100 and 20 sccm) with 600 W of RF power applied to the coil while, for etching, we used plasma of mixture of

SF_6 and Ar (110 and 20 sccm) with 600 W of RF power applied to the coil and 50 W to the platen. Press and passivation time were gradually decrease and increase, respectively, during etching process, with a reduction on scallop dimensions on vertical walls. Typically, we remove almost 20 μm with 60 cycles and obtain pillar with base 600-900 μm thick.

After the fabrication process, the device was glued to a piezo-actuator (PZT). By using a silver paste to glue a DIL to the surface of the PZT, an out-of plane actuation of the cantilevers can be achieved. The electrical connections between the device pads and the package pins were realized with a bonding machine and gold wires. Final devices are shown in figure 4-13.

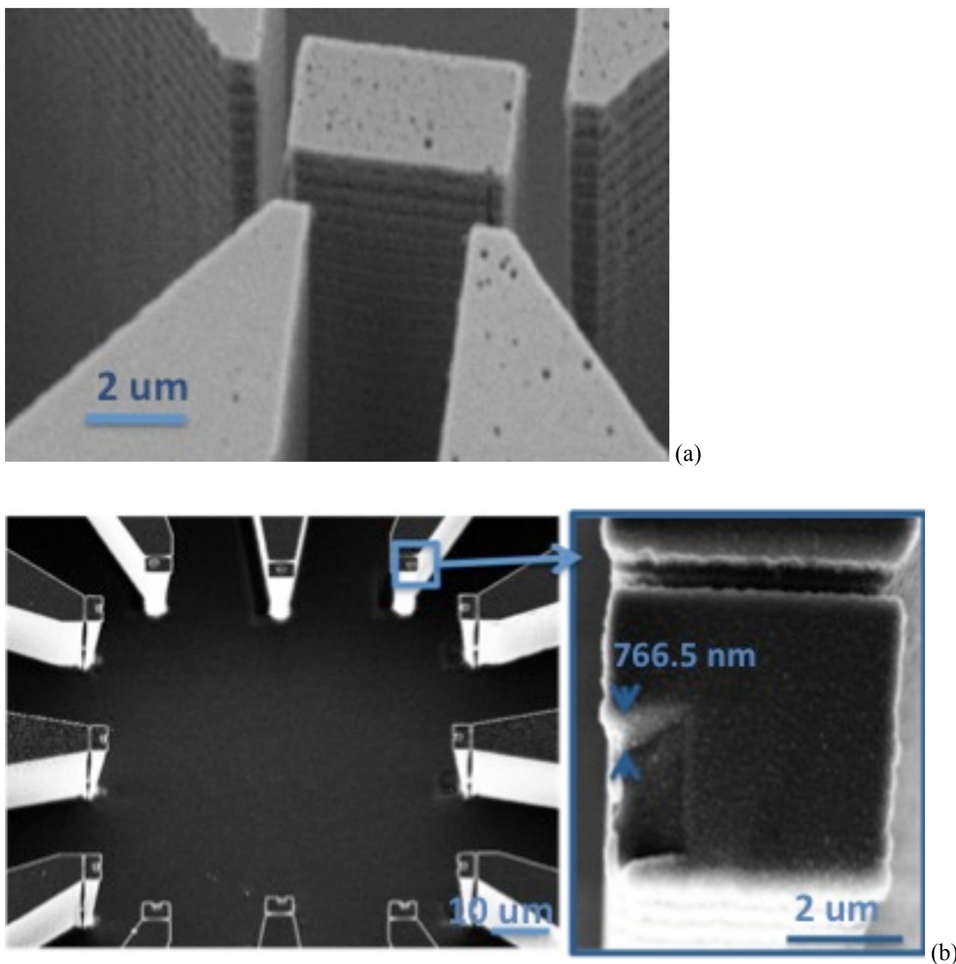

Fig. 4-13.Two SEM images of finished silicon pillars for both **(a)** single and **(b)** double configurations. In **(b)** micro-ramp performed on pillar top is zoomed. A ramp 766 nm deep will ensure the electrical connection between metal and silicon through silicon oxide.

4.2.3. Implemented measurement techniques

The setup used for characterization of the hard contact readout method consisted of two major parts: the actuation electronics and the readout circuit. Pillars were operated in dynamic mode, by applying an AC actuation voltage with maximum amplitude of 10 V_{PP} to the beneath piezo-actuator, and the entire readout and actuation system was integrated in a vacuum chamber through several flanges. A membrane pump was used to keep vacuum conditions around 0.5 mbar. The obvious drawback of this method is that not only the pillars are excited but also other several structures (holder, pillar chip, wires etc.), whose mechanical resonant modes can interfere with the desired signal. A rather precise estimate of the resonant frequency was therefore necessary, as a suitable reference during electrical measurements.

The preliminary readout of the cantilever frequency response was performed by a laser-optical system. In particular, pillars were tested with deflection mode to characterize their frequency response and to confirm hard contact phenomena. To align the optical readout to the cantilever chip an external CCD camera was installed. Electrical readout was then performed using two setups based on difference instrumentations: lock-in and transconductance amplifier. In all the experiments, the device was actuated by function generator (Agilent 33120A). One electrode of the device was connected to a power supply (IPS 405) while the other was used to acquire the current signal cause by the induced mechanical contact. We developed a program with LabVIEW software, which can interface with and set all electronic instrumentations, other than automatically perform a series of frequency scans. In each scans we considered different amplitude of the actuation signal (V_{AC}) and power supply signal (V_{DC}), while the data were collected and fitted. In the following sections the realization of the two parts will be presented:

- Lock-In Amplifier: lock-in amplifier (Stanford Research, SR830) [4-16] was set on low current measurements with a sensitivity of 100 pA and an input impedance of 1 MΩ. 1 V_{DC} was applied to sample bulk and the electrode nearby the pillar was directly connected to lock-in amplifier input through BNC cable.
- Transconductance amplifier: The integrating transconductance amplifier is based on a LMP7721 femtoamperometer input bias current precision amplifier [4-17], driven by ±5V. The LMP7721 features very fast slew rates, wide bandwidth, and low noise characteristics. Further details are reported on table 4-2. For the remaining components a capacitor of C = 1 pF and a resistor of R = 20 MΩ was chosen, facilitating a large integration constant and a slow discharge of the capacitor. C determines the amplification and the resistor R discharges the capacitor to obtain a steady-state signal. The DC-output of the integrating transconductance amplifier was measured with a computer-controlled multimeter (Agilent

35510A). The pillar was grounded, the electrode close to the resonator was connected to the inverting-input of the integrating amplifier and a DC voltage, V_E, was applied to the non-inverting input. When contact occurred once every cycle, a unidirectional current pulse train, $I_{IN}(t)$ was supplied to the amplifier. Input signal presented a pulse width of t_C, and a magnitude of V_E/R_C, where R_C is the total resistance of the contact. Amplifier integrate the unidirectional current train and at steady state it output voltage reaches a value of:

$$V_O = V_E - RI_{IN} = V_E - \frac{Rt_C}{R_C T} V_E \quad (4\text{-}7)$$

where I_{IN} is the time average of the input current, R the transconductance resistance (20 MΩ), t_C the contact time and T the cycle time.

LMP7721 characteristics	Value
Input bias current	±20 fA
Voltage noise	6.5 nV/√Hz
DC offset voltage	±150 µV
DC open loop gain	120 dB
DC CMRR	100 dB
GBW	17 MHz

Tab. 4-2. Main features of LMP7721 amplifier at 25 °C.

4.2.4. Initial characterization

To test the hard contact readout method, the frequency response of each pillar was initially recorded optically. The oscillations were excited by piezo-actuation and were detected using a green laser and a four quadrants photodiode in optical lever configuration. We applied the same setup used in chapter 4.2.1. to compare light intensity measurements with optical deflection one on pillar array. A network analyzer (3577A Hewlett–Packard) generated the sweeping actuation signal, acquired and filtered the signal coming from the photodiode, extracted the actuation frequency and provided the amplitude and the phase elements. The instrument was set to collect 401 points with a frequency span is 10 kHz and a duration of the sweep of 60 sec. With low actuation

voltage, from a Lorentzian fit of the amplitude curve, the resonant frequency is found to be in the range of 1-4 MHz with a *Q-factor* around 13 10^3.

As presented in figure 4-14 (a), during positive frequency scans, with higher actuation voltage the frequency response of the device shows a flat amplitude region due to the fact that pillar oscillation amplitude is limited by the adjacent structure. Moreover, during contact time t_C, system behaves chaotically and pillar motion is described by a superposition of mode (sub-harmonic frequencies are introduced).

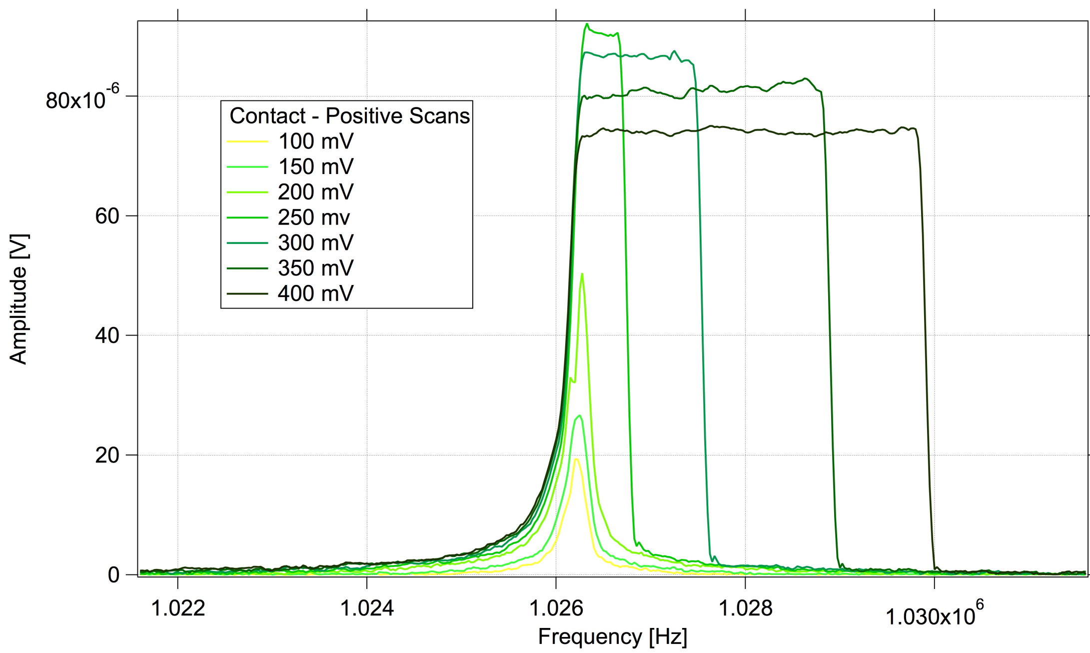

(a)

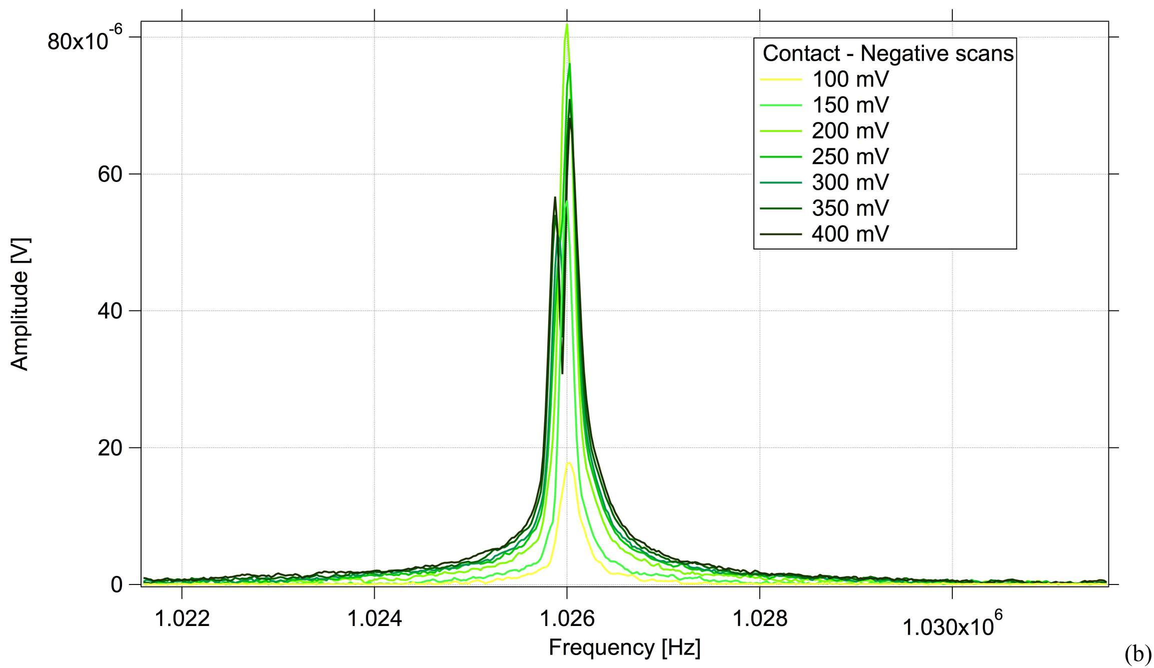

(b)

Fig. 4-14. Amplitude at different actuation voltages for positive **(a)** and negative **(b)** frequency scans.

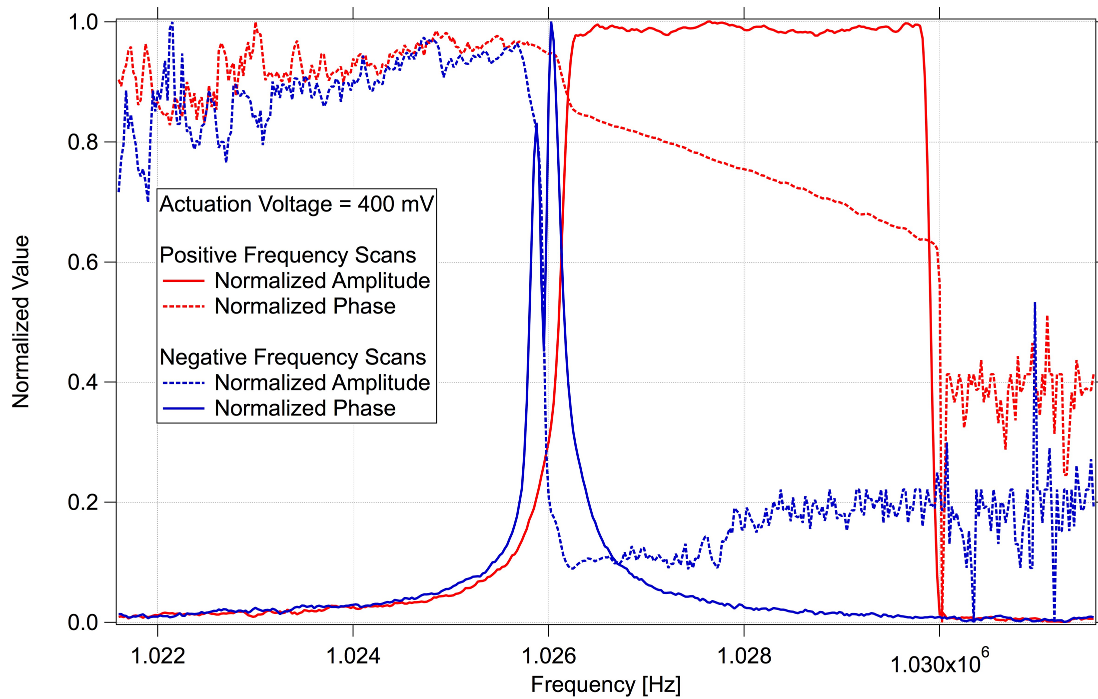

Fig. 4-15. Comparison between amplitude (line) and phase (dots) response of pillar when contact occurs: positive (red) and negative (blue) frequency scans.

The mechanical contact causes a shift of resonance frequency to higher values [4-18] and, with the increase of

the actuation voltage, the plateau increases its frequency extension. When contact ends, frequency response comes back to its original value and the response of device drastically drops down. That confirms the possibility to control contact time t_C and the amount of current that flows into readout system by modulating the amplitude of actuation voltage. As shown in figure 4-15, when we consider positive frequency scans, phase shows a linear behaviour during contact. The same behaviour cannot be found in negative scans, either in the amplitude or in phase response.

Scans with negative frequency shows a two-peak response in the amplitude response (figure 4-14 (b)). When contact occurs, pillar amplitude response drops down immediately, due to the shift of the resonance frequency. This causes a decrease on oscillation amplitude down to no-contact condition. As a consequence, pillar immediately arises out of chaotic state and this results in a narrow amplitude negative peak at f_0. At the same time, phase response shows a step-like change in correspondence of f_0 and the difference behaviour of phase in positive and negative scans have to be taken into account when contact pillar readout is interfacing with phase-locked loop (PLL) system. As already mention on chapter 1.2.3., PLL keeps actuation and detection signal phase at -90 degree and can be use to follow MEMS resonance frequency shift over time. Further information about this system will be offer in chapter 6. In particular, PLL response could be more sensible to negative shifts of frequency response, which occur when the analyte is adsorbed by the pillar.

4.2.4.1. Impact oscillator

The observed response has been investigated over the last decades in dynamical systems literature [4-19 – 4-21] and its model is depicted in figure 4-16. It is composed by a periodically forced and damped linear one-dimensional oscillator whose displacement is limited by an amplitude constraint, $x = x_C$, which is a rigid wall on which the oscillator collides inelastically. Setting the oscillator mass to 1, the oscillator behaviour can be described with the equation [4-22]:

$$\ddot{x} + c\dot{x} + k|x| + x = F\cos(\omega t) \tag{4-8}$$

where c is the damping coefficient, k the elastic coefficient and F the forcing amplitude. An impact occurs whenever $x = x_C$ and the collisions are modelled by the law of inelastic impact (Newton impact law). After each impact, the velocity is taken to be R times the velocity before the impact, where R is a constant restitution coefficient ($0 < R < 1$).

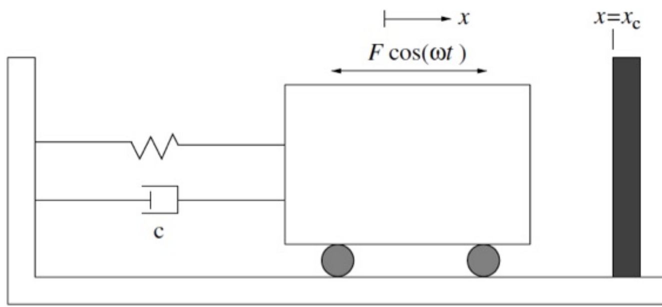

Fig. 4-16. Model of an impact oscillator.

4.2.5. Preliminary results

As already mention, preliminary sample behaviour was tested with deflection mode technique, in order to find the resonance frequency and the minimum actuation voltage to install mechanical contact between pillar and electrode. A frequency range of 10 kHz was conventionally used as frequency scans window to perform both optical and electrical measurements.

By looking at samples status after preliminary characterization, metallic layer of configuration 1 exhibited damages at one electrode, due to localization of contact phenomena. Indeed this implies that hard contact occurred only at one of the two electrodes. It follows that the circuit was not properly closed and not current was able to flow during the contact time. The reason of this result may be linked to unavoidable imprecision of the nanofabrication techniques used in this research project: if one of the two electrodes exceeds only of a few nanometers the other, the electrical circuit will not be closed.

A preliminary measurement was performed on a pillar in single-electrode configuration by applying 15 V_{DC} to its bulk and measuring the DC voltage by a multimeter (figure 4-17) and electrical results perfectly fit with optical one, under the same actuation conditions. In order to obtain amplitude peak of 5 mV, an high DC voltage was applied to the devise, which damaged the deposited electrical contacts, that is to say we experienced the partial removal and the burning of gold layer. For this reason, this measurement technique was abandoned.

Both lock-in and transconductance amplifiers were unable to detect pillar resonance response. High resonance frequency and sticktion parameter close to 1 can both be responsible for this result. By reducing pillar base to a thickness less than 300 nm and increasing the high at 20 μm, operating resonance frequency of around hundreds of kHz can be reach. This expedient would make possible the detection of higher resonance mode for clamped pillar during contact. However, to respect design limits and keep sticktion parameter above 1, distance between

pillar and electrode must increase, which leads to an increase of actuation voltage.

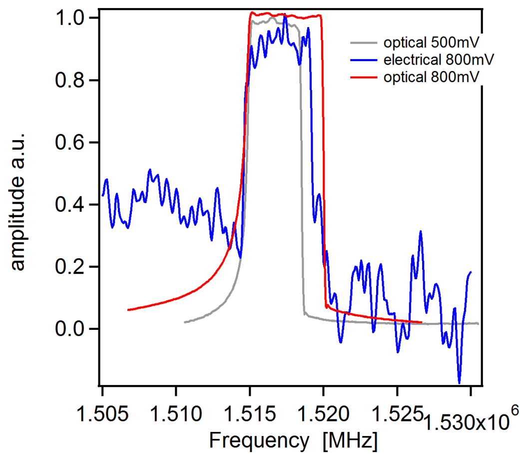

Fig. 4-17. Preliminary measurements performed on a hard contact pillar.

4.3. SUMMARY AND DISCUSSIONS

In summary, we designed and implemented a strategy for the integration of μ-pillar sensors, by taking advantage of the Kelvin force for the actuation and of the hard contact for the readout. In the first part of the chapter the behaviour of a pillar as a resonance structure were studied. The theoretical evidence of the dependence of the polarization and position of the pillar related to the actuation electrode was investigated and, to validate the theoretical results, finite element (F.E.) simulations were performed. In the second part, the principle behind the hard contact method was been taken into account and impact oscillator frequency behaviour was studied in order to determine the current flowing through the device.

The obtained results represent the first steps toward a full integration of pillars with on-chip electronic. Changes on pillar design are scheduled for hard contact readout configuration. The aim is to decrease operating frequency and to increase contact area. Exclusively transconductance amplifier setup is going to be used for further measurements since it allows feeding pillar with high voltages without any damage to the connected electronic instrumentations.

In order to apply our device to actual biological applications, and thus in liquid environment, several fabrication steps are missing. First both the geometries should be modified and a chemical functionalization step should be introduced to obtain a superhydrophobic system. In particular, from the actuation point of view, the field

generated in the gap between pillar and electrodes can be as high as 2.2 10^5 V/cm, close to the distilled water breakdown, and definitely too high to operate in physiological conditions, with saline buffers, ionic conduction and ionic screening. To circumvent these problems, the liquid should be in contact with an insulating layer. A further process step consisting in the deposition of a Si_3N_4 layer on top of the electrodes should be implemented.

REFERENCES

[4-1] Q.P. Unterreithmeier, E.M. Weig and J.P. Kotthaus. "Universal transduction scheme for nanomechanical systems based on dielectric forces". Nature, vol.458, pp. 1001–1004, 2009.

[4-2] S. Schmid, C. Hierold and A. Boisen. "Modeling the Kelvin polarization force actuation of micro- and nanomechanical systems". Journal of Applied Physics, vol. 107, 054510, 2010.

[4-3] S. Schmid, M. Wendlandt, D. Junker and C. Hierold. "Nonconductive polymer microresonators actuated by the Kelvin polarization force". Applied Physics Letters, vol. 89, 163506, 2006.

[4-4] J. N. Israelachvili. "Intermolecular and surface forces". Academic Press, New York, pp.480, 1991.

[4-5] S. Schmid, P. Senn and C. Hierold. "Electrostatically actuated nonconductive polymer microresonators in gaseous and aqueous environment". Sensors and Actuators A: Physical, vol. 144-146, pp. 442–448, 2008.

[4-6] Z. Hao and Y. Xu. "Vibration displacement on substrate due to time-harmonic stress sources from a micromechanical resonator". Journal of Sound and Vibration, vol. 322, pp. 196–215, 2009.

[4-7] Y. Zhang. "Determining the adsorption-induced surface stress and mass by measuring the shifts of resonant frequencies". Sensors and Actuators A: Physical, vol. 194, pp. 169–175, 2013.

[4-8] S. Dohn, O. Hansen and A. Boisen. "Cantilever based mass sensor with hard contact readout". Applied Physics Letters, vol. 88, 264104, 2006.

[4-9] S. Dohn, O. Hansen and A. Boisen. "Measurement of the resonant frequency of nano-scale cantilevers by hard contact readout". Microelectronic Engineering, vol. 85, pp. 1390–1394, 2008.

[4-10]Y. Lin, W.C. Li, Z. Ren and C.T.C. Nguyen. "A metal micro mechanical resonant switch for on-chip power applications". Proceeding of the Electron Devices Meeting (IEDM), 2011 IEEE International, pp. 20.6.1 - 20.6.4, 2011.

[4-11] Y. Lin, W.C. Li, Z. Ren and C.T.C. Nguyen. "A resonance dynamical approach to faster, more reliable micromechanical switches. Proceeding of the Frequency Control Symposium, 2008 IEEE International, pp. 640 - 645, 2008.

[4-12] J. R. Vig and Y. Kim. "Noise in microelectromechanical system resonators". IEEE Transactions on Ultrasonics, Ferroelectrics, and Frequency Control, vol. 46, issue 6, pp. 1558–1565,1999.

[4-13] A. Erbe, R.H. Blick, A. Tilke, A. Kriele and J.P. Kotthaus. "A mechanically flexible tunneling contact operating at radio frequencies". Applied Physics Letters, vol. 73, issue 25, pp. 3751 - 3753, 1998.

[4-14] J. Shah."Estimating bond wire current-carrying capacitity". Available form: www. powersystemdesign.com, 2014.

[4-15] D. Miller, C. Herrmann, H. Maier, S. George, C. Stoldt and K. Gall. "Intrinsic stress development and microstructure evolution of Au/Cr/Si multilayer thin films subject to annealing". Scripta Materialia, vol. 52, issue 9, pp. 873–879, 2005.

[4-16] Standford Research System, SR830, 2011.

[4-17] Texas Instruments, LMP7721, 2013.

[4-18] S.W. Shaw and P.J. Holmes. "A periodic forced piecewise linear oscillator". Journal of Sound and Vibration, vol. 90, issue 1, pp. 129-155, 1983.

[4-19] Y. Ma, J. Ing, S. Banerjee,M. Wiercigroch and E. Pavlovskaia. "The nature of the normal form map for soft impacting systems". International Journal of Non-Linear Mechanics, vol. 43, issue 6, pp. 504–513, 2008.

[4-20] A.V. Dyskin, E. Pasternak and E. Pelinovsky. "Periodic motions and resonances of impact oscillators". Journal of Sound and Vibration, vol. 331, issue 12, 2856–2873, 2012.

[4-21] F. Peterka. "Behaviour of impact oscillator with soft and preloaded stop". Chaos, Solitons and Fractals, vol. 18, issue 1, pp. 79–88, 2003.

[4-22] S.L.T. De Souza, I.L. Caldas and R.L. Viana. "Damping control law for a chaotic impact oscillator". Chaos, Solitons and Fractals, vol. 32, issue 2, pp. 745–750, 2007.

5. REAL-TIME MEASUREMENTS

In order to follow MEMS resonance frequency evolution over time, a phase-locked loop (PLL) was realized using National Instrument technologies and programming a field programmable gate array (FPGA) by a dedicated LabVIEW module. Indeed, phase presents a monotonic and sharper behaviour than amplitude nearby resonance frequency. By defining the phase value we want the pillar to work at, we can lock pillar-vibrating operation by adjusting actuation frequency every time changes in the environment or in pillar mechanical properties cause a shift of its resonance frequency.

The theory of continuous-time and discrete-time, i.e. digital, phase-locked loop is extensively discussed by Farhang-Boroujeny in [5-1]. In this chapter we will summarize the theory of digital PLL (DPLL), address important issues for Field Programmable Gate Array (FPGA) implementation and present the second order DPLL we built and interfaced with MEMS resonators.

5.1. PLL THEORY AND ARCHITECTURE

PLL can be analyzed in general as a negative feedback system. The generic block diagram for DPLL is shown in figure 5-1, where $x[n]=sin(2\pi f_C nT_S+\theta_C[n])$ is the input signal, $y[n]=sin(2\pi f_0 nT_S+\theta_0[n])$ the output signal, $\varepsilon[n]=k_D \bullet (\theta_C[n]-\theta_0[n])$ the phase detector output and k_D the phase detector gain. PLL is a linear feedback control system that generates an output signal, which has the same frequency and phase as the input reference signal. Phase-locked loops can be used, for example, to generate stable output frequency signals from a fixed low frequency signal. Their main components are a phase detector (PD), a digital loop filter (DLP) and a voltage control oscillator (VCO). Since VCO transfer function is given by:

$$H_{VCO}(z)=\frac{\Theta_0(z)}{C(z)}=\frac{k_0 T_S}{z-1} \tag{5-1}$$

the phase transfer function of a PLL can be written as:

$$H(z) = \frac{\Theta_0(z)}{\Theta_C(z)} = \frac{L(z)H_{VCO}(z)}{1-L(z)H_{VCO}(z)} = \frac{L(z)k_O k_D T_S}{L(z)k_O k_D T_S + z - 1} \tag{5-2}$$

where k_0 is the gain of VCO and T_S is duration between two consecutive data samples. At steady-state, frequency is locked, $f_C = f_0$, and the phase error in this condition must be determined when PLL input change in phase ($\theta_C[n]=u[n]$) and in frequency ($\theta_C[n]=2\pi\Delta f_C n u[n]$) for different filter designs ($L(z)$). We considered first-order and second-order PLL, where the loop filter is essentially a constant gain, k_L, or a first-order filter respectively. By using the final-value theorem on z-transform, steady-state phase error is:

$$\varepsilon_{SS} = \lim_{z\to 1}(z-1)E(z) = \lim_{z\to 1}(z-1)\left(\Theta_C(z) - H(z)\Theta_C(z)\right) \tag{5-3}$$

For first-order PLL, when a step change in the input frequency occurs, ε_{SS} converges to a constant. On the other hand, it can be shown that the steady-state phase error proportional-integral (PI) loop PLL is zero for both frequency and phase step input. For this reason, in our project a PI filter were implemented. Its transfer function:

$$L(z) = k_L \frac{1+\alpha z^{-1}}{1-z^{-1}} \tag{5-4}$$

was developed to design a stable DPLL, by acting on filter parameters k_L and α. In particular, the condition to be met in order to locate the pole of $H(z)$ inside the unit circle in z-plane was:

$$\left| \frac{-K_L T_S + 2 \pm \left(K_L^2 T_S^2 - 4K_L T_S(1+\alpha)\right)^{1/2}}{2} \right| < 1 \tag{5-5}$$

where $K_L = k_L k_0 k_D$ is the cumulative gain.

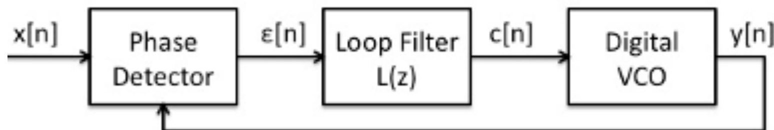

Fig. 5-1. Generic block diagram for a digital PLL

5.1.1. Phase detector

A digital signal *x[n]* can be represented by an in-phase *I[n]* and a quadrature *Q[n]* component. Given I and Q components of the input signal, the phase of the signal can be computed as:

$$\varepsilon[n] = artcan\left(\frac{Q[n]}{I[n]}\right) \tag{5-6}$$

An arctan function is difficult to implement on FPGA due to the limited resources and computation limits of the hardware. A practical implementations of phase detectors on FPGA is the *Modifed Costas phase detector*, in which phase error is expressed as $\varepsilon[n]=sign(I[n])Q[n]$. Its biggest problem is that its gain, k_D, depends on the input phase error and can be assumed roughly linear only when the input phase error is small. This leads to some errors in system characterization. However, since the *Modifed Costas phase detector* is a very computationally efficient algorithm, it is widely used in FPGA applications.

Another algorithm implemented on FPGA to perform phase detection is CORDIC, which is based on an iterative method to compute arctan, using only shift, add, and sign functions [5-2]. To determine θ by performing arctangent operation, when the coordinates *[x,y]* of the corresponding point on the unit circle in the Cartesian plane are given, the algorithm rotates the coordinates repeatedly. By making the y component tends to 0, phase can be determinate after a certain number of iterations. It can be implemented to perform other hyperbolic and trigonometric functions and was employed in our program to compute arctan function within a time loop, with a latency of 17 clock cycles. The biggest limitation of this algorithm is that upper and lower bounds for the output phase exist. Indeed, its output reaches a plateau after the input phase exceeds a certain value, which can be determinate mathematically and is equal to ±0.9579 radiant. By increasing the number of iteration cycles quantization error inside this region can be reduce and phase detector become more linear within this operating region.

5.1.2. DDS theory

As stated in [5-3], *Direct Digital Systhesis* (DDS) is a technique for using digital data processing blocks as a means to generate a frequency- and phase-tunable output signal referenced to a fixed-frequency clock source. Figure 5-2 (a) shows a generic block diagram of DDS, which is constituted by:

- A reference clock.

- A phase accumulator which is actually a modulus counter
- A PROM (programmable read-only memory).
- A digital to analog converter D/A.

It is helpful to visualize the signal generator as a vector rotating around a phase wheel, as shown in figure 5-3(b), where the output of the phase register points to a position of the phase wheel and a revolution around the wheel corresponds to a cycle of the periodic wave. The output data from the DDS, corresponding to the amplitude of a complete sinusoidal signal, are contained in the PROM, which therefore acts as a look-up table. The counter-address points at specific location on PROM and increases (M-bit) its value of a quantity specified by N-bit word at every clock. Its output is therefore linear and the look-up table converts it into the amplitude of a sinusoidal signal. Finally, the data stored in the memory has to be converted into analog signal by a DAC and the output is an analog signal whose frequency depends on:

- The frequency of the reference clock (f_{clock}).
- The step used to sample the reference sinusoid, which is store in the PROM.
- The resolution of the digital word input to the DDS, the so-called frequency tune word (FTW).

The frequency tuning resolution of the DDS is obtained as:

$$\delta f = \frac{f_{clock}}{2^M} \tag{5-7}$$

At the same time, the output frequency, f_0, of the DDS is a function of the frequency clock (f_{clock}), the value of the N-bit word (FTW) and the size of the phase accumulator register. Their relationship is:

$$f_0 = FTW \frac{f_{clock}}{2^M} \tag{5-8}$$

where FTW value can be updated in real-time. In order to fit DDS into our PLL model, we need to characterize it in discrete-time domain. The relation between two consecutive output phase samples can be expressed as:

$$\vartheta[n+1] = \vartheta[n] + 2\pi\Delta f[n]T_S \tag{5-9}$$

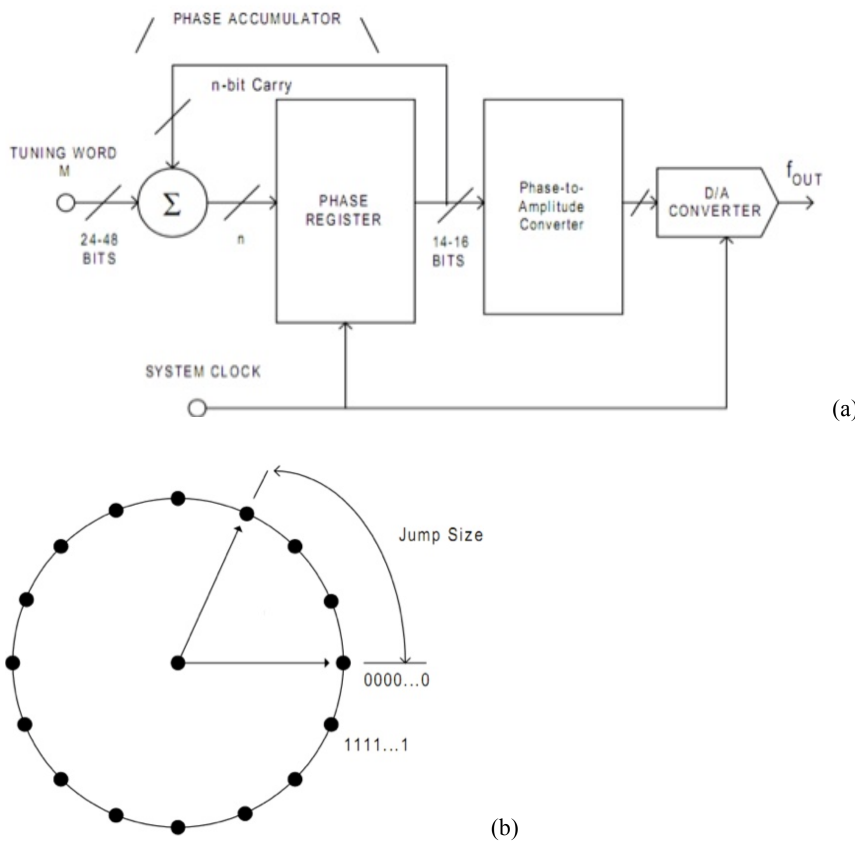

Figure 5-2. (a) Generic block diagram of a frequency-tunable DDS system and **(b)** sinewave oscillation representation as a vector rotating around a digital phase circle [5-3]

where *Δf[n]* is DDS offset from free-running frequency at time *n*. By comparing equation 5-1 and 5-7, it follows that $c[n]k_0=2\pi\Delta f[n]$. In our project, DDS is clocked with a 100 MHz source while a 31-bit word is used for both phase accumulator and FTW. Therefore, DDS features precise frequency control with a step size of 0.023 Hz.

Moreover, compared to analog synthesizer solutions, DDS is more robust against component aging and temperature drift and the amount of output frequency jitter largely depends on the quality of the reference clock. Indeed, DDS transfer function shown a gain of 0.15, which is equal to a minimum increase in its output angular frequency of 0.15 rad/s, when $c[n]=1$.

5.2. IMPLEMENTATION AND ANALYSIS

In this chapter we will cover the hardware components that are related to our project and give an overview on how they communicate with each other.

5.2.1. NI 5781R hardware

NI 5781R comprises of a NI FlexRIO FPGA module and an NI5781 FlexRIO adapter module that can be programmed with LabVIEW graphical programming language, with some constraints (e.g. it is not possible to work with multidimensional arrays). More information on NI 5781R can be found in [5-4]. As shown in figure 5-3, it has two differential analog inputs (AI), two differential analog outputs (AO), and seven digital I/O (DIO) lines. In our project, one AI channel is used to receive the incoming signal, which is sampled at 100 MHz at the front end of ADC and then converted to baseband IQ data by a digital-down converter (DDC). IQ data can be processed directly on FPGA using inline processing or streamed to host using Direct Memory Access (DMA) via PCI interface. 40 MHz base clock can be used to control the timing of the processes running on FPGA. By default, the functions on the FPGA operating in timed loops where no-clock is explicitly are compiled to FPGA clock so that their execution time stays constant when other clocks are customized to run at various frequencies. The analog input module NI5781 is an A/D converter with a resolution of 14 bit. The measuring range is $1V_{PP}$ for single-ended input and 2 V_{PP} for double-ended one while sampling rate can be set up to 100 MS/s. It follows that the smallest measurable single-ended voltage is 0.06 mV_{PP}.

FlexRIO NI 5781 can be programmed by LabVIEW FPGA module, thanks to a feature for HDL IP integration called CLIP. NI FlexRIO devices support two types of CLIP:

- User-defined CLIP, which allows users to insert HDL IP into an FPGA target.
- Socketed CLIP, which allows our IP to communicate directly with both the FPGA VI and the external adapter module connector interface. The NI-developed NI5781 CLIP provides access to four analog channels, eight PFI lines, one clock output, and an input clock selector. This CLIP also contains an engine to program the ADC, DAC, and clock, through predetermined settings for an easier instrument setup.

Communication between computer and NI5781R is governed by PXI protocol, which integrate PCI bus with triggering and temporization (10 MHz) ones. The control of PXI by PC is allowed thanks to a PCI/PCI Express board inside the computer and a PXI/PXI Express module inserted in slot 1 of PXI system. Other properties of NI5781 and its convertor specifications [5-5 – 5-6] are listed in table 5-1.

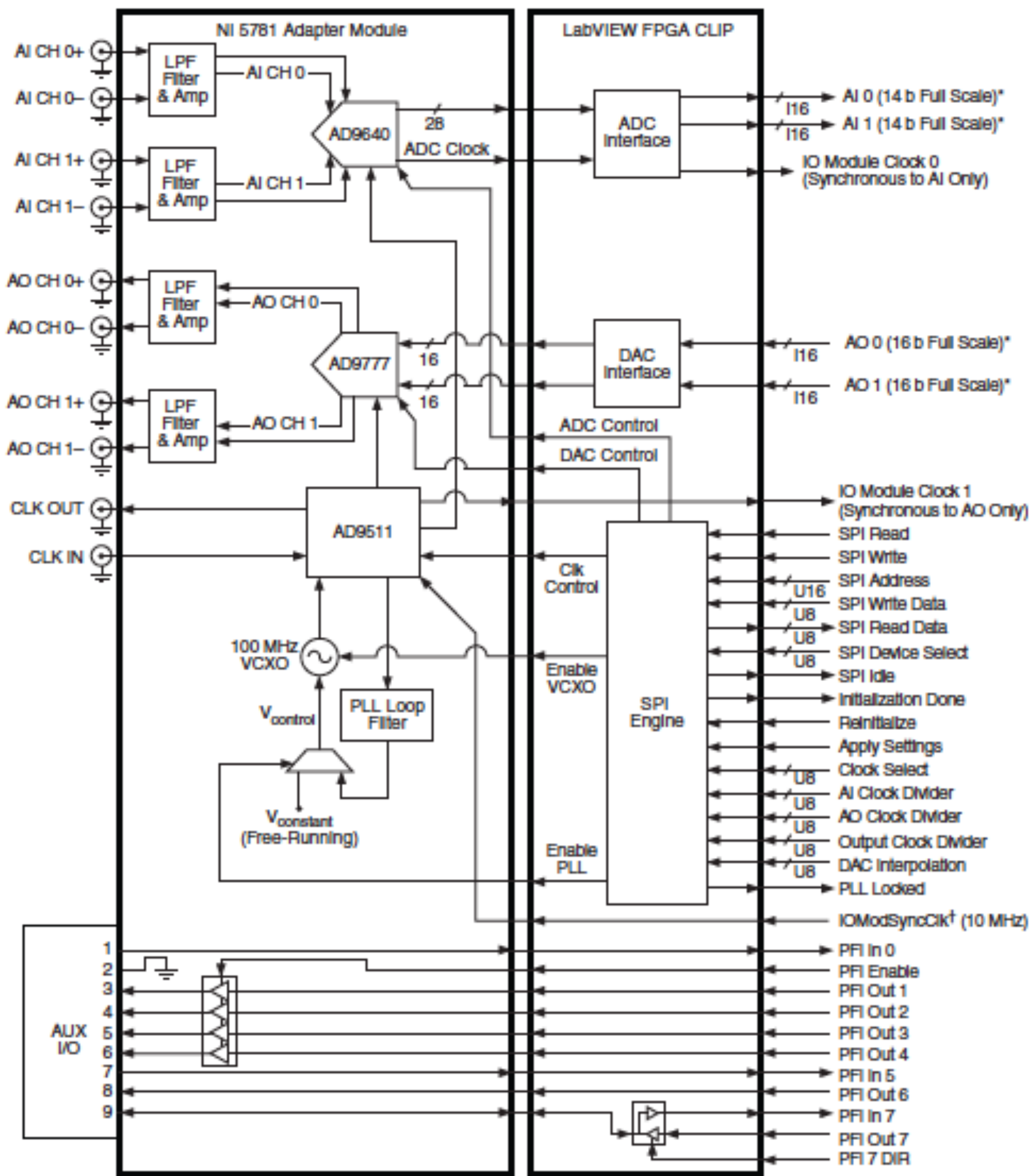

Fig. 5-3. NI5781 signal flow to and from the NI5781 component-level intellectual property (CLIP) by way of the adapter module and the corresponding NI5781 CLIP in LabVIEW FPGA.

Analog Input and Output – General Characteristics	
Connector	MCX
Input range	
Differential	2 V_{PP}
Common mode range	±1 V_{DC}
Single-ended	1 V_{PP}
Output range	
Differential	2 V_{PP} (into 1000 Ω) - 4 V_{PP} (into high Z)
Single-ended	1 V_{PP} (into 50 Ω) - 2 V_{PP} (into high Z) -
Internal sample clock	10 MHz to 100 MHz (100 MHz by default)
Input/Output impedance	50 Ω
Output coupling	DC
ADC part number	AD9640/105; 13-bit resolution, dual ADC, multistage, differential pipelined architecture
DAC part number	AD9777; 15-bit resolution, dual DAC, selectable interpolation rate
Filter type	Fixed 7th-order elliptical
Bandwidth	40 MHz

Tab. 5-1. Main features of FlexRIO NI5781

5.2.1.1. Programming strategy

We chose to collect and processes MEMS resonance data by NI5871R hardware to reproduce real-time system since, to perform IQ algorithm, data has not only to be logically correct but also time correct [5-7]. Indeed, there are no other technical systems where hardware and software are so closely coupled as in embedded systems. In particular, DPPL required:

- Timeliness: input data has to be collected in time.
- Synchronism: events linked to input phase computation have to be processed at the same time. In LabVIEW this is presented with two timed loops that are beside each other (to collect the sensor data in one loop and sending the actuator commands in the other loop) and synchronized with the same clock. This will guarantees timeliness and simultaneous execution of both tasks.
- Availability: real-time system must be constantly ready for operation, so that spontaneous reaction to events is possible without violating the timing restrictions.

Moreover DPLL must handle two types of event, which required real-time programming supported by NI5871:

- Synchronous Programming: Phase identification is a cyclic task that has to be periodically executed.
- Asynchronous Programming: It is used for handling aperiodic events, like the request to read the incoming data performed by PC operator.

Data to be transfer between FPGA and host were stored in host-to-target DMA FIFO or target-to-host DMA FIFO, depending on the transportation direction. Control of synchronous events was implemented on FPGA within 5 main parallel time loops:

- I/O loop: as shown in figure 5-4, data were acquired from analog input ports while actuation signal were written into the output port. DDS was realized by filling a lock-up table of 1024 elements with a half period of a sinusoidal signal. The frequency of DDS signal was determined by *FREQ_act* variable while phase behaviour was controlled by *PH_act* variable. In order to estimate IQ parameters, shift registers collected two consecutive I/O signals.
- First filter loop: AI signal was filter to reduce the influence of noise on phase calculation. It consisted on a Butterworth filter of 16th order working at 100 MHz and coefficients were determined by Matlab.
- PD loop: The extraction of IQ component from AI signal was performed at 40 MHz. In other words, most of the data were discarded due to the relatively slow execution rate of PD loop and the influence of input noise and quantization error were reduced [5-7].
- Processing loop: IQ data were collected at 40 MHz and phase error value was computed and stored in a local variable to be compute to the control signal. Simple manipulation of phase data, such as scaling, can be done in this loop sample-by-sample before they are sent to the memory.
- Second filter loop: Two types of loop lowpass filters are implemented in this loop. The first one performed the mean over the last 16 phase values while the second one was a PI filter. All of them were implemented with fixed-point arithmetic.

Interface with PC was governed by finite-state-machine (FSM – figure 5-5). Every change in command variable (*Cmd*) was transfer into a sequence of actions, which enabled NI5871R to read-write the data, perform a frequency scans, act as a PLL. Each state of the FSM took 1 μsec.

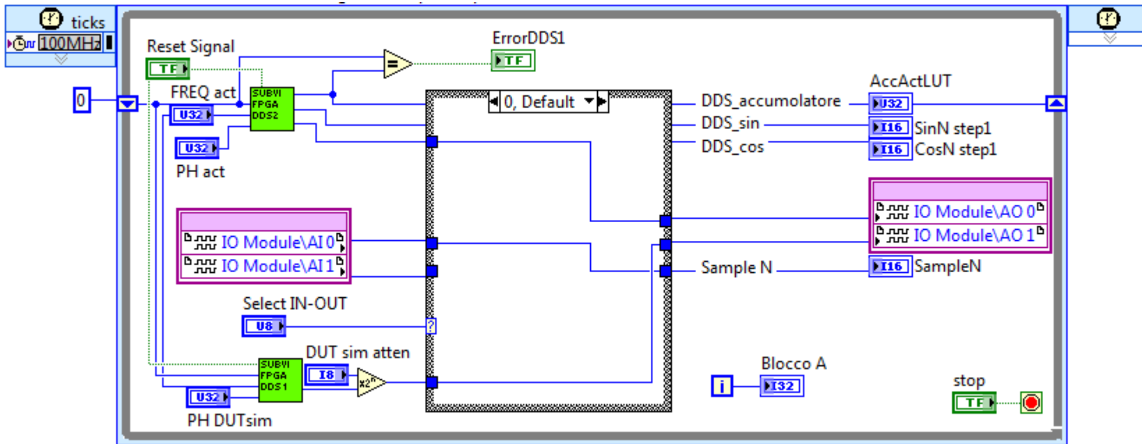

Fig. 5-4. LabVIEW time loop, which is in charge of handling input and output signal.

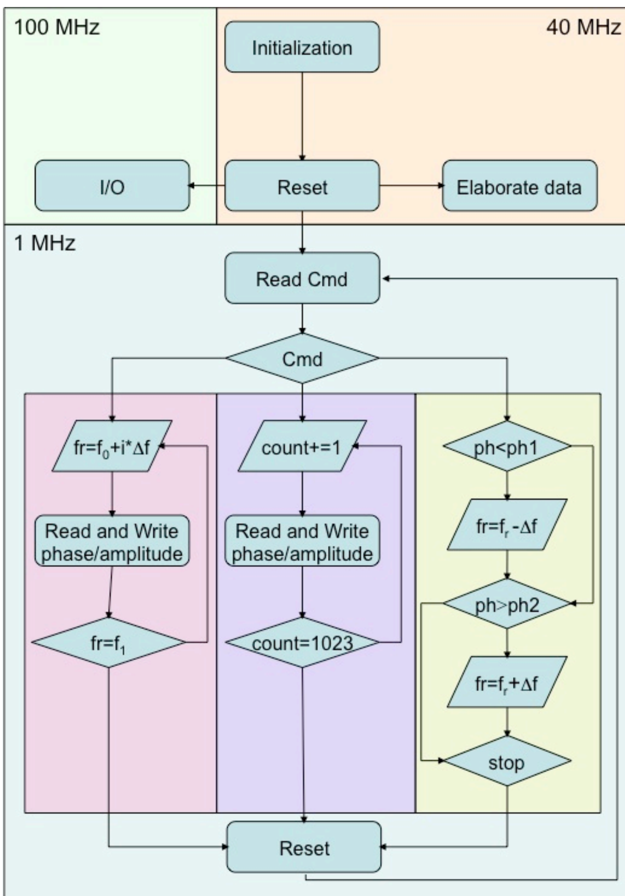

Fig. 5-5. Schematic of PC-FlexRIO interface logic.

5.2.2. Other hardware

In order to measure resonance MEMS movements operating in dynamic mode, samples were placed inside a vacuum chamber and actuated by piezo-crystal while detection was based on deflection mode. In this operating conditions the amplitude of the sinusoidal signal detected by four-quadrants photodetector (QPD), though it is a function of laser focalization, typical ranges between $10^{-4} – 10^{-6}$ V_{PP}. Since input voltage sensitivity for NI5871R is 2^{-13} V_{PP}, MEMS signal was amplified using an HVA-10M-60-B low noise amplifier [5-8]. The main characteristics of HVA-10M-60-B are listed in table 5-2. During experiments, by default, the amplitude was set at 60 dB and the device was DC-coupled to National instrumentation.

HVA-10M-60-B	
Input impedance	50 Ω || 12 pF
Input Voltage Noise	0.9 nV/√Hz (@ 2 MHz, 60 dB gain) 1.8 nV/√Hz (@ 2 MHz, 40 dB gain)
Input Bias Current	18 µA
Input Offset Voltage	500 µV typ.
Output Impedance	50 Ω (terminate with 50 Ω load for best performance)
Output Voltage	± 3.5 V (@ 50 Ω load, for linear amplification)
Slew Rate	500 V/µs (@ 50 Ω load)
Lower Cut-Off Frequency (-3 dB)	DC/1 kHz switchable
Upper Cut-Off Frequency (-3 dB)	10 MHz
Rise/Fall Time (10% - 90%)	35 ns
Gain	40/60 dB switchable
Gain accuracy	± 0.2 dB

Tab. 5-2. Main feature of HVA-10M-60-B low noise amplifier

5.3. EXPERIMENTAL RESULTS

PLL response was tested by artificially creating a frequency response change in MEMS devices. The optical experimental setup is described in subparagraph 3.2.2.. Actuation signal was generated and controlled by National FlexRIO instrumentation, which was also in charge of collecting and converting data from the 3-quadrant photodiode. During the experiment, filter loop performed the mean of consecutive 16 data coming from optical detection setup.

5.3.1. Characterization

The most intuitive way to measure the step response is to introduce a known step change in the input signal and measure the phase response at the output. A second DDS (*DDS_DUT*) was introduced in LabVIEW program (figure 5-4) in order to simulate MEMS frequency behaviour and record PLL response to a shift on the resonance frequency. At every operative frequency, PC program defined MEMS behaviour and controlled *DDS_DUT* frequency, phase and amplitude. The operator could choose which ports to enable for the output and input signal through the variable *Select IN-OUT*. For example, when *Select IN-OUT* was 0, DUT simulated signal fed *AO1* and, through BNC cable, was connected back to AI0 and read by the system. Simultaneously, PC collected the elaboration of phase detector through LabVIEW local variables, displayed the results and saved the relative data. In this hybrid configuration PLL logic was performed on the PC, as much as frequency scans one, while data elaboration were still confined into the FPGA.

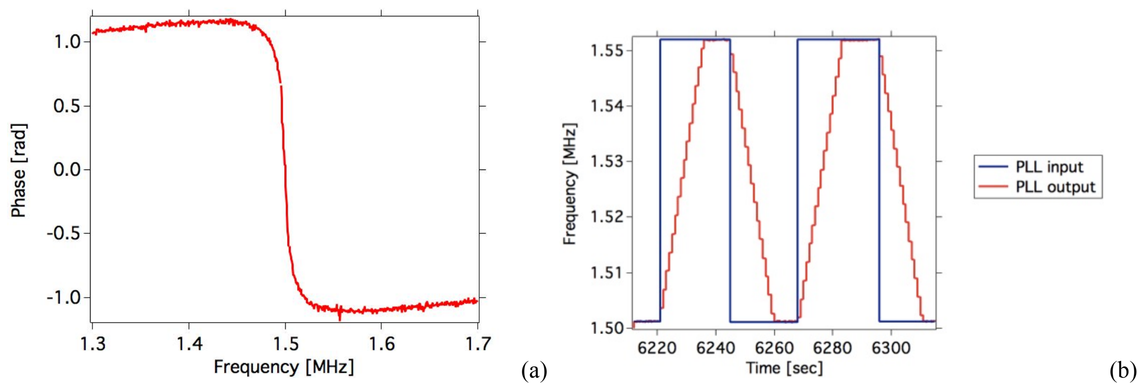

Fig 5-6. Test of the second-order DPLL performances. **(a)** Preliminary frequency scans performs on the simulated device. **(b)** Response of the DPLL to step change of the input resonance frequency.

We considered MEMS with 1.5 MHz resonance frequency, 100 as Q-factor and a peak amplitude of 0.0039 V_{PP}. An initial frequency scans, form 1.3 MHz to 1.7 MHz, was performed with a frequency step of 10 Hz, to define phase behaviour and identify the locked phase. DPLL was performed by locking the device at 0.03 rad and by defining a lock range of 0.01 rad with frequency step of 10 Hz. The results are shown in figure 5-6 (a). In particular, at 1.5 MHz, phase vs. frequency behaviour shows a sharp transition and in 8 kHz it goes from value 0 to 1.

Once locked to the resonance condition, we switched the resonance frequency of the simulated device from 1.5 MHz to 1.55 MHz, which correspond to a phase change of 10 %. The device was set to perform frequency

adjustment on actuation signal of 100 Hz per operative cycle. As shown in figure 5-6 (b), PLL was able to reach steady-state after 15 sec every step change in the input signal, with a sensitivity of 3.4 kHz/sec. Moreover, the experimental result shows that the detection error of resonance frequency accuracy in real-time is less than 200-350 Hz.

5.3.2. MEMS experiments

Our DPLL was tested on two different MEMS: AFM cantilever and pillar. PLL is commonly used in non-contact atomic force microscopy to measure the change in the resonance frequency of a silicon-cantilever caused by interactions force between resonator and sample surface. Pillar, unlike cantilever, requires more sensitivity. Where in array or in contact configuration, its excursion would not exceed 300 nm. It follows that DPLL must be able to detect smaller signals and discriminate them form environment noise.

To identify initial locked-phase, a preliminary frequency scans was performed over every samples with a step of 5 Hz. Once locked, we simulated the adsorption and evaporation of the analyte on resonator surface by turning off and on the vacuum system, respectively. Pump-off will lead a progressive increase of the pressure inside the chamber, mainly because of chamber wall degassing, which in turn increases hydrodynamic damping effects, with a consequent decrease of the resonance frequency and of the oscillation amplitude. On the contrary, pump-on will rapidly bring back the chamber pressure to its steady state value, with a rapid increase of the resonance frequency of the sensor.

AFM cantilever: Silicon nitride triangular cantilever was used to test DPLL. In particular a MLCT triangular cantilever (0.55 μm thick, 135 μm long and 13 μm width) was considered. This AFM tip presents a gold deposition on its backside, which increases device reflectivity, and its resonance frequency ranges over 26-50 kHz. Cantilever shown a sharp phase response during the frequency scans, with a π phase shift within 5 Hz. On the other hand, DPLL was able to follow resonance transition. In particular, during upper transitions caused by turning-on of the pump, rise time was 9 sec and sensitivity was 12 Hz/sec.

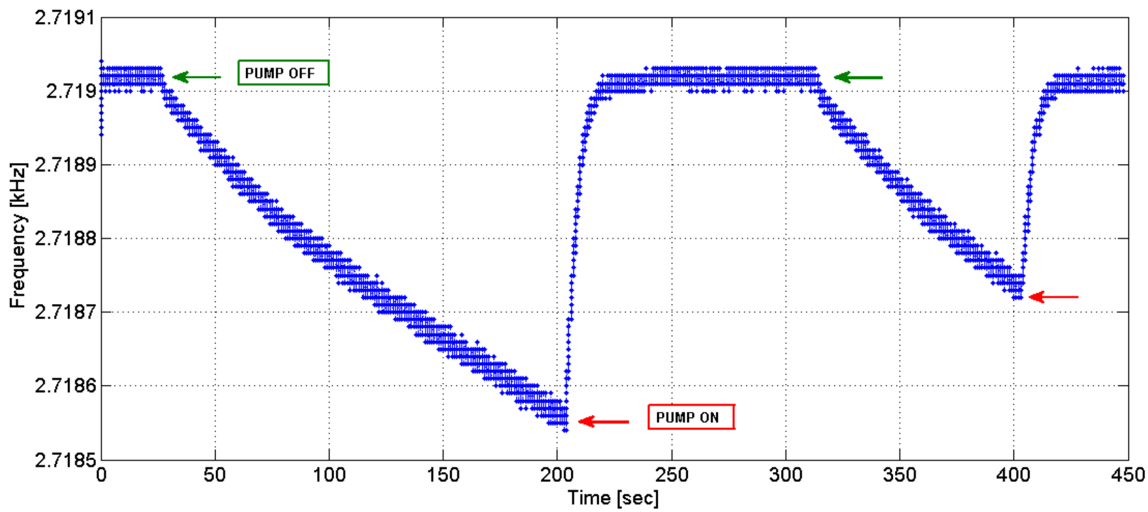

Fig 5-7. FlexRIO measurements on cantilever. DPLL results obtain by switching on and off the vacuum pump. Red arrows point at the moments pump was turned on while the green ones point at the moments pump was turn off.

Pillar: We tested both contact and no-contact (of "free") pillar. As already mention on chapter 5.2., contact pillar phase behaviour present a sharp transition at the resonance frequency, when mechanical contact takes place and negative frequency scan is performed. Contact pillar was actuated with $1V_{PP}$ sinusoidal signal and recorded with both network analyzed and FlexRIO. With NI5871 technology, detected amplitude signal was noisy and, on the plateau caused by contact, voltage standard deviation was 50 mV_{PP}.

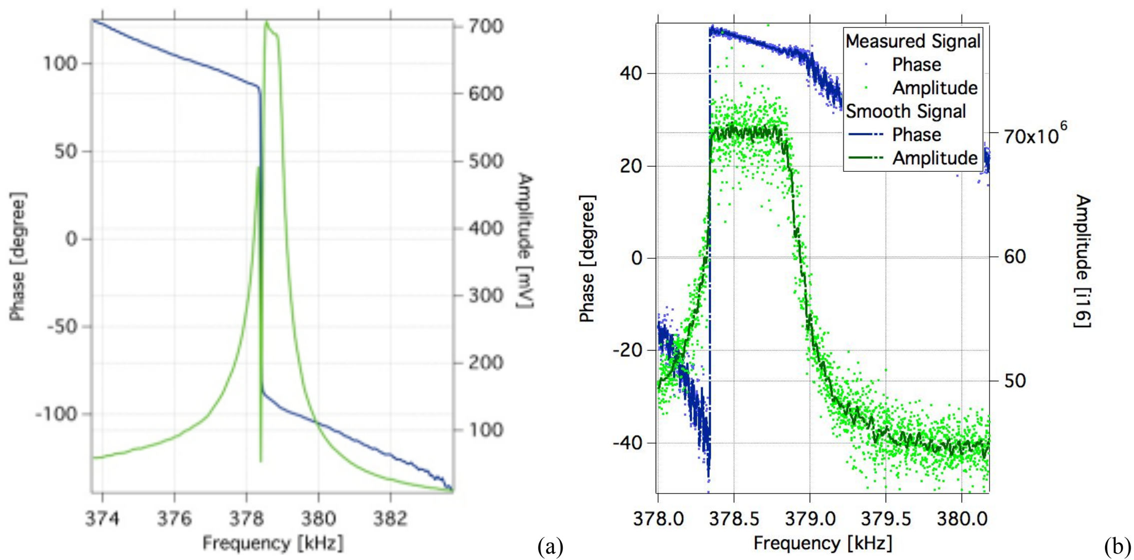

Fig 5-8. Frequency scans results on contact pillar obtained using **(a)** a network analyzer and **(b)** National NI5781R.

Moreover, detection required an accurate focalization of laser spot on pillar and high laser power (around 50 mV) in order to obtain input signal above few hundreds of mV_{PP}. The main reason behind these demanding operating conditions is the need to discriminate slightly pillar displacement but they increase thermal noise effects. Free silicon pillars (20x3.5x0.5 μm) were then tested for DPLL. On the positive front end, during pump switch on, DPLL measured 48 sample/sec and shown a sensitivity of 30 Hz/sec.

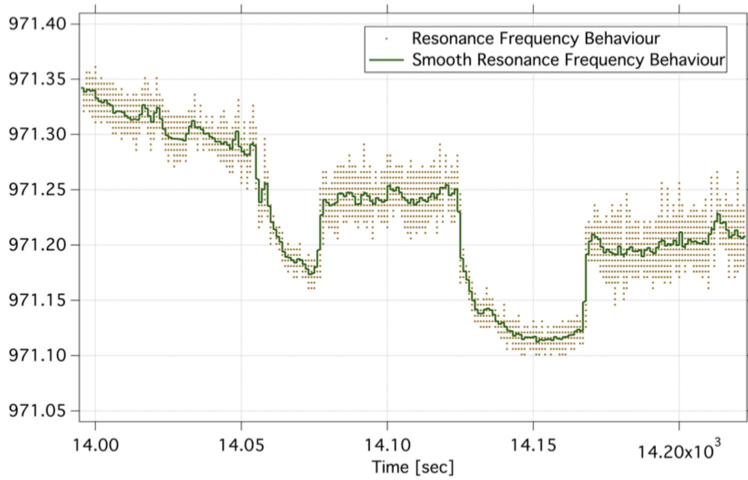

Fig 5-9. DPLL results obtain by switching on and off the vacuum pump.

When DPLL was locked, average standard deviation from mean resonance frequency was ± 25 Hz, which is equal to the frequency shift caused by adsorbed analyte mass of 0.5 10^{-21} g. In fact the mass sensitivity of the micropillar sensor can be expressed as [5-9]:

$$S = \frac{\Delta f}{\Delta m} = \frac{1}{2}\frac{f_0}{m_{eff}} \tag{5-10}$$

where f_0 is the resonance frequency, Δf the frequency shift, Δm the adsorbed mass and m_{eff} the effective mass of the sensor.

5.4. SUMMARY AND DISCUSSIONS

The work presents a study on digital PLL based on the NI 5781R and the program realized with LabVIEW FPGA module. Optical and electronic instrumentations were interfaced and optimized to enhance the readout

signal of the QPD. The setup was tested both with cantilever and pillars and was able to follow the resonance frequency shift caused by a change in the operating environment of MEMS resonator.

The results are helpful for future implementation on biomarker detection and there is room for several improvements concerning input filters and multiple pillars detection. In fact, when a piezo-crystal is actuated with a signal which is the sum of sinusoidal with different frequency, multiple pillars can be actuated simultaneously, as shown in figure 5-11. The evolution of the resonance frequency of multiple pillars can be recorded, giving the opportunities to studies how different analytes react when subjected at the same environment changes.

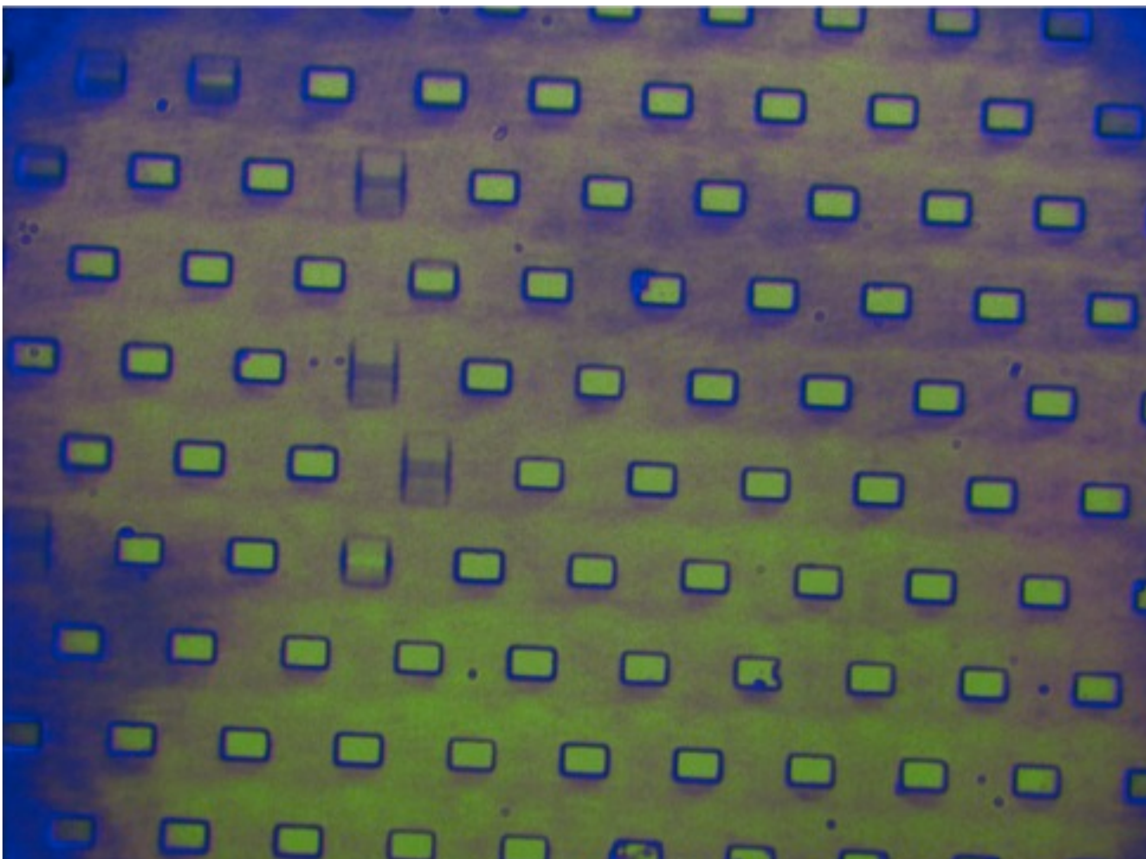

Fig 5-11. CCD image of an array of pillars actuated with a overlap of 4 sinusoidal signals.

However, in this scenario, an optical deflection mode cannot be applied for the detection of pillar movements, since the focalization of multiple lasers is a difficult and time-consuming operation.

REFERENCES

[5-1] B. Farhang-Boroujeny, "Signal processing techniques for software radios", Salt Lake City, UT, 2008.

[5-2] R. Andraka, "A survey of CORDIC algorithms for FPGA based computers".

[5-3] "A Technical Tutorial on Digital Signal Synthesis", Analog Device Inc., 1999.

[5-4] "NI 5781R User Guide and Specifications" National Instruments Corporation, Jan 2010.

[5-5] AD9777, Rev. C, Analog Device Inc., 2006.

[5-6] AD9640, Rev. B, Analog Device Inc., 2009.

[5-7] T. Schilcher, "RF applications in digital signal processing", Applications in digital signal processing, pp. 249-283, Aug. 2009.

[5-8] HVA-10M-60-B, Fempto.

[5-9] X. Li, H. Yu, X. Gan, X. Xia, P. Xu, J. Li, M. Liu, and Y. Li, "Integrated MEMS/NEMS Resonant Cantilevers for Ultrasensitive Biological Detection", Journal of Sensors, vol. 2009, issue 637874, Apr. 2009.

CONCLUSIONS

The aim of this Ph.D. project was to design and implement new actuation and read-out strategies for a fruitful application of MEMS resonator in medical and biological sensing field. To this purpose I combined together different approaches and competences, such as optics, image processing, microcircuit design and fabrication, digital data processing and FPGA programming. Different hardware prototypes were designed and realized in laboratory and preliminary test measurements were performed.

We considered two different MEMS resonator as sensors (cantilevers and pillars) and, for each one of them, a specific optical readout was implemented. Cantilevers are single end clamped beams fabricated in planar geometry, are commonly used in sensing applications, are easy to detect and to actuate using several alternative approaches, but suffer of liquid interactions damping and therefore did not find any concrete application as sensors in medicine and biology. Pillars are columnar resonators that, with a suitable chemical functionalization, can repel water and be operated easily in a biological environment; however, due to the peculiar fabrication process, available actuation and read out strategies are rather limited.

The first objective was the implementation of a readout system for the measurement in parallel of tens of MEMS sensors. Measurements were performed in vacuum, air and liquid. In vacuum frequency responses of 29 pillars were recorded in parallel in less than 5 minute, improving of near two orders of magnitude the measurement time required for obtaining the same information by serial readout [1]. Measurements in air and liquid were performed on cantilever. In particular, for liquid measurements, u-shape cantilevers were used and a microfluidic chamber was realized by PDMS, PMMA and micromachined aluminium.

The second objective was to integrate MEMS resonators, and in particular pillars, into a microelectronic chip, thus avoiding the use of external piezo-crystals for actuation and optical elements for detection. As already pointed out before, the integration of pillar with electric elements is not a trivial task, due to the vertical geometry and the in-plane oscillation, which makes the most common approaches, namely capacitive and piezoresistive, not straightforward. Therefore we implemented a Kelvin polarization force method for the actuation setup [2, 3], which has the advantage of not requiring any electrical contact on the resonator itself. Simulations were performed to optimize device performance and several electrical configurations were studied. The experimental results confirmed the possibility to modulate resonance amplitude peak by acting on the DC component of actuation voltage. Moreover, the resonator behaved as a micromechanical RF mixer. For detection

purpose a hard contact readout configuration was designed, which is compatible with Kelvin force actuation and do not require contacts on the resonator as well. In this system, under vibration, pillar behaved as an impact oscillator and its frequency response was studied. Different fabrication strategies were investigated, as well as measurement techniques.

The third objective was to develop an electronic control for acquiring frequency variation in real time. Relevant information can be derived by resonance frequency changes over time when MEMS interacts with analyte or is subjected with environment changes. This is usually obtained following resonator phase evolution in time with a phase lock loop (PLL) approach, however, no commercial instruments are able to operate both in the RF regime and following large frequency modulation (up to 10% of the central frequency). Under these considerations, a DPLL was realized using National Instrument NI5781R and LabVIEW FPGA module. In order to employ our system in the detection of low quantity of biomarker (fg), the software was designed to show a maximum frequency control on the function generator of 0.023 Hz. Measurements were performed by subjecting both cantilevers and pillars to environment changes and the results were promising.

A marginal activity, developed between Master and Ph.D. thesis, concerned the design and characteristics of a micro-system for thermogravimetric analysis (TGA) in which heater, temperature sensor and mass sensor are integrated into a single device are presented [4]. TGA sensors were tested using milli-Q water and polyurethane microcapsule and the results demonstrated that our approach provides a faster and more sensitive TGA with respect to commercial systems.

The development of all the projects connected with this study is still in progress to reach further improvements. Moreover, during Ph.D. period, 2 articles and 2 publications in proceeding of international conferences were published, all as a first author.

REFERENCES

[1] V. Toffoli, D. Borin, M. Tardivo, S. Dal Zilio, S. Carrato, G. Scoles, "Arrays of micromechanical pillars for biochemical detection", The 15th International Meeting on Chenical Sensors, March 2014, Buenos Aires (Argentina), Mar. 2014.

[2] V. Toffoli, F. Dandash, A. Pozzato, D. Borin, S. Carrato, and M. Lazzarino, "Actuation of silicon pillar micro-mechanical resonators by Kelvin polarization force", Microelectronic Engineering, vol. 111, pp. 1–6, November 2013.

[3] V. Toffoli, F. Dandash, A. Pozzato, D. Borin, S. Carrato, and M. Lazzarino. “Dielectric actuation of silicon pillar micro-mechanical resonators”, International Conference on Micro and Nano Engineering, Toulouse (France). Sept. 2012.

[4] V. Toffoli, S. Carrato, D. Lee, S. Jeon, and M. Lazzarino, “Heater-Integrated Cantilevers for Nano-Samples Thermogravimetric Analysis”, Sensors vol. 12, pp. 16657-16671, Dec. 2013.

ACKNOWLEDGEMENTS

First of all, I would like to sincerely thank my supervisors, Dr. Sergio Carrato and Dr. Marco Lazzarino, for their guidance, understanding, and, most importantly, patience during my Ph.D. graduate studies at the University of Trieste.

I would also like to thank my friends, colleagues and all of the members of the CNR-IOM research group. Their friendship and support lightened up my days and made my life more meaningful.

Finally, I would like to express my deepest gratitude to my family. Their endless support and encouragement made all of this possible.